Monthly Notices of the ROYAL ASTRONOMICAL SOCIETY

MNRAS **536,** 1268–1302 (2025) https://doi.org/10.1093/mnras/stae2620
Advance Access publication 2024 November 22

A splitting method for numerical relativistic magnetohydrodynamics

Serguei S. Komissarov ★ and David Phillips★
Department of Applied Mathematics, The University of Leeds, Leeds LS2 9JT, UK

Accepted 2024 November 15. Received 2024 November 15; in original form 2024 September 5

ABSTRACT

We describe a novel splitting approach to numerical relativistic magnetohydrodynamics (RMHD) designed to expand its applicability to the domain of ultrahigh magnetization (high-σ). In this approach, the electromagnetic field is split into the force-free component and its perturbation due to the plasma inertia. Accordingly, the system of RMHD equations is extended to include the subsystem of force-free degenerate electrodynamics and the subsystem governing the plasma dynamics and the perturbation of the force-free field. The combined system of conservation laws is integrated simultaneously, to which aim various numerical techniques can be used, and the force-free field is recombined with its perturbation at the end of every time-step. To explore the potential of this splitting approach, we combined it with a third-order weighted essentially non-oscillatory method, and carried out a variety of 1D and 2D test simulations. The simulations confirm the robustness of the splitting method in the high-σ regime, and also show that it remains accurate in the low-σ regime, all the way down to $\sigma = 0$. Thus, the method can be used for simulating complex astrophysical flows involving a wide range of physical parameters. The numerical resistivity of the code obeys a simple ansatz and allows fast magnetic reconnection in the plasmoid-dominated regime. The results of simulations involving thin and long current sheets agree very well with the theory of resistive magnetic reconnection.

Key words: magnetic reconnection – MHD – plasmas – shock – methods: numerical.

1 INTRODUCTION

The strong gravity of astrophysical black holes and neutron stars creates some of the most extreme physical conditions in the Universe which cannot be achieved in research laboratories. In particular, they naturally develop magnetospheres with extremely high plasma magnetization. Highly relativistic winds and jets emerging from these magnetospheres create spectacular structures on enormous scales, from parsecs (pulsar wind nebulae) to hundreds of kiloparsecs (jets of active galactic nuclei). These flows transport huge amounts of energy in the form of Poynting flux and the kinetic energy of the bulk motion, and drive the observed phenomena via magnetic reconnection and shock interaction with the external plasma. For plasma flows on such huge scales, relativistic magnetohydrodynamics (RMHD) is the most suitable framework.

The starting point of modern numerical schemes for compressible hydrodynamics (HD) and magnetohydrodynamics (MHD) is their differential equations written in the form of conservation laws, with the aim of developing a numerical analogue of these laws which provides conservation of the scheme-specific numerical approximation for the conserved quantities integrated over the volume of individual computational cells and the whole computational domain down to the processor rounding (machine) error. This is mainly because of the superior ability of such schemes to accurately capture shock waves. Both finite-volume and finite-difference schemes can be developed along these lines. The schemes may differ in many other aspects, like the type of Riemann solvers, the order of accuracy, etc. In terms of the integration of the Faraday equation, the modern numerical schemes for MHD and RMHD split into two major groups, those which use the generalized method of Lagrange multiplier (GLM, Munz et al. 2000; Dedner et al. 2002) and those that use the constrained transport method (CT, Evans & Hawley 1988).

In form, the Faraday equation of the MHD (and RMHD) system can be written as a law describing the conservation of the magnetic field integrated over the volume. This approach allows to integrate the Faraday equation in the same fashion as the other conservation laws, which is very convenient. However, it makes impossible to ensure that the magnetic field remains divergence-free, whatever numerical approximation of the divergence is chosen, because this condition involves not the volume integral of the magnetic field but its integral (magnetic flux) over a close surface. The uncontrolled deviation from the divergence-free state is not just an error for the magnetic field alone but may have severe implication for other flow parameters (Brackbill & Barnes 1980). For this reason, additional algorithms were developed to keep the magnetic field close to a divergence-free state.

In the CT method, the Faraday equation is treated as the law describing the conservation of magnetic flux over a surface. As the result, the normal components of the magnetic field have to be defined at the faces of computational cells and the electric field over their edges. This leads to the so-called staggered grid, where different physical parameters are defined at different points of the grid making this approach rather involved (for the recent analysis and comparison of various CT schemes, see Mignone & Del Zanna 2021). Moreover, since the energy (in Newtonian MHD) and the whole

★ E-mails: s.s.komissarov@leeds.ac.uk (SSK); david.phillips@fmi.fi (DP)

energy-momentum vector (in RMHD) include the electromagnetic contribution, integration of the corresponding conservation laws requires to define the magnetic field inside the computational cells as well. As a result, there are two numerical solutions for the magnetic fields, one defined at the cell faces and advanced using the surface form of the integral Faraday equation, and one defined inside the cells and advanced using the volume form of this equation. They may diverge over time, resulting in a rather uncomfortable state where the volume-based conserved variables like energy and momentum are inconsistent with the face-based magnetic field. In highly magnetized regions, this may even lead to an unphysical state with negative gas pressure. To prevent this, one may readjust the volume-based magnetic field and hence the conserved variables, thus making the numerical scheme not fully conservative. In Newtonian MHD, where out of all other conserved quantities the magnetic field is present only in the total energy, this can be done by simply removing the energy contribution due to the volume-based magnetic field and replacing it with the contribution due to the surface-base magnetic field (Balsara & Spicer 1999). This algorithm keeps the plasma contribution to the energy and hence the corresponding primitive variables (velocity, density, and thermal pressure of plasma) unchanged, thus making the deviation from the energy conservation superficial. In RMHD, both the magnetic and the electric field contribute to all the components of the total energy-momentum vector. Even if the volume-based magnetic field is a conserved variable, the volume-based electric field is not and can be found only via conversion of the conserved variables into the primitive ones (velocity, density, and thermal pressure of plasma) first, and then applying the perfect conductivity condition $\boldsymbol{E} = -\boldsymbol{v}\times\boldsymbol{B}$. As a result, the direct replacement of the electromagnetic contribution to the energy-momentum like in Balsara & Spicer (1999) is impossible. Instead, one is forced to carry out the 'harmonization' only after the variable conversion (Komissarov 1999). The same algorithm can be applied in Newtonian MHD, where it is equivalent to that of Balsara & Spicer (1999).

In the GLM method, the system of differential equations is extended by (1) introducing new scalar-dependent variable and hence one more evolution equation, and (2) modifying the Faraday equation to couple the new variable and the magnetic field. As a result, $\nabla\cdot B$ can be both transported away from the regions where it is generated, normally regions with large computational errors, and diffused over the computational domain effectively dumping its spacial oscillation. However, some residual divergence of the magnetic field remains. This method is very easy to implement, as it does not require any modification of the computational grid, and all the evolution equations are treated in the same way. At least in ideal Newtonian MHD, the GLM and CT methods provide similar accuracy (Mignone, Tzeferacos & Bodo 2010).

In contrast to Newtonian MHD, where it is sufficient to describe the plasma magnetization by the ratio of thermal and magnetic pressures ($\beta = p/p_{\rm m}$), relativistic plasma requires a different parameter $\sigma = b^2/4\pi w$, where $w = \epsilon + p$ is the relativistic enthalpy of plasma (where the internal energy density ϵ includes the contribution due to the rest mass energy of plasma particles), and $b^2 = B^2 - E^2$ is the Lorentz invariant equal to the squared strength of magnetic field as measured in the rest frame of plasma. Direct extension of the numerical methods developed for Newtonian MHD to RMHD has been quite successful in the low-σ regime. However, the high-σ regime has turned out to be very problematic, as these codes tend to crash, resulting in conserved variables which cannot be converted into physically meaningful set of primitive variables. In multidimensional simulations, these schemes begin to fail when $\sigma \sim 1$. On the one hand, this is a very high magnetization, never achieved in laboratory plasmas. On the other hand, it can be much higher in many problems of relativistic astrophysics. For example, in the pulsar magnetospheres, σ can be as high as $10^3 - 10^6$.

It has been suggested that the origin of this issue is the stiffness of the conservation laws of RMHD in the high-σ regime (Komissarov 2006a). Basically, when σ is high, the electromagnetic field dominates in the total energy and momentum. In this case, it is reasonable to expect that even small errors in the magnetic field, associated with the numerical integration of the Faraday equation, may lead to large errors in the plasma parameters, when they are computed from the conserved quantities. The quantitative analysis of the errors is rather complicated, however. To strengthen the argument, one may approach this problem from a different angle. The dynamics of electromagnetic field in highly rarefied plasma can be described using the approximation of the force-free degenerate electrodynamics (FFDE, e.g. MacDonald & Thorne 1982; Uchida 1997; Gruzinov 1999; Komissarov 2002). Normally, it is formulated as the Maxwell equations complimented with a constraint on the electric four-current, which ensures vanishing Lorentz force. The density of electric charges required to satisfy this constraint is quite small and the corresponding energy-momentum density of plasma can be negligibly small compared to that of the electromagnetic field. Alternatively, one may consider FFDE as RMHD in the limit $\sigma \to \infty$ (Komissarov 2002). In this limit, the set of the differential equations of RMHD reduces to the Faraday equation and the energy-momentum conservation laws for the electromagnetic field, complemented with the two perfect conductivity conditions. However, this system is overdetermined, with only two out of the four components of the energy-momentum equation being independent. For the numerical integration, this implies that any error in the computed magnetic field makes it inconsistent with the computed energy-momentum density.

For adiabatic flows, one can eliminate the energy equation from the set of numerically integrated equations of RMHD and this helps to extend the range of manageable magnetization up to $\sigma \approx 100$ (Komissarov et al. 2007b; Noble, Krolik & Hawley 2009). The conversion of remaining conserved variables to the primitive variables may still fail from time to time, becoming increasingly more severe for higher σ and requiring emergency fixes just to keep the simulations going. None the less, these results support the stiffness of RMHD equations as the reason for the high-σ failures, as the omission of the energy equation reduces this stiffness.

In their CT scheme for ideal RMHD, Mignone & Bodo (2006) applied exactly the same energy correction as Balsara & Spicer (1999), before converting the conserved variables into the primitive ones and replacing the cell-based magnetic field with the face-based one. This allowed them to succeed with the cylindrical explosion test for $B_0 = 1$ (see Section 5.3), which would failed otherwise. Martí (2015) went further and proposed an iterative algorithm for correcting the total energy-momentum vector, using the correction of Mignone & Bodo (2006) as a first step. This allowed them to avoid the conversion failure in the explosion test with $B_0 = 100$. The corresponding plasma magnetization in this problem is extremely high, with $\sigma > 2.5\times10^3$! This is a remarkable achievement, but some caution is in order. First, these corrections of conserved variables are different to that of Balsara & Spicer (1999) as they change not only the energy-momentum of the electromagnetic field but the energy-momentum of plasma as well. So, this is more than just resetting the cell-based magnetic field using the face-centred magnetic field. Second, there is no analysis to justify these corrections. The mathematical problem supposed to be solved by

the iterative algorithm of Martí (2015) is actually not posed. Even a qualitative understanding of why these corrections help to keep the conserved variables in the physical part of their domain is missing. As the result, it is not clear how robust these fixes are. A proper analytical and numerical investigation of this approach is required.

In addition to the conversion failures, RMHD simulations of highly magnetized flows suffer from excessive artificial plasma heating due to numerical resistivity. For this reason, the high-σ region is normally excluded when modelling black hole emission in simulations (e.g. Event Horizon Telescope Collaboration 2021).

In this paper, we propose an alternative to emergency fixes in the form of a radically new approach to computational RMHD which allows to mitigate the stiffness of its equations in the high-σ limit. In part, it was motivated by the method used by Tanaka (1994) for MHD simulations of the collision between the Earth's magnetosphere and the solar wind. In this problem, the Earth's magnetic field increases by many orders of magnitude from the collision site to the troposphere, where it is largely stationary and dipolar, whereas the perturbation of this field remains of about the same magnitude and hence increasingly small relative to the undisturbed Earth's field on approach to the troposphere. If the total magnetic field is evolved numerically, the truncation errors become large in comparison to the perturbation amplitude and hence the numerical solution for the perturbation becomes corrupted. To overcome this problem, Tanaka (1994) proposed to separate the strong stationary dipolar field from its perturbation and hence to integrate only the non-linear equations governing the perturbation. This approach has been proved to be very effective, and nowadays it is widely used in numerical modelling of planetary magnetospheres (e.g. Eggington et al. 2020).

Our problem is more complicated, however, as in the most interesting astrophysical applications, the strong background magnetic field is highly dynamic and cannot be considered as a known stationary component. At the first sight, this could be handled by allowing it to evolve according to the evolution equations of FFDE (Komissarov 2001, 2006b; McKinney 2006; Mahlmann et al. 2021). However, over time, the RMHD solution for the electromagnetic field could significantly deviate from the FFDE solution, with the force-free component and its perturbation having similar amplitudes. To keep the electromagnetic perturbation small, one could reset the division of the electromagnetic field into the strong force-free and perturbation components. The simplest way of doing this is to recombine the force-free field and its perturbation into the 'refreshed' force-free field, and to nullify the perturbation at the same time. In sufficiently simple problems, this could be done only so often. However, in some other problems, the perturbation may grow very rapidly. For example, consider a stationary fast magnetosonic shock. Since the fast modes of FFDE propagate with the speed of light, the FFDE solution will strongly deviate from the RMHD solution already after one time-step of numerical integration. This shows that to make the scheme robust, one has to invoke the resetting every time-step.

Numerical integration of FFDE equations, either in the form of the Maxwell equations with force-free current (Gruzinov 1999) or in the form of reduced RMHD equations (Komissarov 2002), does not conserve the electromagnetic energy-momentum and hence the splitting approach cannot ensure the conservation of the total energy-momentum down to the processor rounding error. However, a departure from this conservation seems inevitable for high-σ RMHD anyway, because it is the attempt to ensure the full conservation that leads to crashes.

In this paper, we describe a successful attempt to develop the splitting method based on these ideas. In Section 2, we detail the key principles of the splitting method. Section 3 describes the specifics of its numerical implementation. The 1D test simulations are presented in Section 4. In addition to the standard tests involving hyperbolic waves of RMHD, this section also describes the investigation of the scheme's numerical resistivity and the possibility to control the plasma heating via numerical magnetic dissipation. Section 5 describes the test simulations for inherently 2D problems. These include the investigation of the anisotropy of numerical resistivity, and a number of problems involving current sheets. The latter constitute a study focusing on the ability of ideal MHD codes to capture fast magnetic reconnection, apparently the first study of this kind. The whole study is summarized in Section 6 and the key conclusions are stated in Section 7. Appendix A describes the novel third-order weighted essentially non-oscillatory (WENO) interpolation employed by our code, and Appendix B gives the derivation of the key equations involved in the variable conversion algorithm.

2 THE KEY PRINCIPLES

2.1 Ideal relativistic magnetohydrodynamics

For an inertial frame of Minkowski space–time, the system of ideal RMHD in consists of the Faraday equation

$$\partial_t \boldsymbol{B} + \nabla \times \boldsymbol{E} = 0\,, \tag{1}$$

the energy equation

$$\partial_t \left(\frac{E^2 + B^2}{2} + w\gamma^2 - p \right) + \nabla \cdot (\boldsymbol{E} \times \boldsymbol{B} + w\gamma^2 \boldsymbol{v}) = 0\,, \tag{2}$$

the momentum equation

$$\partial_t \left(\boldsymbol{E} \times \boldsymbol{B} + w\gamma^2 \boldsymbol{v} \right) + \nabla \cdot \left[-\boldsymbol{E} \otimes \boldsymbol{E} - \boldsymbol{B} \otimes \boldsymbol{B} + w\gamma^2 \boldsymbol{v} \otimes \boldsymbol{v} + \mathbf{g} \left(\frac{E^2 + B^2}{2} + p \right) \right] = 0\,, \tag{3}$$

the continuity equation

$$\partial_t (\rho\gamma) + \nabla \cdot (\rho\gamma \boldsymbol{v}) = 0\,, \tag{4}$$

the divergence-free condition for the magnetic field

$$\nabla \cdot \boldsymbol{B} = 0\,, \tag{5}$$

and the perfect conductivity condition

$$\boldsymbol{E} = -\boldsymbol{v} \times \boldsymbol{B}\,. \tag{6}$$

Here, p is the thermodynamic pressure, ρ is the density of plasma particles rest mass, $\boldsymbol{g}$ is the metric tensor of space, $\boldsymbol{v}$ is the fluid velocity, γ is the corresponding Lorentz factor, $\boldsymbol{B}$ and $\boldsymbol{E}$ are the vectors of electric and magnetic field, respectively, as measured in the aforementioned inertial frame. $w(p, \rho)$ is the relativistic enthalpy per unit volume. In what follows, we use the equation of state

$$w = \rho + \kappa p \quad \text{with} \quad \kappa = \frac{\Gamma}{\Gamma - 1}\,, \tag{7}$$

where Γ is the ratio of specific heats. Here, we utilize the relativistic units where neither the speed of light no the geometric factor $1/4\pi$ appear in the equations (for example $\sigma = b^2/w$). We also agree that for any three-vector of the space $\boldsymbol{a}$, $a^2 = a_i a^i$, and $a = \sqrt{a^2}$, and for any four-vector a^ν of the space–time, $a^2 = a_\nu a^\nu$, and use $-+++$ signature for the space–time.

Let us now discuss how the errors in numerical integration of the energy-momentum equations can result in an unphysical state. Consider the four-vector of energy-momentum density, $\Pi^\mu = -T^{\mu\nu} n_\nu$,

where $T^{\mu\nu}$ is stress-energy-momentum tensor, and n_ν is the four-velocity of the fiducial observer who measures the energy and momentum. When the observer is at rest in the space, $n_\nu = -\delta^t_\nu$ and $\Pi^\nu = (\mathcal{E}, \boldsymbol{S})$, where $\mathcal{E}$ and $\boldsymbol{S}$ are the energy and momentum densities, respectively. For the electromagnetic field, this is

$$\Pi^\nu_{\rm em} = \left(\frac{E^2+B^2}{2}, \boldsymbol{E}\times\boldsymbol{B}\right), \quad \text{where} \quad \boldsymbol{E} = -\boldsymbol{v}\times\boldsymbol{B}, \tag{8}$$

and

$$\Pi^2_{\rm em} = -\frac{1}{4}\left(B^2_\parallel + \frac{B^2_\perp}{\gamma^2}\right)^2 < 0, \tag{9}$$

where $\boldsymbol{B}_\parallel$ and $\boldsymbol{B}_\perp$ are the components of the magnetic field parallel and orthogonal to the velocity, respectively. Hence, $\Pi^\nu_{\rm em}$ is a time-like four-vector. For the plasma (fluid),

$$\Pi^\nu_{\rm pl} = (w\gamma^2 - p, w\gamma^2\boldsymbol{v}), \tag{10}$$

and

$$\Pi^2_{\rm pl} = \gamma^2 w(2p-w) - p^2. \tag{11}$$

For the physical range of specific heats, $1<\Gamma<2$, and the combination $2p - w = p\dfrac{\Gamma-2}{\Gamma-1} - \rho$ is strictly negative. Hence , $\Pi^\nu_{\rm pl}$ is also a time-like four-vector. For the total energy-momentum vector $\Pi_{\rm t} = \Pi_{\rm em} + \Pi_{\rm pl}$,

$$\Pi^2_{\rm t} = \Pi^2_{\rm em} + \Pi^2_{\rm pl} + 2(-\mathcal{E}_{\rm em}\mathcal{E}_{\rm pl} + (\boldsymbol{S}_{\rm em}\cdot\boldsymbol{S}_{\rm pl})) < 0 \tag{12}$$

and hence $\Pi^\nu_{\rm t}$ is also time-like (This is a particular case of the general result on the sum of future-directed time-like vectors of space–time.).

Obviously, if the numerical integration results in a space-like $\Pi^\nu_{\rm t}$, the conversion of conserved quantities into primitive ones will fail. However, this is the same as in the numerical relativistic HD, and hence the truncation errors arising in the numerical integration of the energy-momentum equations are unlikely to be the cause of the problems specific to the high-σ regime of RMHD. The source of errors specific only to RMHD is the Faraday equation. In the rest of this section, we demonstrate that sufficiently large errors in magnetic field can render the set of conserved variables unphysical by pushing the energy-momentum vector of plasma $\Pi^\nu_{\rm pl}$ into the space-like domain.

We start with a physical state with the magnetic field $\boldsymbol{B}_0$ and the total energy-momentum $\Pi^\nu_{\rm t,0}$. Then, we analyse other states with $\Pi^\nu_{\rm t} = \Pi^\nu_{\rm t,0}$ but $\boldsymbol{B} = \boldsymbol{B}_0 + \delta\boldsymbol{B}$, where the small perturbation $\delta\boldsymbol{B}$ plays the role of the computational error. The aim is to determine how large this error can be before the energy-momentum vector of plasma $\Pi^\nu_{\rm pl}$ turns space-like. In general, the impact of this error is hard to analyse. To simplify the analysis, we assume that $\delta\boldsymbol{B} \parallel \boldsymbol{B}_0$ and consider only the cases where $\boldsymbol{v}_0$ is either parallel or perpendicular to $\boldsymbol{B}_0$. Since the total momentum vector

$$\boldsymbol{S}_{\rm t} = (B^2 + w\gamma^2)\boldsymbol{v} - (\boldsymbol{v}\cdot\boldsymbol{B})\boldsymbol{B},$$

$\boldsymbol{v}$ will remain either parallel or perpendicular to $\boldsymbol{B}$ in the perturbed state as well. We will also assume that the magnetic field strength increases, $B = B_0 + \delta B$ where $\delta B > 0$, as only this case is constraining.

When $\boldsymbol{v}_0 \parallel \boldsymbol{B}_0$, the electromagnetic momentum $\boldsymbol{S}_{\rm em,0} = \boldsymbol{0}$, and hence

$$\Pi^2_{\rm t,0} = \Pi^2_{\rm em,0} + \Pi^2_{\rm pl,0} - 2\mathcal{E}_{\rm em,0}\mathcal{E}_{\rm pl,0}, \tag{13}$$

and

$$\Pi^2_{\rm t} = \Pi^2_{\rm em} + \Pi^2_{\rm pl} - 2\mathcal{E}_{\rm em}\mathcal{E}_{\rm pl}. \tag{14}$$

Since $\Pi^2_{\rm t} = \Pi^2_{\rm t,0}$, this implies that

$$\Pi^2_{\rm pl} = \Pi^2_{\rm pl,0} - \delta\Pi^2_{\rm em} + 2(\mathcal{E}_{\rm em}\mathcal{E}_{\rm pl} - \mathcal{E}_{\rm em,0}\mathcal{E}_{\rm pl,0}), \tag{15}$$

where $-\delta\Pi^2_{\rm em} = -(\Pi^2_{\rm em} - \Pi^2_{\rm em,0}) = B_0^3\delta B > 0$. For $\Pi^\nu_{\rm pl}$ to be time-like, the whole expression on the right-hand side of this equation must be negative, which is the condition for the perturbed state to be physical. When $\mathcal{E}_{\rm pl} \ll \mathcal{E}_{\rm em}$, the term $\Pi^2_{\rm pl,0} \ll \mathcal{E}_{\rm em,0}\mathcal{E}_{\rm pl}$ can be ignored. One may also ignore the small difference $\delta\mathcal{E}_{\rm em}$ between $\mathcal{E}_{\rm em}$ and $\mathcal{E}_{\rm em,0}$. With these simplifications, the physicality condition reads

$$2\mathcal{E}_{\rm em,0}(\mathcal{E}_{\rm pl} - \mathcal{E}_{\rm pl,0}) - \delta\Pi^2_{\rm em} < 0. \tag{16}$$

Since the last term in this expression is positive, this implies that the plasma energy in the perturbed state must be lower than the one in the original state. Moreover, this condition will not be satisfied by any $\mathcal{E}_{\rm pl} > 0$ unless

$$-\delta\Pi^2_{\rm em} < 2\mathcal{E}_{\rm em,0}\mathcal{E}_{\rm pl,0}.$$

Using $\mathcal{E}_{\rm em,0} = B_0^2/2$, $\mathcal{E}_{\rm pl,0} = w_0\gamma_0^2 - p_0 \simeq w_0\gamma_0^2$, and utilizing the fact that in this case $b^2 = B^2$, we finally arrive to the upper limit on the maximum error in magnetic field

$$\frac{\delta B}{B_0} \lesssim 2\frac{\gamma_0^2}{\sigma_0}. \tag{17}$$

When $\boldsymbol{v}_0 \perp \boldsymbol{B}_0$, the electromagnetic momentum does not vanish. Hence, equation (15) is replaced with

$$\Pi^2_{\rm pl} = \Pi^2_{\rm pl,0} - \delta\Pi^2_{\rm em} + 2(\mathcal{E}_{\rm em}\mathcal{E}_{\rm pl} - \mathcal{E}_{\rm em,0}\mathcal{E}_{\rm pl,0}) + 2((\boldsymbol{S}_{\rm em,0}\cdot\boldsymbol{S}_{\rm pl,0}) - (\boldsymbol{S}_{\rm em}\cdot\boldsymbol{S}_{\rm pl})), \tag{18}$$

where $-\delta\Pi^2_{\rm em} = B_0^3\delta B/\gamma_0^4 > 0$, and equation (16) with

$$2\mathcal{E}_{\rm em,0}\delta\mathcal{E}_{\rm pl} - 2(\boldsymbol{S}_{\rm em,0}\cdot\delta\boldsymbol{S}_{\rm pl}) - \delta\Pi^2_{\rm em} < 0, \tag{19}$$

where $\mathcal{E}_{\rm em,0} = B_0^2(1+v_0^2)/2$, $\boldsymbol{S}_{\rm em,0} = B_0^2\boldsymbol{v}_0$, $\delta\mathcal{E}_{\rm pl} = \mathcal{E}_{\rm pl} - \mathcal{E}_{\rm pl,0}$, and $\delta\boldsymbol{S}_{\rm pl} = \boldsymbol{S}_{\rm pl} - \boldsymbol{S}_{\rm pl,0}$. When $v_0, v \ll 1$, the second term in equation (19) can be ignored, leading to the condition (17) with $\gamma_0 = 1$. When $v_0, v \simeq 1$, one may use the approximation $\delta\boldsymbol{S}_{\rm pl} \simeq \delta\mathcal{E}_{\rm pl}\boldsymbol{v}_0$, which yields $2(\boldsymbol{S}_{\rm em,0}\cdot\delta\boldsymbol{S}_{\rm pl}) \simeq 2B_0^2v_0^2\delta\mathcal{E}_{\rm pl}$. Substituting these into equation (19), one obtains the simplified physicality condition

$$\frac{B_0^2\delta\mathcal{E}_{\rm pl}}{\gamma_0^2} - \delta\Pi^2_{\rm em} < 0.$$

Thus, like in the parallel case, $\delta\mathcal{E}_{\rm pl}$ must be negative. Moreover, this condition will not be satisfied by any $\mathcal{E}_{\rm pl} > 0$ unless

$$-\delta\Pi^2_{\rm em} < \frac{B_0^2\mathcal{E}_{\rm pl,0}}{\gamma_0^2},$$

which leads to the upper limit on the error in magnetic field

$$\frac{\delta B}{B_0} \lesssim \frac{\gamma_0^2}{\sigma_0}, \tag{20}$$

where we applied $B^2 = \gamma^2 b^2$. Interestingly, this limit differs from the one obtained for the parallel case only by the factor of two, suggesting that there is no strong dependence on the angle between

the velocity and magnetic field. The accuracy constraints may be even more restrictive than those we have derived. For example, we did not take into account that the plasma energy of the perturbed state cannot fall below $D = \rho_0\gamma_0$, the conserved variable that has to be preserved in the perturbed state as well.

In the standard approach, one may try to tackle the issue of conversion failures via increasing the accuracy of the magnetic field integration. In the splitting approach, we seek to reduce the impact of the errors in the magnetic field on the energy-momentum of plasma.

2.2 Splitting equations of ideal RMHD into the electromagnetic field and plasma components

Let us split the electromagnetic field into two components

$$\boldsymbol{B} = \boldsymbol{B}_{(0)} + \boldsymbol{B}_{(1)}\,, \quad \boldsymbol{E} = \boldsymbol{E}_{(0)} + \boldsymbol{E}_{(1)}\,,$$

where the component with the suffix 0 satisfies the equations of FFDE. Here, we use the formulation of FFDE due to Komissarov (2002)

$$\partial_t \boldsymbol{B}_{(0)} + \nabla\times\boldsymbol{E}_{(0)} = 0\,, \tag{21}$$

$$\partial_t\left(\frac{E_{(0)}^2 + B_{(0)}^2}{2}\right) + \nabla\cdot(\boldsymbol{E}_{(0)}\times\boldsymbol{B}_{(0)}) = 0\,, \tag{22}$$

$$\partial_t\left(\boldsymbol{E}_{(0)}\times\boldsymbol{B}_{(0)}\right) + \nabla\cdot\left(-\boldsymbol{E}_{(0)}\otimes\boldsymbol{E}_{(0)} - \boldsymbol{B}_{(0)}\otimes\boldsymbol{B}_{(0)} + \boldsymbol{g}\left(\frac{E_{(0)}^2 + B_{(0)}^2}{2}\right)\right) = 0\,, \tag{23}$$

$$\nabla\cdot\boldsymbol{B}_{(0)} = 0\,, \tag{24}$$

and

$$(\boldsymbol{E}_{(0)}\cdot\boldsymbol{B}_{(0)}) = 0\,. \tag{25}$$

The last equation is one of the constraints imposed by the perfect conductivity. The second one is

$$B_{(0)} > E_{(0)}\,. \tag{26}$$

The energy-momentum equations can be considered as the corresponding equations of RMHD in the limit of vanishing plasma inertia. Equations (25) and (26) follow from the perfect conductivity condition $\boldsymbol{E} = -\boldsymbol{v}\times\boldsymbol{B}$. Conversely, equations (25) and (26) ensure the existence of inertial frames where the electric field vanishes. One of these frames is the rest frame of plasma, the others move relative to it along the magnetic field. When conditions (25) and (26) are satisfied, the FFDE system is hyperbolic, with a pair of fast magnetosonic modes and a pair of Alfvén modes. There are seven evolution equations in the FFDE system, (21)–(23). Together with the algebraic constraint (25) imposed by the prefect conductivity condition, this gives eight equations in total.[1] This exceeds by two the number of dependent variables (components of $\boldsymbol{B}_{(0)}$ and $\boldsymbol{E}_{(0)}$). This is because only two components of the energy-momentum equations are independent (Komissarov 2002). For numerical integration, however, this means that the system of equations is overdetermined, and in order to convert the energy-momentum density into the electric field, some of the components of the energy-momentum have to be ignored, which can be done in many different ways. Our algorithm will be described later in Section 3.6.

[1]The divergence-free state of the magnetic field is preserved by the Faraday condition and hence does not need to be counted. The condition $E > B$ does not affect the evolution, until it gets broken, and for this reason it is not counted too.

The component with suffix 1 describes the correction (perturbation) of the force-free field due to the plasma inertia. The equations governing this component of the electromagnetic field, and at the same time the motion of plasma, are obtained from the full system of RMHD by removing the terms cancelling each other via equations (21)–(24). This yields

$$\partial_t \boldsymbol{B}_{(1)} + \nabla\times\boldsymbol{E}_{(1)} = 0\,, \tag{27}$$

$$\partial_t\left(\boldsymbol{E}_{(0)}\cdot\boldsymbol{E}_{(1)} + \boldsymbol{B}_{(0)}\cdot\boldsymbol{B}_{(1)} + \frac{(E_{(1)}^2 + B_{(1)}^2)}{2} + w\gamma^2 - p\right)$$
$$+\nabla\cdot\left(\boldsymbol{E}_{(0)}\times\boldsymbol{B}_{(1)} + \boldsymbol{E}_{(1)}\times\boldsymbol{B}_{(0)} + \boldsymbol{E}_{(1)}\times\boldsymbol{B}_{(1)} + w\gamma^2\boldsymbol{v}\right) = 0\,, \tag{28}$$

$$\partial_t\left(\boldsymbol{E}_{(0)}\times\boldsymbol{B}_{(1)} + \boldsymbol{E}_{(1)}\times\boldsymbol{B}_{(0)} + \boldsymbol{E}_{(1)}\times\boldsymbol{B}_{(1)} + w\gamma^2\boldsymbol{v}\right)$$
$$+\nabla\cdot\Big(-\boldsymbol{E}_{(1)}\otimes\boldsymbol{E}_{(0)} - \boldsymbol{E}_{(0)}\otimes\boldsymbol{E}_{(1)} - \boldsymbol{E}_{(1)}\otimes\boldsymbol{E}_{(1)}$$
$$-\boldsymbol{B}_{(1)}\otimes\boldsymbol{B}_{(0)} - \boldsymbol{B}_{(0)}\otimes\boldsymbol{B}_{(1)} - \boldsymbol{B}_{(1)}\otimes\boldsymbol{B}_{(1)}$$
$$+\boldsymbol{g}\left[\boldsymbol{E}_{(0)}\cdot\boldsymbol{E}_{(1)} + \boldsymbol{B}_{(0)}\cdot\boldsymbol{B}_{(1)} + \frac{E_{(1)}^2 + B_{(1)}^2}{2}\right]$$
$$+w\gamma^2\boldsymbol{v}\otimes\boldsymbol{v} + \boldsymbol{g}\,p\Big) = 0\,, \tag{29}$$

$$\partial_t\rho\gamma + \nabla\cdot\rho\gamma\boldsymbol{v} = 0\,, \tag{30}$$

$$\nabla\cdot\boldsymbol{B}_{(1)} = 0\,, \tag{31}$$

$$\boldsymbol{E}_{(1)} = -\boldsymbol{v}\times\boldsymbol{B}_{(1)} - (\boldsymbol{E}_{(0)} + \boldsymbol{v}\times\boldsymbol{B}_{(0)})\,. \tag{32}$$

The energy-momentum equations (28)–() do not involve the terms quadratic in $\boldsymbol{B}_{(0)}$ and $\boldsymbol{E}_{(0)}$, which are dominant in problems with high σ. As a result, the effect of the truncation error in calculations of $\boldsymbol{B}_{(0)}$ on plasma parameters is reduced. The FFDE field still enters the plasma equations via linear terms. These interaction terms describe both the effect of the electromagnetic field on the plasma motion, and the effect plasma inertia on the evolution of the electromagnetic field. The two components of the electromagnetic field are also coupled via the perfect conductivity equation (32).

2.3 Numerical splitting

Each time-step of numerical integration consists of following three substeps:

(i) Given the solution at the time t^n, including $\boldsymbol{B}^n$ and $\boldsymbol{E}^n$, one introduces

$$\boldsymbol{B}^n_{(0)} = \boldsymbol{B}^n, \tag{33}$$

$$\boldsymbol{E}^n_{(0)} = \boldsymbol{E}^n, \tag{34}$$

$$\boldsymbol{B}^n_{(1)} = 0, \tag{35}$$

$$\boldsymbol{E}^n_{(1)} = 0. \tag{36}$$

(ii) The combined equations of the FFDE and perturbation subsystems are integrated simultaneously to obtain the solution at the time $t^{n+1} = t^n + \Delta t$. The evolution equations of the combined system are conservation laws and can be written as a single vector equation

$$\partial_t\boldsymbol{q} + \nabla\cdot\boldsymbol{f} = 0, \tag{37}$$

where

$$\boldsymbol{q} = \begin{pmatrix}\boldsymbol{q}_{(0)}\\ \boldsymbol{q}_{(1)}\end{pmatrix} \quad \text{and} \quad \boldsymbol{f} = \begin{pmatrix}\boldsymbol{f}_{(0)}\\ \boldsymbol{f}_{(1)}\end{pmatrix},$$

are the vectors of conserved variables and their fluxes, respectively. The subvector of conserved FFDE variables is

$$\boldsymbol{q}_{(0)} = \begin{pmatrix} \boldsymbol{B}_{(0)} \\ \mathcal{E}_{(0)} \\ \boldsymbol{S}_{(0)} \end{pmatrix}, \tag{38}$$

where

$$\mathcal{E}_{(0)} = \frac{E_{(0)}^2 + B_{(0)}^2}{2}, \quad \boldsymbol{S}_{(0)} = \boldsymbol{E}_{(0)} \times \boldsymbol{B}_{(0)}, \tag{39}$$

and the subvector of conserved perturbation variables is

$$\boldsymbol{q}_{(1)} = \begin{pmatrix} \boldsymbol{B}_{(1)} \\ \mathcal{E}_{(1)} \\ \boldsymbol{S}_{(1)} \\ D \end{pmatrix}, \tag{40}$$

where

$$\mathcal{E}_{(1)} = (\boldsymbol{E}_{(0)} \cdot \boldsymbol{E}_{(1)}) + (\boldsymbol{B}_{(0)} \cdot \boldsymbol{B}_{(1)}) + \frac{(E_{(1)}^2 + B_{(1)}^2)}{2} + w\gamma^2 - p \tag{41}$$

$$\boldsymbol{S}_{(1)} = \boldsymbol{E}_{(0)} \times \boldsymbol{B}_{(1)} + \boldsymbol{E}_{(1)} \times \boldsymbol{B}_{(0)} + \boldsymbol{E}_{(1)} \times \boldsymbol{B}_{(1)} + w\gamma^2 \boldsymbol{v} \tag{42}$$

$$D = \rho\gamma\,. \tag{43}$$

(iii) The total electromagnetic field vectors at the time t^{n+1} are computed via

$$\boldsymbol{B}^{n+1} = \boldsymbol{B}_{(0)}^{n+1} + \boldsymbol{B}_{(1)}^{n+1}, \tag{44}$$

$$\boldsymbol{E}^{n+1} = \boldsymbol{E}_{(0)}^{n+1} + \boldsymbol{E}_{(1)}^{n+1}. \tag{45}$$

Using simple conditional switches, the computer code based on this splitting scheme can be turned into a FFDE code and a standard (unsplit) RMHD code. To run it in the FFDE mode, one simply has to integrate only the FFDE equations and keep $\boldsymbol{B}_{(1)} = \boldsymbol{E}_{(1)} = 0$. To run it in the standard RMHD mode, one has bypass the splitting step (i), integrate only the perturbation equations, and keep $\boldsymbol{B}_{(0)} = \boldsymbol{E}_{(0)} = 0$. This will be used later for testing the splitting approach against the standard one in the low-σ regime.

2.4 Controlled energy transfer

In the splitting method, the energy-momentum of the force-free component of the electromagnetic field is separated from the energy-momentum of plasma. Thanks to this separation, the errors arising in the numerical integration of the Faraday equation for the this field can no longer directly impact the state of plasma and result in a conversion failure. This is the main advantage of the separation approach. On the other hand, this separation also prohibits the plasma heating via numerical resistivity. In some cases, this can be considered as beneficial. However, this may be detrimental in problems involving current sheets, where the magnetic dissipation and plasma heating are paramount.

In ideal MHD simulations, the numerical resistivity arises via the rounding errors emerging in numerical integration of the Faraday equation. In 'good' schemes, it leads mostly to diffusion of the magnetic field through plasma and reduction of its spatial gradients. This smoothing out of the magnetic field is accompanied by reduction (dissipation) of the magnetic energy. In standard conservative schemes for MHD, the total energy is conserved, which implies that this reduction of magnetic energy is fully compensated by the increase of plasma energy. The rate of this numerical plasma heating is fixed implicitly by the algorithm for integration of the Faraday equation. This lack of control may lead to undesirable numerical heating of plasma. For example, the highly magnetized plasma in the accretion disc funnel emerging in numerical simulations of the black hole accretion gets heated to extremely high temperature for this very reason (e.g. Event Horizon Telescope Collaboration 2021). The splitting approach, allows us to introduce control over the energy transfer between the electromagnetic field and plasma associated with the rounding errors.

At some point during the integration step (ii), the conserved quantities are converted into the primitive ones. In particular, $\mathcal{E}_{(0)}^{n+1}$ and $\boldsymbol{S}_{(0)}^{n+1}$ are converted into $\boldsymbol{E}_{(0)}^{n+1}$. Given the nominal overdeterminacy of the FFDE subsystem, this can be done only if we reduce the number of equations used for the conversion. There are many ways of doing this, each time departing from the computed conserved variables in one way or another. Here, we follow Komissarov (2002) and compute the electric field via

$$\boldsymbol{E}_{(0)}^{n+1} = \frac{1}{B_{(0)}^{n+1\,2}} \boldsymbol{S}_{(0)}^{n+1} \times \boldsymbol{B}_{(0)}^{n+1} \tag{46}$$

if $\boldsymbol{B}_{(0)}^{n+1} \neq \boldsymbol{0}$, otherwise $\boldsymbol{E}_{(0)}^{n+1} = \boldsymbol{0}$. Computing the electric field this way ensures the perfect conductivity condition $\boldsymbol{E}_{(0)}^{n+1} \cdot \boldsymbol{B}_{(0)}^{n+1} = 0$. However, the obtained electric field may exceed, especially at current sheets, the magnetic one, breaking the second perfect conductivity condition (26). Whenever this takes place, the electric field $E_{(0)}$ is reduced somewhat below $B_{(0)}$ (in the test simulations to the level $0.9999 B_{(0)}$), or to zero if $B_{(0)} = 0$. This amounts to dissipation of the FFDE electromagnetic energy (e.g. Komissarov 2004, 2006b). Even without this rescaling of the electric field, the electromagnetic energy density based on the obtained $E_{(0)}^{n+1}$ and $B_{(0)}^{n+1}$,

$$\tilde{\mathcal{E}}_{(0)}^{n+1} = (E_{(0)}^{n+1\,2} + B_{(0)}^{n+1\,2})/2\,, \tag{47}$$

will be different from $\mathcal{E}_{(0)}^{n+1}$ obtained via integration of the energy equation (22), giving rise to the energy difference

$$\delta\mathcal{E}_{(0)}^{n+1} = \mathcal{E}_{(0)}^{n+1} - \tilde{\mathcal{E}}_{(0)}^{n+1}\,. \tag{48}$$

When $\delta\mathcal{E}_{(0)}^{n+1} > 0$, the electromagnetic energy dissipates. Transferring the dissipated energy to the perturbation subsystem can only decrease $\Pi_{\rm pl}^2$ and should not result in conversion failure.

To further support this conclusion, consider unmagnetized fluid with conserved variables $D = \rho\gamma$, $S_{\rm pl} = w\gamma^2 v$, $\mathcal{E}_{\rm pl} = w\gamma^2 - p$, and determine the response of the gas pressure δp to the energy variation $\delta\mathcal{E}_{\rm pl}$ under constant D and S. Straightforward calculations show that

$$\delta p = \mathcal{A}\,\delta\mathcal{E}_{\rm pl}\,,$$

where

$$\mathcal{A} = \frac{w\gamma^2 + \kappa p(\gamma^2 - 1)}{\rho\gamma^2(\kappa - 1) + \kappa p(\gamma^2(\kappa - 2) + 1)}\,,$$

$\kappa = \Gamma/(\Gamma - 1)$, and Γ is the ratio of specific heats. For $1 < \Gamma < 2$, the proportionality coefficient $\mathcal{A}$ is positive, and hence $\delta\mathcal{E}$ and δp have the same sign. This suggests that the transfer of $\delta\mathcal{E}_{(0)}^{n+1} > 0$ to the perturbation system

$$\mathcal{E}_{(1)}^{n+1} \to \mathcal{E}_{(1)}^{n+1} + \delta\mathcal{E}_{(0)}^{n+1}\,. \tag{49}$$

will result in plasma heating.

When $\delta\mathcal{E}_{(0)}^{n+1} < 0$, its transfer to the perturbation subsystem may increase $\Pi_{\rm pl}^2$ and even make it positive, thus leading to the variable conversion failure. To avert the danger, in this case the energy transfer is turned off. Our test simulations show that this allows to almost

completely eliminate the conversion failures even in problems with extremely high σ.

In smooth regions away from current sheets, the numerical heating of plasma can be undesirable. Thus, one may opt not to transfer the numerically dissipated energy of the FFDE system to the perturbation system even if $\delta\mathcal{E}^{n+1}_{(0)} > 0$. In such smooth regions, $\delta\mathcal{E}^{n+1}_{(0)}$ is significantly smaller than in current sheets and this can be used to design a suitable switch-off criterion. In our code, we implemented the energy transfer condition

$$\delta\mathcal{E}^{n+1}_{(0)} > \alpha_{\rm e}\mathcal{E}^{n+1}_{(0)}\,, \tag{50}$$

where the switch-off parameter $\alpha_{\rm e} \geq 0$. When $\alpha_{\rm e} = 0$, the transfer takes place whenever $\delta\mathcal{E}^{n+1}_{(0)} > 0$, and when $\alpha_{\rm e} = 1$, it is turned off completely. In most of the test simulations, we used $\alpha_{\rm e} = 10^{-3}$.

Finally, equation (46) ignores the component of $\boldsymbol{S}^{n+1}_{(0)}$ aligned with $\boldsymbol{B}^{n+1}_{(0)}$, emerging because of the computational errors. As the result, the momentum density corresponding to $\boldsymbol{B}^{n+1}_{(0)}$ and $\boldsymbol{E}^{n+1}_{(0)}$, obtained via the variables conversion algorithm,

$$\tilde{\boldsymbol{S}}^{n+1}_{(0)} = \boldsymbol{E}^{n+1}_{(0)} \times \boldsymbol{B}^{n+1}_{(0)}\,,$$

also differs from the conserved variable $\boldsymbol{S}^{n+1}_{(0)}$,

$$\delta\boldsymbol{S}^{n+1}_{(0)} = \boldsymbol{S}^{n+1}_{(0)} - \tilde{\boldsymbol{S}}^{n+1}_{(0)} \neq 0\,. \tag{51}$$

Thus, one may consider transferring not only energy but the momentum as well. We have not been able to find an suitable algorithm for this transfer, though.

3 NUMERICAL IMPLEMENTATION

To integrate the conservation laws of the split RMHD, we used a third-order finite-difference scheme. In this, we closely followed the scheme ECHO developed by Del Zanna et al. (2007) for unsplit RMHD equations. There are, however, few significant differences: (1) use of the GLM approach instead of the CT method to enforce the differential constraints (24) and (31). GLM delivers similar accuracy to CT (Mignone et al. 2010) for ideal MHD, but it is much easier to implement; (2) use of a novel third-order WENO reconstruction algorithm; (3) switching the DER operator (Del Zanna et al. 2007) off at shock waves to reduce numerical oscillations (see section 3.5 for details); and (4) new variables conversion algorithm adjusted to the peculiarities of the split RMHD equations.

3.1 GLM approach

To keep the magnetic field approximately divergence-free, we follow the method called GLM (Munz et al. 2000; Dedner et al. 2002). Hence, we introduce two additional dependent variables $\Phi_{(0)}$ and $\Phi_{(1)}$, one per each subsystems, and replace the Faraday equations (21) and (27) and the divergence-free conditions (24) and (31) with

$$\partial_t \boldsymbol{B}_{(\rm s)} + \boldsymbol{\nabla}\times\boldsymbol{E}_{(\rm s)} + \nabla\Phi_{(\rm s)} = 0\,, \tag{52}$$

$$\partial_t \Phi_{(\rm s)} + \boldsymbol{\nabla}\cdot\boldsymbol{B}_{(\rm s)} = -\kappa\Phi_{(\rm s)}\,, \tag{53}$$

where $s = 0, 1$. In the test simulation, we use $\kappa = 0.2/\Delta t$, making the e-folding time for $\Phi_{(\rm s)}$ (in the case of vanishing $\boldsymbol{\nabla}\cdot\boldsymbol{B}_{(\rm s)}$) equal to 5 integration time-steps Δt.

3.2 Time integration

Since this is a finite-difference scheme, the numerical solution $\boldsymbol{q}^n_{i,j,k}$ describes the values of variables $\boldsymbol{q}$ at the gridpoints with coordinates (x_i, y_j, z_k) at the discrete time t^n. Here, we utilize Cartesian coordinates and uniform spatial grid with $x_i = x_1 + (i-1)\Delta x$, $y_j = y_1 + (j-1)\Delta y$, and $z_k = z_1 + (k-1)\Delta z$, where $\Delta x = \Delta y = \Delta z = h$. These gridpoints can considered as central points of rectangular computational cells. The interfaces of these cells are located at $x_{i\pm1/2} = x_i \pm h/2$, $y_{j\pm1/2} = y_j \pm h/2$, and $z_{k\pm1/2} = z_k \pm h/2$. The time grid is also uniform, $t^n = t_0 + \Delta t n$ with $\Delta t = {\rm C}h$, where C is the Courant number.

The finite-difference equations have the form

$$\frac{{\rm d}\mathcal{Q}}{{\rm d}t} = \mathcal{F}(\mathcal{Q})\,, \tag{54}$$

where $\mathcal{Q}$ is a 1D, 2D, or 3D array, depending on the dimensionality of the problem. Each entry of this array is the vector $\boldsymbol{q}$ at the corresponding gridpoint. $\mathcal{F}$ is an array of the same dimension and size as $\mathcal{Q}$. Each entry of this array is the numerical finite-difference approximation for $-\boldsymbol{\nabla}\cdot\boldsymbol{f} + \mathcal{S}_{\rm Q}$ at the corresponding gridpoint, where $\mathcal{S}_{\rm Q}$ is the vector of source terms. In the case of Cartesian coordinates, the source terms emerge only in the GLM equations. The system of ODEs (55) is integrated using third-order strong stability preserving version of the Runge–Kutta method (Shu & Osher 1988). Hence,

$$\mathcal{Q}^{n+1} = \mathcal{Q}^n + \frac{\Delta t}{6}(k_1 + k_2 + 4k_3)\,, \tag{55}$$

where

$$k_1 = \mathcal{F}(\mathcal{Q}^n)\,,$$
$$k_2 = \mathcal{F}(\mathcal{Q}^n + \Delta t\, k_1)\,,$$
$$k_3 = \mathcal{F}\left(\mathcal{Q}^n + \frac{\Delta t}{4}(k_1 + k_2)\right)\,.$$

The finite-difference approximation for $\boldsymbol{\nabla}\cdot\boldsymbol{f}$ is computed in the following steps:

(i) Conserved variables are converted into the primitive variables. This is needed because interpolating conserved variables may yield an unphysical state.

(ii) A third-order WENO interpolation is used to setup Riemann problems at the cell interfaces.

(iii) HLL Riemann solver (Harten, Lax & van Leer 1983) is used to find upwind flux densities $\boldsymbol{f}$ at the interfaces.

(iv) Central quartic polynomial interpolation is used to reconstruct the distribution of $\boldsymbol{f}$ in each coordinate direction and hence to find the third-order approximation for $\boldsymbol{\nabla}\cdot\boldsymbol{f}$ (DER operation of Del Zanna et al. 2007). This works fine for smooth solutions, but may introduce oscillations at shocks, often leading to crashes in high-σ regime. To avoid this, the computational domain is scanned for shock fronts and a 'safety zone' is set around them. Within the safety zone, a second-order total variation diminishing (TVD) interpolation is used instead of the WENO interpolation.

3.3 Third-order WENO interpolation

WENO interpolation invokes linear combination of lower order substencil polynomials to achieve a higher order accuracy in smooth sections of numerical solution and lower order almost-non-oscillatory interpolation in rough sections (shocks, Liu, Osher & Chan 1994; Shu 2020). This is achieved by making the weights of the polynomials dependent on some quantitative roughness indicators. WENO approach have enjoyed great success over the years, especially after its efficient implementation by Jiang & Shu (1996). Later, however, it was found that their non-linear weights have a drawback, resulting in significant reduction of accuracy in smooth

regions with critical points. Since realistic numerical models often involve local extrema in numerous locations, especially in the case of turbulent flows, this is a major disadvantage. Ha et al. (2020) proposed new weights for third-order WENO interpolation. Their test results look impressive, but the approach is not intuitive and hard to comprehend. Henrick, Aslam & Powers (2005) derived new weights for fifth-order WENO interpolation via mapping the original weights of Jiang & Shu (1996) to the improved set. Here, we adopt a similar strategy to derive an improved set of weights for a third-order scheme. In particular, we start with the weights of the second-order TVD scheme (Falle 1991), modify it to address the issue of critical points, and then use these TVD weights to produce 3rd-order WENO weights (see Appendix A).

Below, only the interpolation in the x-direction is considered, and all other spatial indices are dropped for brevity. In the other directions, the procedure is the same.

3.4 Hyperbolic fluxes

Given the left $\boldsymbol{u}^l$ and right $\boldsymbol{u}^r$ states at the interface, the flux density normal to the interface is computed using the approximate Riemann solver by Harten et al. (1983). Namely,

$$\boldsymbol{f}_n = \frac{a^+ \boldsymbol{f}_n^l + a^- \boldsymbol{f}_n^r}{a^+ + a^-} - a^+ a^- \frac{\boldsymbol{q}^r - \boldsymbol{q}^l}{a^+ + a^-}\,, \tag{56}$$

where $\boldsymbol{f}_n^{l,r} = \boldsymbol{f}_n(\boldsymbol{u}^{l,r})$, $\boldsymbol{q}^{l,r} = \boldsymbol{q}(\boldsymbol{u}^{l,r})$, and

$$a^\pm = \max(0, \pm\lambda_n^\pm(\boldsymbol{u}^l), \pm\lambda_n^\pm(\boldsymbol{u}^r)), \tag{57}$$

where $\lambda_n^\pm$ are the speeds of fastest hyperbolic modes moving relative to plasma in the positive and negative directions along the normal to the interface. We use separate wave speeds for the FFDE and perturbation subsystems. For the FFDE subsystem, $\lambda_n^\pm = \pm 1$. For the perturbation subsystem, we use the speeds of fast magnetosonic waves (as in unsplit RMHD equations). These are computed using the computationally cheap approximation

$$\lambda_n^\pm = \frac{(1-a^2)v_n \pm \sqrt{a^2(1-v^2)\left[(1-v^2a^2) - (1-a^2)v_n^2\right]}}{1 - v^2a^2}\,, \tag{58}$$

where

$$a^2 = c_s^2 + c_\mathrm{A}^2 - c_s^2 c_\mathrm{A}^2\,, \tag{59}$$

c_s is the sound speed, c_A is the Alfvén speed, and v_n is the velocity component normal to the interface (Gammie, McKinney & Tóth 2003). The HLL solver is stable and diffusive. Its diffusivity can be a drawback, but it is also a strength. It helps to smoothout the numerical solution in complex regions with non-monotonic spatial variations of large amplitude, where large truncation errors may lead to an unphysical set of conserved variables.

3.5 Finite-difference approximation for the flux divergence

Given the array of upwind fluxes at cell interfaces, we look for a third-order accurate approximation for $\nabla\cdot\boldsymbol{f}$ at the cell centres (gridpoints). To simplify the presentation, consider a gridline aligned with the x- direction, choose a particular gridpoint on this line, reset its index to zero, and measure the position of other points relative to this one, so that $x_0 = 0$. Then, introduce the four-point stencil $S = \{x_{-3/2}, x_{-1/2}, x_{1/2}, x_{3/2}\}$ centred on this gridpoint, denote the corresponding upwind fluxes in the direction of the gridline as $\{\boldsymbol{f}_{-3/2}, \boldsymbol{f}_{-1/2}, \boldsymbol{f}_{1/2}, \boldsymbol{f}_{3/2}\}$, and use the third-order interpolating polynomial $\boldsymbol{p}(x) = \boldsymbol{a}_3 x^3 + \boldsymbol{a}_2 x^2 + \boldsymbol{a}_1 x + \boldsymbol{a}_0$ to reconstruct the distribution of $\boldsymbol{f}$ around $x = 0$. Its derivative $\mathrm{d}\boldsymbol{p}/\mathrm{d}x(0) = \boldsymbol{a}_1$ gives us the require third-order approximation for $\partial_x \boldsymbol{f}_0$. It is easy to verify that the final results is

$$\partial_x \boldsymbol{f}_0 = \frac{9}{8}\frac{\boldsymbol{f}_{1/2} - \boldsymbol{f}_{-1/2}}{\Delta x} - \frac{1}{8}\frac{\boldsymbol{f}_{3/2} - \boldsymbol{f}_{-3/2}}{3\Delta x}\,. \tag{60}$$

Using a somewhat different approach, Del Zanna et al. (2007) derived this result (where it is called the DER step) in a different form. Restoring the normal cell indexation, it reads

$$\partial_x \boldsymbol{f}_i = \frac{(\boldsymbol{F}_{i+1/2} - \boldsymbol{F}_{i-1/2})}{\Delta x}\,, \tag{61}$$

where

$$\boldsymbol{F}_{i+1/2} = -\frac{1}{24}\boldsymbol{f}_{i+3/2} + \frac{26}{24}\boldsymbol{f}_{i+1/2} - \frac{1}{24}\boldsymbol{f}_{i-1/2}\,. \tag{62}$$

Equation (61) is the same form as in finite-volume schemes for conservation laws, where the place of $\boldsymbol{F}$ is taken by the interface flux $\boldsymbol{f}$ at the cell interface. This tells us that this finite-difference scheme provides an exact conservation to the integral quantities computed via the second-order accurate approximation

$$\int_v \boldsymbol{q}\mathrm{d}V \approx \sum_{i,j,k} \boldsymbol{q}_{i,j,k}\Delta V_{i,j,k}\,. \tag{63}$$

This approximation is neither upwind nor ENO/WENO, and hence may, and does, introduce oscillations at strong shocks. In the high-σ regime, these oscillations can be fatal, resulting in a failure of the variable conversion. For this reason, we implemented a strong-shock-finder algorithm and, in a safety zone around them, replace (61) with

$$(\partial_x \boldsymbol{f})_i = \frac{\boldsymbol{f}_{i+1/2} - \boldsymbol{f}_{i-1/2}}{\Delta x}\,. \tag{64}$$

This is a step towards the second-order TVD scheme, like in Komissarov (1999), which allows to prevent the shock oscillations almost completely.

The strong-shock identification algorithm is currently based on these two criteria.

(1) The central difference approximation is used to estimate the three-divergence of $\boldsymbol{u} = \gamma\boldsymbol{v}$ at the tested gridpoint. It is required to be negative with

$$|\nabla\cdot\boldsymbol{u}| > \alpha_u u\,,$$

where $\alpha_u > 0$ is a strength factor, and u is the amplitude of $\boldsymbol{u}$ at this point.

(2) The same approximation is used to estimate the gradient of total pressure $p_\mathrm{tot} = p + (B^2 + E^2)/2$. It it required to satisfy the condition

$$|\nabla p_\mathrm{tot}| > \alpha_p p\,,$$

where $\alpha_p > 0$ is another strength factor, and p is the value of gas pressure at this point. The p_tot variation pressure is compared against the gas pressure p, because in the high-σ regime, the relative variation of magnetic pressure can remain low even at strong shocks, where other flow parameters change significantly. In the test simulations, we use, $\alpha_u = \alpha_p = 0.5$.

One can make one more step and replace even the WENO interpolation with the TVD interpolation in the safety zone.

3.6 Variables conversion

For the FFDE subsystem, the conversion is relatively straightforward and already described in Section 2.4. For the perturbation subsystem,

$B_{(1)}$ and $\Phi_{(1)}$ are both the primitive and conservative at the same time and do not need converting. Thus, we need to compute the primitive variables p, ρ, w, $\boldsymbol{v}$, and $\boldsymbol{E}_{(1)}$ given the conservative variables $\mathcal{E}_{(1)}$, $\boldsymbol{S}_{(1)}$, D, the values of $B_{(1)}$, $B_{(0)}$, and $E_{(0)}$, the equation of state $w = w(p, \rho)$, and the perfect conductivity equation (32). Using the conductivity equation one can easily eliminate $\boldsymbol{E}_{(1)}$ from the set of unknowns. It is also relatively easy to eliminate one of the thermodynamic variables using the equation of state (7). Then, one can use the Newton–Raphson method to solve the remaining system of five equations for the five unknowns, but it is rather slow due to the high dimensionality of the problem. However, we have found a way to reduce the number of equations. The key first step of this algorithm is the recombination of the conserved variables of the FFDE and perturbation system. This yields the conserved variables of the unsplit RMHD system and hence allows to use any of the existing methods for the conversion of its variables. Here, we adapt the approach described by Del Zanna et al. (2007).

The recombination of conserved variables may have an adverse effect on the accuracy of the conversion, as in the high-σ regime this involves the mixing of very large and very small terms. However, the induction equation (32) alone already reintroduces the terms quadratic in $B^2_{(0)}$ and $E^2_{(0)}$ into the expressions for $\mathcal{E}_{(1)}$ and $\boldsymbol{S}_{(1)}$, and so the mixing issue exists in any case. So anyway, extra care has to be taken in order to avoid unnecessary loss accuracy in conversion calculations. After lengthy calculations described in Appendix B, the conversion problem is reduced to finding the root of the transcendental equation

$$F(X, W(X)) = 0\,, \tag{65}$$

where $X = u^2 - u_0^2$, $u^2 = v^2\gamma(v)^2$, and $u_0^2 = v_0^2\gamma(v_0)^2$, where $\boldsymbol{v}_{(0)} = \boldsymbol{E}_{(0)} \times \boldsymbol{B}_{(0)}/B^2_{(0)}$ is the drift velocity of the FFDE subsystem, and $W = w\gamma^2$. The function $F(X, W)$ is defined by the equation

$$F(X, W) = W^2v^2 + 4\bar{\mathcal{E}}_1 W + 4(P(W, X) - W)\left(W + \frac{B^2}{2}\right) - A\,, \tag{66}$$

where

$$A = S^2_{(1)} + 2(\boldsymbol{S}_{(1)}\cdot\boldsymbol{S}_{(0)}) - 2\hat{\mathcal{E}}_1 B^2 - B^2_{(0)}v_0^2(B^2_{(1)} + 2(\boldsymbol{B}_{(0)}\cdot\boldsymbol{B}_{(1)}))\,, \tag{67}$$

$$\bar{\mathcal{E}}_1 = \mathcal{E}_{(1)} + \frac{E^2_{(0)}}{2} - \frac{B^2_{(1)}}{2} - (\boldsymbol{B}_{(0)}\cdot\boldsymbol{B}_{(1)})\,, \tag{68}$$

and

$$\hat{\mathcal{E}}_1 = \mathcal{E}_{(1)} - \frac{B^2_{(1)}}{2} - (\boldsymbol{B}_{(0)}\cdot\boldsymbol{B}_{(1)})\,, \tag{69}$$

are constants, and

$$P(W, X) = \frac{1}{\kappa}(W/\gamma^2 - D/\gamma)\,, \tag{70}$$

is the function describing the gas pressure as a function of the enthalpy and flow speed. In these equations, B^2 is the squared magnitude of the total magnetic field $\boldsymbol{B} = \boldsymbol{B}_{(0)} + \boldsymbol{B}_{(1)}$.

The function $W(X)$ is defined as the positive root of the cubic equation

$$W^3 + a_2(X)W^2 + a_0 = 0\,, \tag{71}$$

where

$$a_2(X) = \frac{A_1(X) + A_2}{A_3(X)} \tag{72}$$

where

$$A_1(X) = \frac{B^2_{(0)}X}{2(1+u^2)(1+u^2_{(0)})} + \frac{v^2}{2}(B^2_{(1)} + \boldsymbol{B}_{(0)}\cdot\boldsymbol{B}_{(1)}) + \frac{D}{\gamma\kappa}\,,$$

$$A_2 = -\mathcal{E}_{(1)} + \frac{B^2_{(1)}}{2} + \boldsymbol{B}_{(0)}\cdot\boldsymbol{B}_{(1)}\,,$$

$$A_3(X) = 1 - \frac{1}{\gamma^2\kappa}\,,$$

and

$$a_0 = -\frac{1}{2}\frac{(\boldsymbol{S}_{(0)}\cdot\boldsymbol{B}_{(1)} + \boldsymbol{S}_{(1)}\cdot\boldsymbol{B})^2}{A_3(X)}\,. \tag{73}$$

Del Zanna et al. (2007) used W and v^2 as their iteration variables. We opted for $X = u^2 - u^2_{(0)} \in [-u^2_{(0)}, +\infty)$ instead of v^2, and hence $\gamma^2 = \gamma^2(X)$ and $u^2 = u^2(X)$, to increase the accuracy in computation of the cubic coefficient a_2. If we used v^2, the calculations of $A_1(v^2)$ would involve the subtraction $v^2 - v^2_{(0)}$, resulting in a significant loss of accuracy when $v^2 \approx v^2_{(0)} \approx 1$. In the high-$\sigma$ regime, this error would further increase due to the multiplication by the large factor $B^2_{(0)}$.

Since $a_0 \leq 0$, this cubic equation always has one non-negative real root. This root vanishes only when $a_2 > 0$ and $a_0 = 0$. When $a_2 < 0$, this is the only real root of the cubic. Obviously, finding accurate numerical value for the root is important for the accuracy of the whole conversion algorithm. If $a_2 < 0$, it is sufficient to use the modified Cardano's method as described in Press et al. (1992), though one has to avoid numerical subtraction of almost equal large terms when computing the discriminant of the reduced cubic when $|a_0/a_2^3| \ll 1$. The first step of this method involves depression of the cubic via introduction of the new variable $Y = W + a_2/3$. When $a_2 > 0$ and $|a_0/a_2^3| \ll 1$, the positive root $W \ll a_2$, and computing it via $W = Y - a_2/3$ involves significant loss of accuracy. In this case, we follow Blinn (2006) and introduce another variable $\bar{Y} = 1/W$, which also reduces the cubic equation to the depressed form, but no shift is involved. After this, the standard prescription is used again.

Equation (65) is solved numerically via either the secant or the Brent–Dekker method (Dekker 1969; Brent 1971). The secant method is tried first, using the value of X in the solution at the previous time-step as the initial guess. When σ is not extremely large, this method finds the root $X \geq -u_0^2$, provided it exists, down to the rounding error (machine precision) after no more than 10 iterations. When σ is very high, it may fail to converge, getting trapped in an oscillation about the root. Whenever the secant method fails, the Brent–Dekker method is tried instead. To start the method, one has to find an interval $[a, b]$, with $a \geq -u_0^2$, which includes the root, and hence $F(a)F(b) < 0$. We start with a reasonably narrow interval containing the initial guess first, and then, if it does not contain the root, exponentially decrease the distance between a and $-u_0^2$ and exponentially increase the distance between a and b. When such interval is found, the method always converges to the root, though in extreme cases this may take up to 60 iterations to reach the rounding-error level.

To test the conversion algorithm, we used the Monte-Carlo method, first to set up the exact parameter state within the parameter space, and then to produce the initial guess. Fig. 1 shows the relative error in the gas pressure against the magnetization σ, for one of such tests. Given the extreme values of σ used in the test and not a single incident of convergence failure, we are almost 100 per cent certain that when the variables conversion fails in real simulations, this is not due to some deficiencies of the conversion algorithm, but because the root $X \geq -u_0^2$ does not exist.

Once the root of equation (65) is found, the primitive variables are computed via

$$u^2 = X + u_0^2, \quad v^2 = u^2/(1+u^2), \quad w = W(X)/\gamma^2 \tag{74}$$

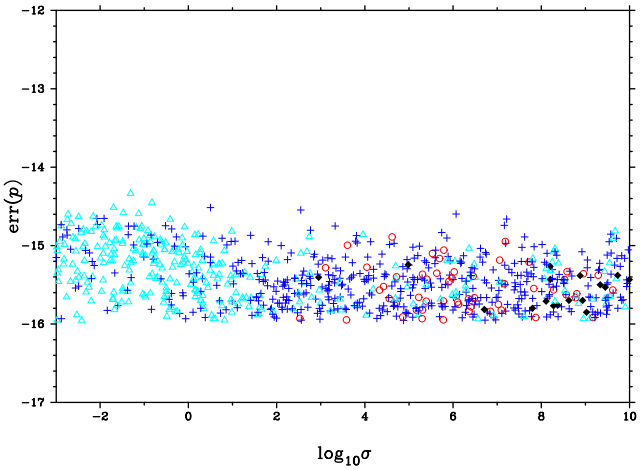

Figure 1. Relative error of pressure in the variables conversion algorithm. The type of plotting marker describes the number of iterations $n_{\rm it}$ required: green triangles when $n_{\rm it} \leq 5$, blue crosses when $5 < n_{\rm it} \leq 10$, red circles when $10 < n_{\rm it} \leq 20$, and black diamonds when $n_{\rm it} > 20$.

$$\rho = \frac{D}{\gamma}\,, \tag{75}$$

$$p = \frac{1}{\kappa}(w-\rho)\,, \tag{76}$$

$$\boldsymbol{v} = \frac{\boldsymbol{S} + (\boldsymbol{S}\cdot\boldsymbol{B})\boldsymbol{B}/W}{B^2+W}\,, \tag{77}$$

and

$$\boldsymbol{E}_{(1)} = -\boldsymbol{v}\times\boldsymbol{B} - \boldsymbol{E}_{(0)}\,. \tag{78}$$

4 1D TEST SIMULATIONS

In the simulations, we use the EoS of ideal gas with the ratio of specific heats $\Gamma = 4/3$, even when the sound speed is well below the speed of light. In all the simulations, the Courant number $\mathrm{C} = 0.5$, with the exception of the Alfvén wave test where $\mathrm{C} = 0.4$.

4.1 Alfvén wave. Convergency study

In addition to being a fundamental wave in RMHD, the Alfvén wave is a great option for testing the scheme convergency rate. It is quite complex in structure due to the rotation of electromagnetic and velocity fields, quite simple to be describe analytically even without the assumption of small amplitude (Komissarov 1997), and allows solutions with continuous higher order derivatives. In the Hoffmann–Teller frame (De Hoffmann & Teller 1950), the wave is stationary, with B^2, γ, p, ρ = const, $\boldsymbol{E} = 0$, and

$$v^i = \pm\frac{1}{\sqrt{\mathcal{E}}}B^i\,, \tag{79}$$

where $\mathcal{E} = w + B^2$, and the sign decides the direction of the wave vector.

For the test simulation, we set $p = \rho = 1$, and

$$B^x = 0.3B_0\,, \quad B^y = B_0\cos\phi\,, \quad B^z = B_0\sin\phi\,, \tag{80}$$

where the phase variable

$$\phi = \arcsin(a\sin(kx))\,.$$

To set the wave in motion, we use the Lorentz transformation to the lab frame moving with the speed $v = 0.5$ in the positive x-direction. The wavenumber k in the Hoffmann–Teller frame is set to yield the wavelength $\lambda = 2$ in the lab frame. We set the phase variation amplitude to $a = 0.3$, to ensure that the Lorentz factor does not become excessively high even for the model with the highest explored magnetization. The simulations run from $t = 0$ to 2, by which time the wave shifts to the left by exactly one half of its wavelength, and in the exact solution the profile of B^y coincides with the initial one. The Courant number is set to $\mathrm{C} = 0.4$ to ensure that in all runs of the convergency study the final time $t = 2$ is a whole number of time-steps.

Fig. 2 shows the results for the model with $B_0 = 50$, $p = \rho = 1$, with the corresponding magnetization $\sigma = 545$. Table 1 shows the results of convergency study based on this model. One can see that the scheme shows third-order behaviour already at the very low resolution. For the resolution $n_x = 20$, the characteristic variation length-scale for B^y is only five cells.

By varying the value of B_0, it s found that $L_1(B^y) \propto \sqrt{\sigma}$ and $L_1(\rho)$, $L_1(p) \propto \sigma$ when $\sigma \gg 1$.

4.2 Harris current sheet. Mechanisms of numerical plasma heating

The numerical resistivity determines the evolution of current sheets in ideal RMHD simulations, which makes this test particularly important for studying the possibility to control the numerical plasma heating associated with the resistivity as described in Section 2.4.

In the initial solution, the magnetic field $\boldsymbol{B} = (0, B^y(x), 0)$ has no guide component, and

$$B^y(x) = B_0\tanh(x/a)\,, \tag{81}$$

where a is the characteristic width of the sheet and B_0 is the asymptotic field strength. The electric field $\boldsymbol{E} = 0$ and the magnetic pressure is balanced by the gas pressure

$$p(x) = p_0 + \frac{B_0^2}{2}(1-\tanh^2(x/a))\,. \tag{82}$$

In the test problem, $B_0 = 500$, $p_0 = 1$, and $a = 0.02$. The plasma mass density is uniform $\rho(x) = \rho_0$, with $\rho_0 = 1$. The corresponding asymptotic (as $x \to \infty$) magnetization $\sigma = 54500$. The computational domain is $(-5, 5)$ with 500 gridpoints. This makes the current sheet approximately four computational cells wide, so it is resolved but only just. Such thin current sheets do emerge in the 2D simulations described in Section 5. To explore the impact of the energy transfer on the solution we made few runs with different values of the energy transfer parameter $\alpha_{\rm e}$. Here, the results for $\alpha_{\rm e} = 0$, 0.001, and 1 are presented. In many respects, they are surprisingly similar. However, there are some revealing differences concerning the energy balance.

Initially, the numerical resistivity is too high for the solution to maintain the pressure balance. Both the magnetic and total pressures in the middle of sheet reduce, and this triggers fast rarefaction waves moving out at almost the speed of light. These waves initiate plasma flow into the current sheet. Inside the current sheet, the plasma gets heated to very high temperatures, and soon the total pressure balance across the current sheet is restored. This active phase last up to $t = 0.15$, by which time the current sheet thickness increases to about six cells. This phase is followed by the phase of slow diffusive spreading, and by the end of the simulations, at $t = 5$, the current sheet thickness is still only about 10 cells (see Fig. 3).

The right panel of Fig. 3 shows the total electric field $E^z = E^z_{(0)} + E^z_{(1)}$ and its force-free and perturbation components at $t = 5$. The force-free component has the sign consistent with the flow of

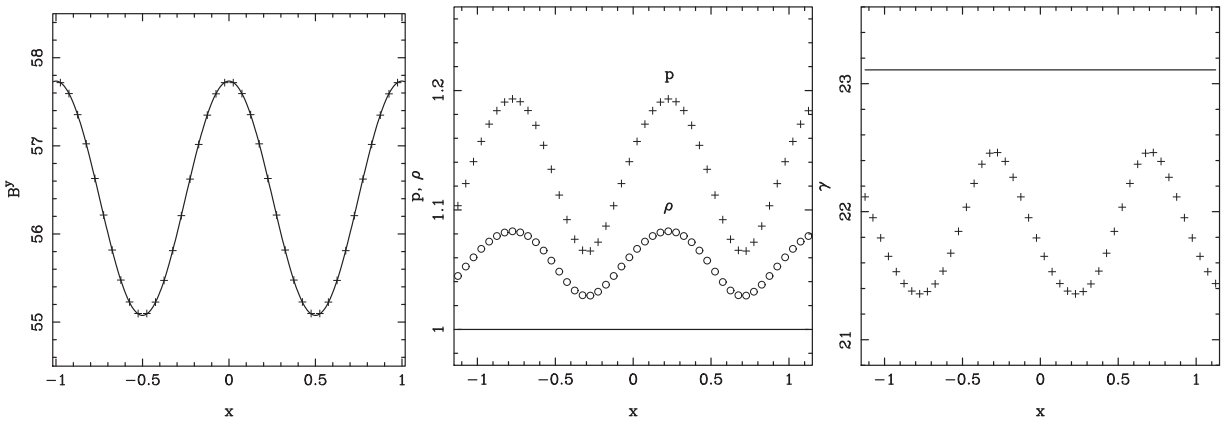

Figure 2. Alfvén wave test. The solid lines show the exact solution and markers show the numerical solution for the model with $B_0 = 50$ ($\sigma = 545$) with the resolution $n_x = 40$ at $t = 2$.

Table 1. Convergency test with Alfvén wave simulations. Here, n_x is the number of gridpoints (the resolution), n_t is the number of time-steps from the start of the run, $L_1(A)$ is the $L1$-error of the variable A, r is the two-point estimate of the order of accuracy based on the errors for the current and previous resolutions.

n_x	n_t	$L_1(B^y)$	r	$L_1(\rho)$	r	$L_1(p)$	r
20	50	0.358e−1	–	0.388e + 0	–	0.107e + 1	–
40	100	0.307e−2	3.5	0.572e−1	2.8	0.133e + 0	3.0
80	200	0.355e−3	3.1	0.755e−2	2.9	0.171e−1	2.9
160	400	0.447e−4	3.0	0.950e−3	3.0	0.214e−2	3.0
320	800	0.536e−5	3.1	0.119e−3	3.0	0.268e−3	3.0

electromagnetic energy into the current sheet. In the pure FFDE numerical solution to this problem, $E_{(0)} \approx B_{(0)}$, and the electromagnetic energy flows into the current sheet at the speed of light. Inside the current sheet, it disappears at the central discontinuity via enforcement of the condition $B > E$, In the split-RMHD simulations, the FFDE electric field $E^z_{(0)}$ is checked by the perturbation field $E^z_{(1)}$, and the total electric field E^z almost vanishes.

Fig. 4 shows the entropy $s = \ln(p/\rho^\Gamma)$, for the models with $\alpha_e = 0$, 0.001, and 1 at $t = 4$. The most conspicuous feature of these plot is the central peak. It manifests the plasma heating in the current sheet itself. In all three models, the peak has almost the same height and width. The plots also show weak 'wings', most pronounced in the model with $\alpha_e = 0$, which spread out by $\Delta x = 4$ in the both directions. This is the wake left by the fast rarefaction wave emitted by the current sheet at the start of the simulations. The left panel of Fig. 5 shows the energy transfer rate per time-step for the run with $\alpha_e = 0$ at $t = 4.5$. The central peak is the current sheet, where the numerical plasma heating continues in the central six cells. Moreover, there are additional regions of numerical heating, which are clustered around the rarefaction waves. They are responsible for the entropy wings in Fig. 4. The irregular structure of plasma heating in the rarefaction waves shows that the sign of $\delta\mathcal{E}^{n+1}_{(0)}$ fluctuates there. One may argue that like at shock waves, the numerical heating in current sheets imitates the proper physical processes known to operate there. On the contrary, its is hard to see how the numerical heating at rarefaction waves can be anything but an unwelcome numerical artefact. Fortunately, it can be suppressed by setting α_e slightly above zero. The middle panel of Fig. 5 shows that in the run with $\alpha_e = 0.001$ the energy transfer operates only in the current sheet.

Table 2 shows the variation of the total energy $\mathcal{E}_{tot} = \mathcal{E}_{em} + \mathcal{E}_{pl}$ and its components for the whole system over the whole run (up to $t = 4.5$). The integrals are computed using the conservative approximation (64),

$$\mathcal{E} = \sum_{i=1}^{n_x} \mathcal{E}_i \,, \tag{83}$$

where $\mathcal{E}_i$ is the energy density at the ith gridpoint (the cell-length factor is ignored). In the standard conservative RMHD mode of the code, the total energy of the system would remain unchanged, $\delta\mathcal{E}_{tot} = 0$ down to the rounding error, because by $t = 4.5$ the rarefaction waves have not reached the domain boundaries. The splitting scheme is not fully conservative, however, and a non-vanishing $\delta\mathcal{E}_{tot}$ is expected.

In the run with fully suppressed energy transfer ($\alpha_e = 1$), the total energy of the system decreases by about 1 per cent. Some decrease is expected because the numerical resistivity reduces the energy of the FFDE system, and this reduction is not compensated via the energy transfer algorithm. Interestingly, the plasma energy of the system still increases. Because in these simulations the bulk motion energy of plasma is very small compared to its thermal energy, this increase indicates the existence of numerical heating mechanism unrelated to the energy transfer algorithm. To understand this mechanism, recall that the conserved energy of the perturbation system $\mathcal{E}_{(1)}$ contains not only the plasma energy $\mathcal{E}_{pl} = w\gamma^2 - p$, but also the interaction energy $\mathcal{E}_{int} = (\boldsymbol{E}_{(0)}\cdot\boldsymbol{E}_{(1)}) + (\boldsymbol{B}_{(0)}\cdot\boldsymbol{B}_{(1)})$ and the energy of the electromagnetic perturbation $\mathcal{E}_{per} = (E^2_{(1)} + B^2_{(1)})/2$ (see equation 41). Hence, the plasma energy itself is not conserved. At the start of $(n+1)$th time-step, $\boldsymbol{E}^n_{(1),i} = \boldsymbol{B}^n_{(1),i} = 0$, and hence $(\mathcal{E}_{int})^n_i + (\mathcal{E}_{per})^n_i = 0$, $(\mathcal{E}_{(1)})^n_i = (\mathcal{E}_{pl})^n_i$. By the end of the time-step, $(\boldsymbol{E}_{(1)})^{n+1}_i, (\boldsymbol{B}_{(1)})^{n+1}_i \neq 0$, $(\mathcal{E}_{int})^{n+1}_i + (\mathcal{E}_{per})^{n+1}_i \neq 0$, and as a result, the plasma energy changes by $-(\mathcal{E}_{int})^{n+1}_i - (\mathcal{E}_{per})^{n+1}_i$. The corresponding change of the plasma energy for the whole system during the time-step is

$$\delta\tilde{\mathcal{E}}^{n+1}_{pl} = -\sum_{i=1}^{n_x} \left((\mathcal{E}_{int})^{n+1}_i + (\mathcal{E}_{per})^{n+1}_i\right) \,, \tag{84}$$

where the summation is taken over the whole grid. Over the whole run, this yields

$$\delta\tilde{\mathcal{E}}_{pl} = \sum_{n=2}^{n_t} \delta\tilde{\mathcal{E}}^n_{pl} \,. \tag{85}$$

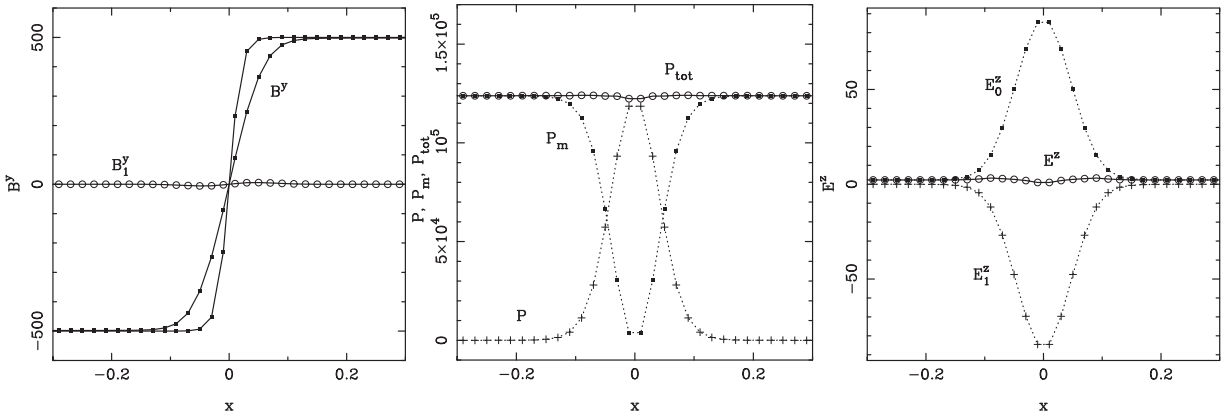

Figure 3. 1D current sheet test. Left panel: the total magnetic field B^y at t =0 and 5 and its perturbation component $B^y_{(1)}$ at $t = 5$. Middle panel: the gas pressure p, the magnetic pressure $p_{\rm m}$ and the total pressure $p_{\rm tot} = p + p_{\rm m}$ at $t = 5$. Right panel: the total electric field E^z, its FFDE component $E^z_{(0)}$ and its perturbation $E^z_{(1)}$ at $t = 5$. The energy transfer parameter is $\alpha_{\rm e} = 1$. In the models with $\alpha_{\rm e} = 0$ and 0.001, the results are very similar.

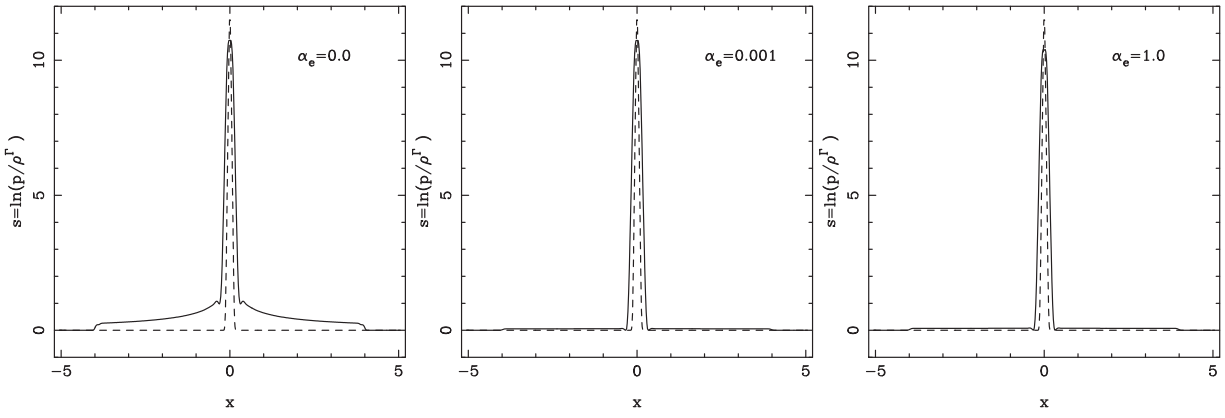

Figure 4. 1D current sheet test. The plasma entropy in the runs the energy transfer parameter $\alpha_{\rm e} = 0$, 10^{-3}, and 1. The dashed lines show the initial solution and the solid lines show the solution at $t = 4$.

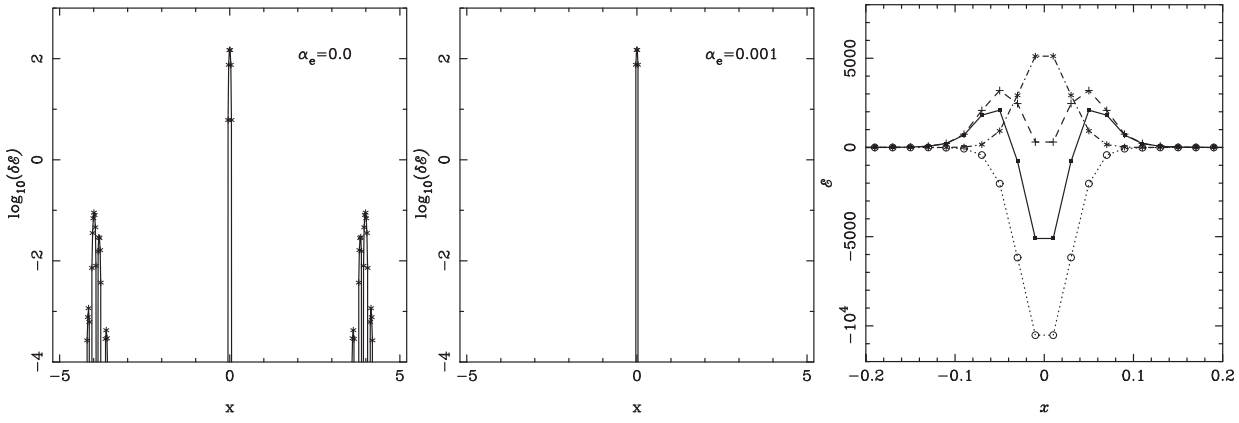

Figure 5. 1D current sheet test. Left and middle panels: plasma heating per one integration time-step at $t = 4$ for the runs with $\alpha_{\rm e} = 0$ (left panel) and $\alpha_{\rm e} = 0.01$ (middle panel). Right panel: $\mathcal{E}_{\rm int} + \mathcal{E}_{\rm per}$ (solid line and filled squares), $\mathcal{E}_{\rm per}$ (dashed line and crosses), $(\boldsymbol{B}_{(0)} \cdot \boldsymbol{B}_{(1)})$ (the dash–dotted line and stars), and $(\boldsymbol{E}_{(0)} \cdot \boldsymbol{E}_{(1)})$ (dotted line and circles) at $t = 2$ for the run with $\alpha_{\rm e} = 1$.

The value of $\delta\tilde{\mathcal{E}}_{\rm pl}$ is shown in the last column of Table 2. For the run with $\alpha_{\rm e} = 1$, $\delta\tilde{\mathcal{E}}_{\rm pl} = \delta\mathcal{E}_{\rm pl}$, confirming that in this run the plasma heating is entirely via this mechanism.

In the run with full energy transfer ($\alpha_{\rm e} = 0$), the solution is closer to the perfect energy conservation. Now $\delta\mathcal{E}_{\rm tot}$ varies by about 0.09 per cent only, and, in contrast to the run with $\alpha_{\rm e} = 1$, the total energy of the system increases. The increase of $\mathcal{E}_{\rm tot}$ in this run is expected because any deficit of $\mathcal{E}_{(0)}$ is fully compensated via increase of $\mathcal{E}_{(1)}$, but the occasional surplus of $\mathcal{E}_{(0)}$ is not compensated via decrease of $\mathcal{E}_{(1)}$. The energy transfer accounts for about 47 per cent

Table 2. 1D current sheet test. Integral energy variation by $t = 4.5$ for runs with different energy transfer parameter α_e. $\mathcal{E}_{em}$, $\mathcal{E}_{pl}$, and $\mathcal{E}_{tot}$ are the electromagnetic energy, the plasma energy, and the total energy, respectively. $\delta\tilde{\mathcal{E}}_{pl}$ is the contribution of the interaction terms to the plasma energy variation. The total energy at the start is $\mathcal{E}_{tot,0} = 6.30 \times 10^7$.

α_e	$\delta\mathcal{E}_{tot}$	$\delta\mathcal{E}_{em}$	$\delta\mathcal{E}_{pl}$	$\delta\tilde{\mathcal{E}}_{pl}$
1.0	-7.81×10^5	-1.874×10^6	1.098×10^6	1.098×10^6
10^{-2}	-9.72×10^4	-1.315×10^6	1.223×10^6	0.748×10^6
10^{-3}	4.34×10^4	-1.224×10^6	1.273×10^6	0.690×10^6
0.0	5.04×10^4	-1.222×10^6	1.294×10^6	0.689×10^6

of the plasma heating. For the run with $\alpha_e = 0.001$, the numbers are similar, with a slight improvement of the total energy conservation. For $\alpha_e = 0.01$, $\mathcal{E}_{tot}$ decreases again and its variation grows in amplitude.

In summary, the energy transfer is not the only channel of plasma heating in the splitting scheme. However, it helps to improve the energy conservation and then accounts for up to 50 per cent of plasma heating in current sheets. To suppress the low-level parasitic heating away from current sheets, it helps to introduce a threshold on the transferred energy, and in the rest of the test simulations, we use the threshold parameter $\alpha_e = 10^{-3}$ as a default value.

4.3 Degenerate Alfvén wave. The study of numerical resistivity

In the MHD approximation, basic theories of magnetic reconnection introduce diffusion of magnetic field lines through plasma using the model of scalar (isotropic) resistivity η, which is properly justified only for collisional plasma. It yields a relatively simple relation between the electric field and the electric current. In the 3 + 1 framework of resistive RMHD, this relation reads

$$\boldsymbol{j} = \frac{\gamma}{\eta}\left(\boldsymbol{E} + \boldsymbol{v}\times\boldsymbol{B} - (\boldsymbol{E}\cdot\boldsymbol{v})\boldsymbol{v}\right) + q\boldsymbol{v}\,, \tag{86}$$

where q is the electric charge density of plasma (e.g. Komissarov 2007). For electrically neutral plasma with the flow speed $v \ll 1$, this reduces to

$$\boldsymbol{j} = \frac{1}{\eta}\left(\boldsymbol{E} + \boldsymbol{v}\times\boldsymbol{B}\right),$$

which further reduces to $\boldsymbol{E} = \eta\boldsymbol{j}$ when $v = 0$. When η is constant, the magnetic field evolves according to the equation

$$\eta\left(\frac{\partial^2\boldsymbol{B}}{\partial t^2} - \nabla^2\boldsymbol{B}\right) + \left(\frac{\partial\boldsymbol{B}}{\partial t} - \nabla\times(\boldsymbol{v}\times\boldsymbol{B})\right) = 0\,. \tag{87}$$

When $\mathcal{L}/\mathcal{T} \ll 1$, where $\mathcal{L}$ and $\mathcal{T}$ the characteristic length- and time-scales of the problem, the second derivative term can be ignored and we obtain the equation of Newtonian MHD

$$\frac{\partial\boldsymbol{B}}{\partial t} - \nabla\times(\boldsymbol{v}\times\boldsymbol{B}) - \eta\nabla^2\boldsymbol{B} = 0\,. \tag{88}$$

Denote as $\mathcal{T}_\eta$ the time-scale introduced by the resistivity. Then, from equation (88), it follows that

$$\mathcal{T}_\eta = \eta^{-1}\mathcal{L}^2\,. \tag{89}$$

Since we solve equations of ideal RMHD, the only kind of resistivity available in our simulations and controlling the magnetic reconnection is the numerical one. The numerical resistivity, like the numerical diffusion and viscosity, emerges from the truncation errors of the numerical scheme. For a Runge–Kutta scheme with temporal and spatial accuracies of the same order r, the rounding error $\mathcal{R}_1$ after one time-step scales with the resolution $n_x = L/\Delta x$, where L is the domain size, as

$$\mathcal{R}^1 = \mathrm{O}(n_x)^{-(r+1)} \quad \text{as} \quad n_x \to \infty\,,$$

assuming a smooth solution (Shu & Osher 1988). However, this error is local, and for a feature of the characteristic length-scale $\mathcal{L} \ll L$, the size of the domain does not matter. What matters is $n_\mathcal{L} = \mathcal{L}/\Delta x$, the number of gridpoints per $\mathcal{L}$. Hence, the local error

$$\mathcal{R}^1_\mathcal{L} \propto n_\mathcal{L}^{-(r+1)} \quad \text{for} \quad n_\mathcal{L} \gg 1\,.$$

The number of time-steps required to reach the resistive time-scale $\mathcal{T}_\eta$ is $n_\eta = \mathcal{T}_\eta/\Delta t$ and the total error accumulated by this time is

$$\mathcal{R}^{n_\eta}_\mathcal{L} \propto n_\eta (n_\mathcal{L})^{-(r+1)} = \frac{\mathcal{L}^2}{\eta\Delta t}(n_\mathcal{L})^{-(r+1)} \quad \text{for} \quad n_\mathcal{L} \gg 1\,.$$

This accumulated error is the overall $\delta B/B$ on the resistive time-scale, and hence a constant which does not depend of the particular values of Δx, Δt, and $\mathcal{L}$. Hence,

$$\eta_{num} = A_\eta\frac{\mathcal{L}^2}{\Delta t}\left(\frac{\Delta x}{\mathcal{L}}\right)^{r+1} = A_\eta\frac{\Delta x}{\Delta t}\mathcal{L}\left(\frac{\Delta x}{\mathcal{L}}\right)^{r}, \tag{90}$$

where A_η is the normalization factor, and we replaced η with η_{num} to stress the fact this is the expression for the numerical resistivity. In this derivation, we assumed that the rounding error emerging in the numerical integration of the Faraday equation has the effect similar to that of the discretized diffusion term $\eta\nabla^2\boldsymbol{B}$. A proper analytical study of this issue is beyond the scope of this paper, and here we only check this via computer simulations. For our scheme $r = 3$, and, given the maximum wave speed being equal to the speed of light, $\Delta x/\Delta t = C^{-1}$.

The result (90) is almost identical to the special case of the ansatz proposed by Rembiasz et al. (2017), who based it on a mixture of physical and numerical reasons. Rembiasz et al. (2017) tried to determine the normalization factors of their ansatz by studying the decay of Alfvén and magnetosonic waves. The decay of these waves depends both on the numerical viscosity and resistivity, which makes the computations rather involved. Curiously, they reported negative resistivity for their numerical scheme.

Here, we simplify the procedure by studying the problem which involves only the numerical resistivity and hence no decoupling is needed. Namely, we consider the 1D initial value problem, where in the initial solution $\boldsymbol{v} = 0$, $p = p_0$, $\rho = \rho_0$, and the magnetic field $\boldsymbol{B} = B_0(0, \cos kx, \sin kx)$ rotates with x at a constant rate. In ideal RMHD, this configuration is magnetostatic due to uniform magnetic and total pressures. It may be described as a degenerate limit of the Alfvén wave, when the wave vector $\boldsymbol{k}$ is orthogonal to the magnetic field. In resistive RMHD with constant scalar resistivity, the magnetic field decays and this decay is accompanied by plasma heating. However, because of the translational symmetry of the problem, the rate of decay and heating is independent on x and the configuration remains magnetostatic.

When $\boldsymbol{v} = 0$, the magnetic field evolves according to the telegraph equation

$$\eta\frac{\partial^2\boldsymbol{B}}{\partial t^2} + \frac{\partial\boldsymbol{B}}{\partial t} - \eta\frac{\partial^2\boldsymbol{B}}{\partial x^2} = 0\,. \tag{91}$$

When $\eta k \ll 1$, it allows the separable solution

$$\boldsymbol{B}(t) = B_0(0, \cos kx, \sin kx)\exp(-\omega t)\,, \tag{92}$$

where $\omega = \eta k^2$ is the decay rate of the magnetic field [This is the same as in the Newtonian limit, where the first term in equation (91) drops out.]. Thus, if the rounding errors of our scheme do indeed

amount to numerical resistivity, one expects the magnetic field to decay exponentially, in which case the value of numerical resistivity can be found as $\eta_{\rm num} = \omega/k^2$. In the test simulations, the initial solution has $p_0 = \rho_0 = 1$, and $B_{(0)} = 50$. The domain is (0,1) with periodic boundary conditions and $C = 0.5$.

The left panel of Fig. 6 shows the evolution of the magnetic field for the model with $k = 2\pi$. As expected, the wave decays keeping its shape intact. To measure the decay rate, we use the total magnetic energy of the system, computed via equation (83), which is expected to decay exponentially at the rate $2\omega = 2\eta_{\rm num}k^2$. It is indeed exponential, as illustrated in the middle panel of Fig. 6. Table 3 shows that the decay rate, and the value of $\eta_{\rm num}$, decrease with the numerical resolution as n_x^{-3} for sufficiently large n_x, in agreement with equation (90).

The characteristic length-scale $\mathcal{L}$ is based on the equation

$$\frac{{\rm d}^2\boldsymbol{B}}{{\rm d}x^2} = \frac{\boldsymbol{B}}{\mathcal{L}^2}\,, \tag{93}$$

and for this problem it yields $\mathcal{L} = 1/k$, independent of the location. Then, equation (90) predicts $\omega \propto k^4$, which is indeed the case as illustrated in the right panel of Fig. 6.

Table 3 also shows the values of the normalization constant A_η obtained in the simulations with $k = 2\pi$. One can see that for $n_x \gtrsim 20$, $A_\eta \approx 0.031$ independently of the resolution as expected. For $n = 10$, A_η it is almost twice as high. However, in this case the number of gridpoints per the length-scale $n_{\mathcal{L}}$ is only about 1.6 and a strong deviation from equation (90) is expected. The numerical magnetic Reynolds number of the wave problem,

$$Re_m = \frac{c\mathcal{L}}{\eta_{\rm num}}\,. \tag{94}$$

4.4 Self-similar rarefaction waves

Self-similar (simple) rarefaction waves provide very useful non-linear test problems. Although no analytic solutions for these waves exist, the problem of finding exact numerical solutions is reduced to solving numerically a system of first-order ordinary differential equations (e.g. Komissarov 1999). These wave are not particularly suitable for the convergency testing because of the loss of smoothness in the exact solutions at the leading (trailing) wavefronts, where already the first spatial derivative is discontinuous. Since we have already verified the order of accuracy of our code, this is no longer required and just a visual comparison with the exact numerical solution is sufficient. Here, we present the results for a switch-off fast rarefaction and a slow rarefaction waves propagating through the same high-σ state.

4.4.1 Fast switch-off wave

This wave connects two uniforms states with the parameters $p = 1$, $\rho = 0.01$, $\boldsymbol{u} = (0, 0, 0)$, and $\boldsymbol{B} = (10, 5, 0)$ for the left state, and $p = 0.630$, $\rho = 0.7076 \times 10^{-2}$, $\boldsymbol{u} = (0.232, -0.577, 0)$, and $\boldsymbol{B} = (10, 0, 0)$ for the right state. The magnetization $\sigma \approx 30$ in both the left and the right states. The wave moves to the left, with the wave speeds of the leading and trailing fronts being $v_l = -0.9856$ and $v_t = -0.9705$, respectively. These are so close because in high-σ plasma the fast speed is very close to the speed of light, and the reduction of the tangential component of the magnetic field has little effect on the magnetization when there is a strong normal component. Another interesting property of the wave is its limited strength in terms of the gas pressure variation. This is partly due to the fact that the fast rarefaction terminates as soon as the tangential magnetic field vanishes. The initial ($t_{\rm R} = 0$) discontinuity of the associated Riemann problem is set at $x = 0$, whereas the initial ($t = t_{\rm R} - 1 = 0$) solution for the computer simulations is the exact solution to this Riemann problem at $t_{\rm R} = 1$. The domain is $(-2.20, -0.90)$ with 800 gridpoints. Fig. 7 shows the exact numerical solution (solid lines) versus the results of computer simulations (markers) at the time $t = 1$ ($t_{\rm R} = 2$). One can see that agreement between the solutions is quite good, apart from the vicinity of the leading and trailing fronts. The loss of accuracy near the fronts is expected due to the lack of continuity in the first spatial derivatives there.

4.4.2 Slow switch-on wave

This wave connects two uniforms states with the parameters $p = 1$, $\rho = 0.01$, $\boldsymbol{u} = (0, 0, 0)$, and $\boldsymbol{B} = (10, 5, 0)$ for the left state and $p = 0.001$, $\rho = 0.562 \times 10^{-5}$, $\boldsymbol{u} = (8.856, 4.479, 0)$, and $\boldsymbol{B} = (10, 5.048, 0)$ for the right state. The magnetization $\sigma \approx 30$ in the left state and $\sigma \approx 3 \times 10^4$ in the right state. The wave moves to the left, with the wave speeds of the leading and trailing fronts being $v_l = -0.516$ and $v_t = 0.876$, respectively. Thus, relative to the computational grid, the trailing front now moves to the right. The great contrast with the fast rarefaction in this regard is due to the fact that the sound speed, $c_s \approx 1/\sqrt{3}$ everywhere, is much lower than the speed of light, and so the speed of the slow mode is strongly influenced by the value of v_x. Another contrasting feature is the large decrease of the gas pressure as the solution can be continued towards $p = 0$ without limit.

The initial ($t_{\rm R} = 0$) discontinuity of the associated Riemann problem is set at $x = 0$, whereas the initial ($t = t_{\rm R} - 1 = 0$) solution for the computer simulations is the exact solution to this Riemann problem at $t_{\rm R} = 1$. The domain is $(-3, 5)$ with 100 gridpoints. This low resolution is sufficient because of the rapid spreading of the wave, in contrast to the fast wave where the spreading is very slow. Fig. 8 shows the exact numerical solution (solid lines) versus the results of computer simulations (markers) at the time $t = 3(t_{\rm R} = 4)$. Again, there is a good agreement between the solutions everywhere, apart from the vicinity of the leading and trailing fronts. The loss of accuracy near the trailing front is higher due to the higher jumps of the first derivatives there.

4.5 Shock waves

Magnetosonic shock waves present the most challenging type of RMHD solutions for standard unsplit numerical schemes in the high-σ regime. The huge variation of the spatial gradients of physical parameters at shocks even with a well-resolved numerical structure yields large numerical errors, and this increases the chance for the computed conserved variables to escape from the physically meaningful domain. The same applies to the splitting scheme. Moreover, there may be no FFDE shock solution which can be considered as a good first approximation to an RMHD shock. For example, fast waves of FFDE propagate in all directions with the speed of light, whereas for an RMHD shock on can always find a frame where it is stationary. This makes the perturbation component of the electromagnetic field ($\boldsymbol{B}_{(1)}$, $\boldsymbol{E}_{(1)}$) comparable to its FFDE component ($\boldsymbol{B}_{(0)}$, $\boldsymbol{E}_{(0)}$), particularly the electric field.

We tested numerical shock solutions obtained with our scheme against the exact solutions, obtained by solving numerically the shock equations as described in Majorana & Anile (1987). Here, the results of some of the tests are described. The corresponding solutions of the shock equations are given in Table 4.

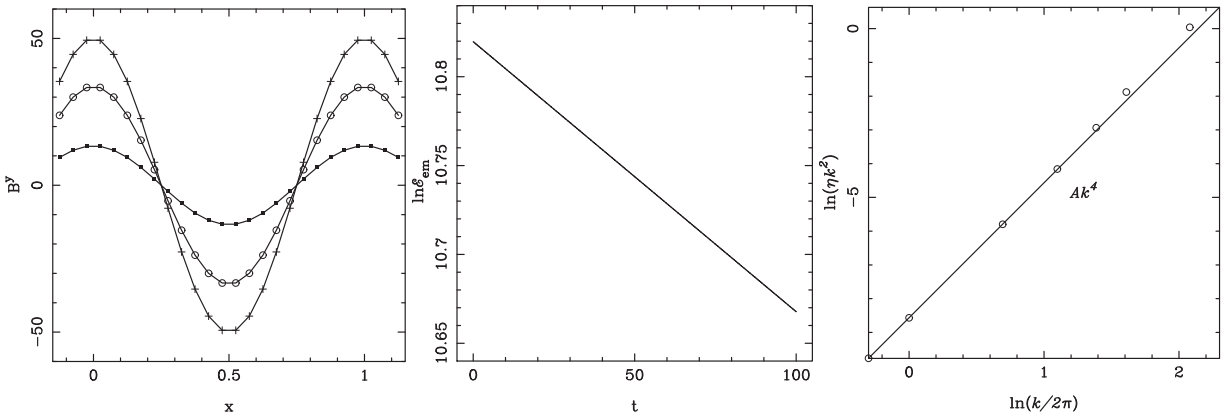

Figure 6. Degenerate Alfvén wave. Left panel: B^y at $t = 0$ (crosses), $t = 30$ (circles), and $t = 100$ (filled squares) in the run with $n_x = 20$ and $k = 2\pi$. Middle panel: evolution of the total electromagnetic energy $\mathcal{E}_{\rm em}$ in the run with $n_x = 40$ and $k = 2\pi$. Right panel: the wave decay rate $\omega = \eta k^2$ against k for the models with the resolution $n_x = 80$.

Table 3. Degenerate Alfvén wave simulations. n_x is the number of grid-points, r is the two-point estimate of the scheme order of accuracy, η is the numerical resistivity, Re_m is the magnetic Reynolds number based on the numerical resistivity, and A_η is the coefficient in the ansatz (90). The wave used for the simulations has $k = 2\pi$.

n_x	10	20	40	80
2ω	0.39	0.26×10^{-1}	0.30×10^{-2}	0.38×10^{-3}
ηnum	0.49×10^{-2}	0.33×10^{-3}	0.38×10^{-4}	0.48×10^{-5}
r	–	3.75	3.1	3
A_η	0.063	0.034	0.031	0.031
Re_m	0.32×10^2	0.48×10^3	0.42×10^4	0.33×10^5

4.5.1 *FS7. Fast shock in weakly magnetized plasma*

We start with the case of fast shock in low-σ plasma. This case is selected to demonstrate the very good performance of splitting scheme performance in the low-σ regime, even if it was designed specifically with the high-σ regime in mind. In addition, this case allows us to illustrate the inner workings of the splitting approach without resorting to sophisticated plotting techniques.

In the upstream (left) state, $p = 10^{-2}$, $\rho = 1$, and $\sigma = 10^{-3}$. The corresponding sound and Alfvén speeds are $c_s = 0.11$ and $c_{\rm A} = 0.022$, respectively. In the rest frame of the upstream state, the shock moves in the negative x-direction with the fast magnetosonic Mach number $M_f = 5$, where

$$M_f = \frac{\gamma_s v_s}{\gamma_f v_f},$$

v_s is the shock speed, v_f is the fast magnetosonic speed along the shock normal, and γ_s and γ_f are the corresponding Lorentz factors. The angle between the shock normal and the magnetic field $\alpha_{\rm B} = 45^\circ$. For the test simulations, the shock is setup in the inertial frame where it moves in the positive x-direction with the speed $v_s' = 0.1$. The domain is $(-0.5, 1.5)$ with 100 gridpoints. Initially, the shock is located at $x = 0$. Fig. 9 illustrates the solution at $t = 10$, when the shock is expected to reach $x = 1$. In its plots, the solid lines show the exact solution, and the markers show the simulation results obtained with the splitting scheme.

One can see that the shock is captured very well, both in terms of the shock speed and the jumps of the fluid parameters. The bottom-left panel shows the jump in the total magnetic field B^y and its perturbation components $B^y_{(1)}$, which vanishes in the upstream and downstream uniform states and remains quite low even at the shock front. The bottom-centre panel, shows the total electric field E^z, its FFDE component $E^z_{(0)}$, and the perturbation components $E^z_{(1)}$. The perturbation component vanishes in the upstream and downstream uniform states, where $E^z = E^z_{(0)}$. However in the shock layer, $E^z_{(0)}$ strongly deviates from E^z and develops a conspicuous upward 'spur'. The perturbation component also has a spur there but in the opposite direction, thus keeping the total electric field E^z close to the exact solution. The behaviour of $E^z_{(0)}$ is consistent with the pure FFDE solution to the Riemann problem with the same electromagnetic left and right states. The bottom-right panel of Fig. 9 illustrates this solution at $t = 0.5$. In involves two fast waves moving with the speed of light in the opposite directions, and a uniform state in between, where $E^z_{(0)} > 0$. The FFDE component of the splitting scheme attempts to evolve the total electromagnetic field in the same direction, but the perturbation component prevents it from getting there.

4.5.2 *FS9. Subrelativistic fast shock*

In this case, both the plasma temperature and magnetization are lower than in FS7, allowing to describe it as a subrelativistic problem. The results of this test show that the splitting scheme can be used to simulate such plasmas without significant decrease of accuracy. This is important as in many astrophysical applications both the ultrarelativistic and subrelativistic plasmas coexist, e.g. an accretion disc or interstellar gas next to a relativistic jet.

In the upstream (left) state, $p = 10^{-4}$, $\rho = 1$, $\sigma = 10^{-3}$, and the non-relativistic magnetization parameter $\beta = p/p_{\rm m} = 2$. The corresponding sound and Alfvén speeds are $c_s = 0.011$ and $c_{\rm A} = 0.0071$, respectively. The shock moves through this state in the negative x-direction with the fast magnetosonic Mach number $M_f = 5$. The angle between the shock normal and the magnetic field $\alpha_{\rm B} = 45^\circ$. The test simulations are setup in the rest frame of the upstream state. In this frame, the shock speed $v_s = -0.0705$. The domain is $(-0.35, 0.05)$ with 100 gridpoints. Initially, the shock is located at $x = 0$. The left panel of Fig. 10 illustrates the solution at $t = 3$, when the shock is expected to reach $x = -0.212$. In the plot, the solid lines show the prediction based of the shock speed of the exact solution, and the markers show the numerical solution obtained with the splitting scheme.

Table 4. Parameters of shock wave tests. In all the tests, the left state is the shock upstream state. σ is the magnetization of the upstream state, $M_{\rm f}$ and $M_{\rm S}$ are, respectively, the relativistic fast- and slow-magnetosonic Mach numbers of the shock, and $v_{\rm sh}$ is the shock speed relative to the grid.

Test	Left state	Right state	Other parameters
FS5	$\boldsymbol{v}$ = (0.99968283E + 00, 0, 0)	$\boldsymbol{v}$ = (0.99768146E + 00, 0.17248747E−01, 0)	$v_{\rm sh} = -0.5$
	$\boldsymbol{B}$ = (50, 0.19853866E + 04, 0)	$\boldsymbol{B}$ = (50, 0.19886156E + 04, 0)	$M_{\rm f} = 2$
	$\boldsymbol{E}$ = (0, 0, −0.19847569E + 04)	$\boldsymbol{E}$ = (0, 0, −0.19831425E + 04)	$\sigma = 10^3$
	$p = 1.0$, $\rho = 1.0$	p = 0.44243911E + 01, ρ = 0.26176303E + 01	
FS5A	$\boldsymbol{v}$ = (0, 0, 0)	$\boldsymbol{v}$ = (−0.75954175E+00, 0.16485693E + 00, 0)	$v_{\rm sh}$ = −0.99989427E + 00
	$\boldsymbol{B}$ = (50, 50, 0)	$\boldsymbol{B}$ = (50, 0.24230060E + 03, 0)	$M_{\rm f} = 2$
	$\boldsymbol{E}$ = (0, 0, 0)	$\boldsymbol{E}$ = (0, 0, 0.19228027E + 03)	$\sigma = 10^3$
	$p = 1.0$, $\rho = 1.0$	p = 0.44243911E + 01, ρ = 0.26176303E + 01	
FS7	$\boldsymbol{v}$ = (0.57368310E + 00, 0, 0)	$\boldsymbol{v}$ = (0.19727530E + 00, 0.34774998E−02, 0)	$v_{\rm sh} = 0.1$
	$\boldsymbol{B}$ = (0.22803509E−01, 0.27840482E−01, 0)	$\boldsymbol{B}$ = (0.22803509E−01, 0.13638473E + 00, 0)	$M_{\rm f} = 5$
	$\boldsymbol{E}$ = (0, 0, −0.15971614E−01)	$\boldsymbol{E}$ = (0, 0, −0.26826038E−01)	$\sigma = 10^{-3}$
	$p = 0.01$, $\rho = 1.0$	p = 0.28341867E + 00, ρ = 0.58282475E + 01	
FS9	$\boldsymbol{v}$ = (0, 0, 0)	$\boldsymbol{v}$ = (−0.57243160E−01, 0.31963724E−02, 0)	$v_{\rm sh}$ = −0.70530352E−01
	$\boldsymbol{B}$ = (0.70724819E−02, 0.70724819E−02, 0)	$\boldsymbol{B}$ = (0.70724819E−02, 0.39243124E−01, 0)	$M_{\rm f} = 5$
	$\boldsymbol{E}$ = (0, 0, 0)	$\boldsymbol{E}$ = (0, 0, 0.22690067E−02)	$\sigma = 10^{-4}$
	$p = 10^{-4}$, $\rho = 1.0$	p = 0.34131551E−02, ρ = 0.52994146E + 01.	
SS1	$\boldsymbol{v}$ = (0.19953950E + 00, 0, 0)	$\boldsymbol{v}$ = (−0.42122856E+00, −0.63382468E + 00, 0)	$v_{\rm sh} = -0.5$
	$\boldsymbol{B}$ = (50, 0.51026147E + 02, 0)	$\boldsymbol{B}$ = (50, 0.50825161E + 02, 0)	$M_{\rm S}$ = 2.101839785
	$\boldsymbol{E}$ = (0, 0, −0.10181732E + 02)	$\boldsymbol{E}$ = (0, 0, −0.10282225E + 02)	$\sigma = 10^3$
	$p = 1.0$, $\rho = 1.0$	p = 0.14412306E + 02, ρ = 0.58792375E + 01	

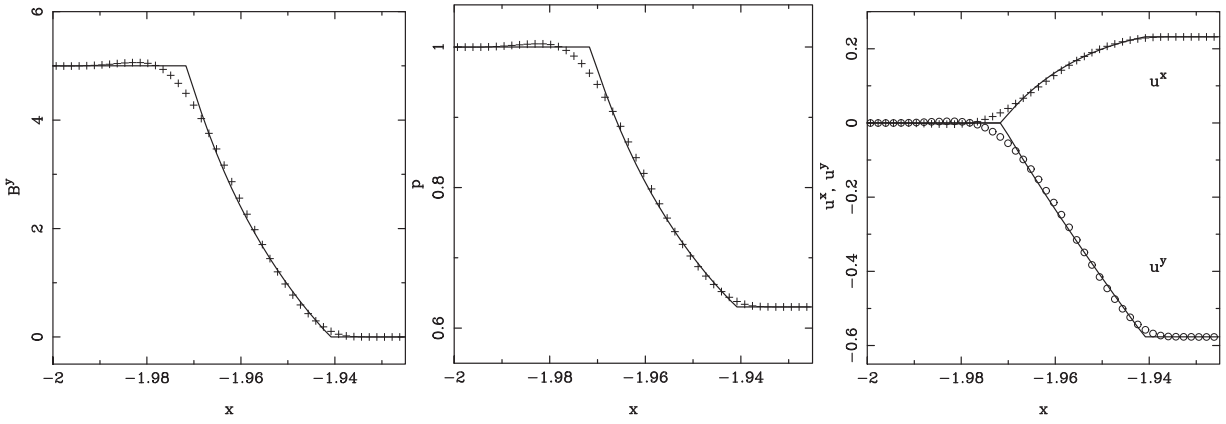

Figure 7. Fast switch-off rarefaction wave test. The continuous lines show the exact solution, and the markers show the numerical solution at the integration time $t = 1$, corresponding to the time $t_{\rm R} = 2$, since the resolution of the initial discontinuity.

4.5.3 FS5. Fast shock in highly magnetized plasma

This is an example of fast shock in highly magnetized plasma. In the rest frame of the upstream state, $p = \rho = 1$ and $\sigma = 10^3$. The shock moves through this state in the negative x-direction with the fast magnetosonic Mach number $M_f = 2$. The shock speed in this frame is $v_s = -0.99968$, and the angle between the shock normal and the magnetic field $\alpha_{\rm B} = 45^\circ$. The test simulations are setup in the frame where the shock speed is $v_s' = -0.5$. The domain is $(-5.5, 0.5)$ with 300 gridpoints. Initially, the shock is located at $x = 0$. The middle panel of Fig. 10 illustrates the solution at $t = 10$, when the shock is expected to reach $x = -5.0$. In the plot, the solid lines show the exact solution, and the markers show the results of computer simulations. Once again both the shock speed and its jumps are well captured by the splitting scheme. When the energy transfer algorithm is turned off, the errors increase. In particular, the gas pressure is about 20 per cent lower. The plot also shows a slight shift of the numerical solution relative to the exact one, implying the possibility of a small error in the shock speed. However, this shift is

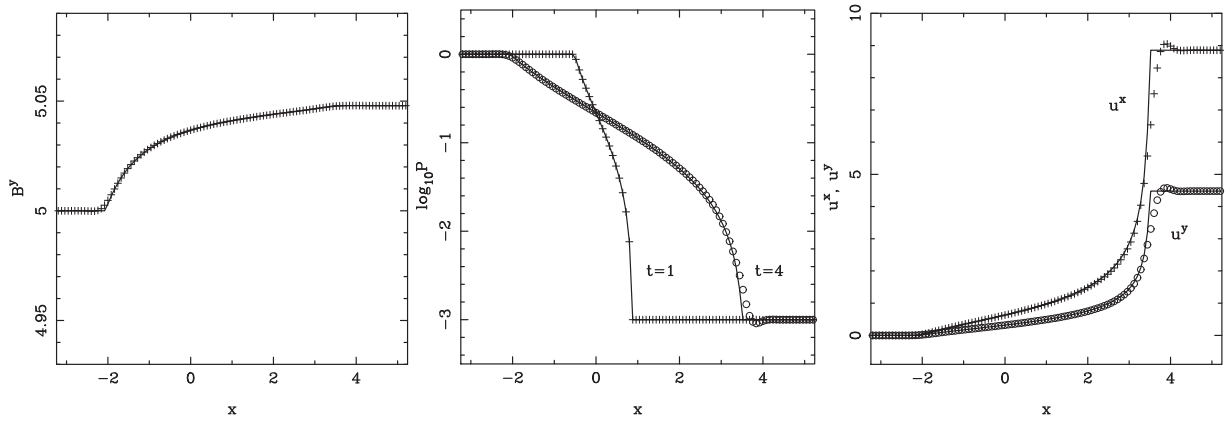

Figure 8. Slow rarefaction wave test. The continuous lines show the exact solution, and the markers show the numerical solution at the integration time $t = 3$, corresponding to $t = 4$, since the resolution of the associated Riemann discontinuity. The middle panel also shows the exact solution at the Riemann time $t = 1$, which served as an initial solution for this test.

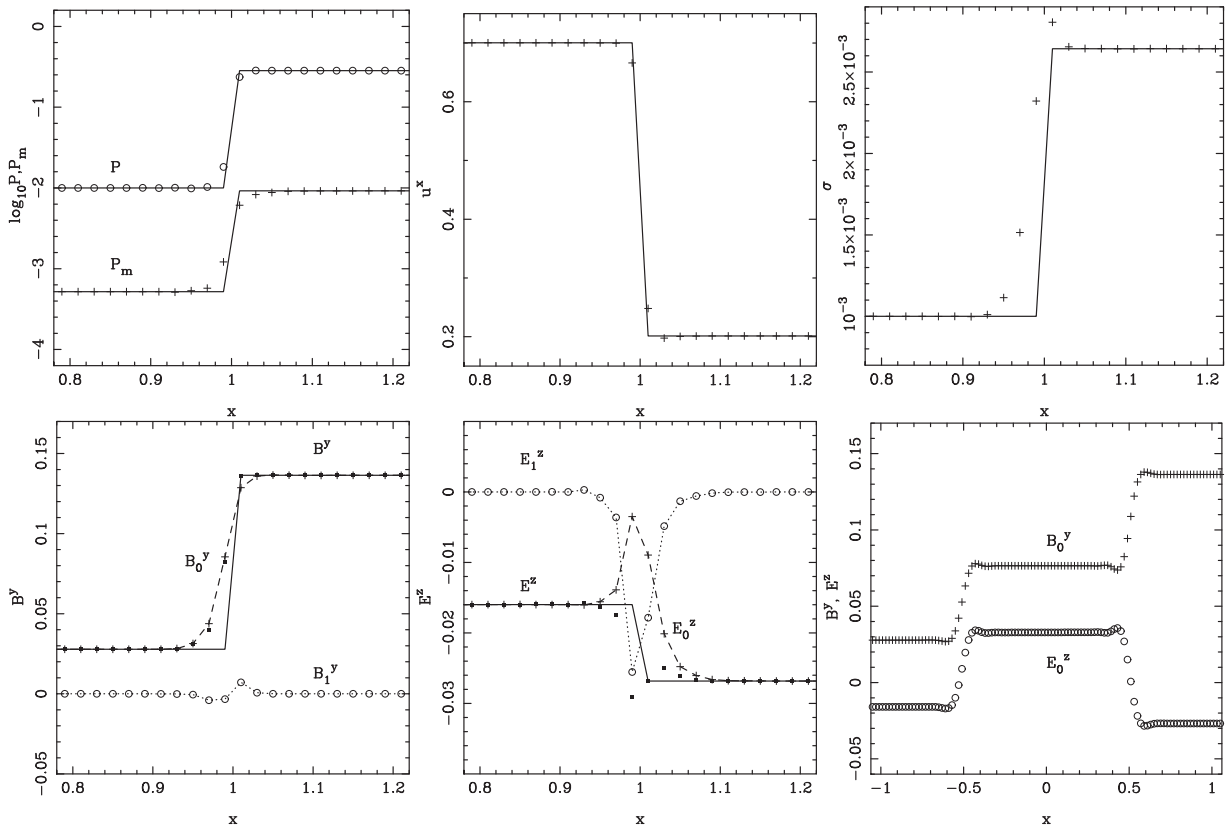

Figure 9. Fast shock FS7 of weak magnetization. $t = 10$. The bottom-right panel shows the FF electrodynamic solution at $t = 0.5$ for the same initial conditions.

already seen at $t = 2$, where it has the same size. This suggests that the shift is more likely a property of the numerical shock structure.

4.5.4 SS. Slow shock in highly magnetized plasma

This is an example of slow shock in highly magnetized plasma. The upstream state is exactly the same as the FS5 example. The shock moves through this state in the negative x-direction with the slow magnetosonic Mach number $M_f = 2.1$, the shock speed in this frame is $v_s = -0.63$. The test simulations consider the flow in the rest frame where the shock speed is $v_s' = -0.5$. The domain is $(-1.5, 0.5)$ with 100 gridpoints. Initially, the shock is located at $x = 0$. The right panel of Fig. 10 illustrates the solution at $t = 10$, when the shock is expected to reach $x = -5.0$. In the plot, the solid lines show the prediction based of the shock speed of the exact solution, and the markers show the numerical solution obtained with the splitting scheme. One can see that this shock is also well captured. The small 'separation' between the curves of the exact and numerical solutions does not increase with time and seems to have the same origin as in the case FS5.

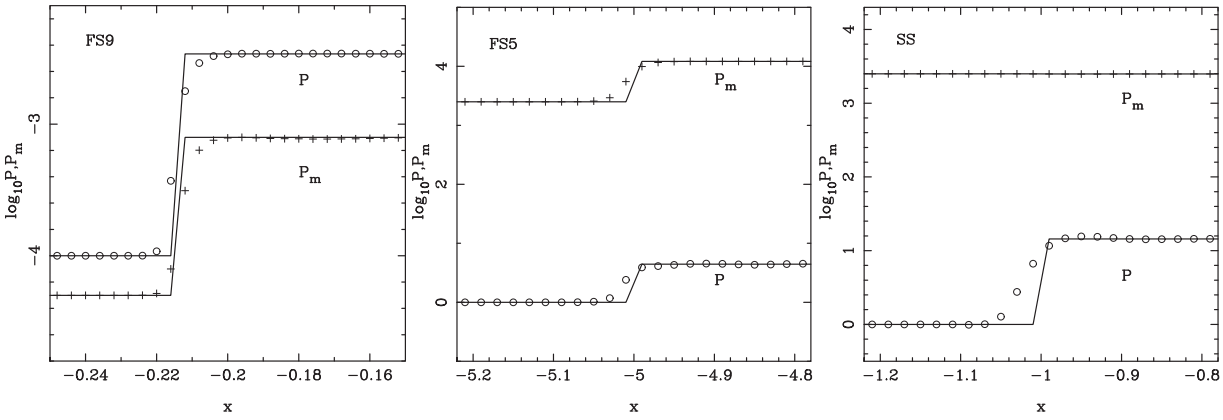

Figure 10. Left panel: subrelativistic shock FS9 at $t = 3$. Middle panel: fast shock FS5 of strong magnetization at $t = 10$. Right panel: slow shock SS of strong magnetization at $t = 2$. All these shocks are initially located at $x = 0$.

4.5.5 FS5A. Fast shock in highly magnetized plasma

This is a problematic case where the numerical solution suffers from large computational errors. The shock is the same as FS5 but now the simulations are set in the rest frame of its upstream state.

The results are illustrated by Fig. 11. As far as the electromagnetic field is concerned the numerical solution is quite accurate, with the shock speed and jumps across the shock being captured quite well (see the left panel of Fig. 11). The plasma parameters, however, show very large errors. As one can see in the middle panel of Fig. 11, the gas pressure of the numerical solution overshoots the pressure of the exact solution by more than 10 times.

One probable reason for the large errors is the very large shock speed, $v_s = -0.99968$. At such a speed, the non-linear steepening is extremely slow and hence not as efficient at balancing the magnetic field diffusion due to numerical resistivity as in slower shocks. As a result, the shock structure keeps spreading out until the numerical diffusion becomes sufficiently reduced. The spreading is accompanied by excessive numerical heating of plasma, which explains the high gas pressure of shocked plasma. This interpretation is consistent with the fact that the heating is particularly intense at the start of the simulation when the shock is just beginning to develop its numerical structure. Moreover, switching off the energy transfer allows to reduce the amount of numerical heating, which also supports this interpretation. The latter does not cure the problem, however, because the energy transfer is not the only mechanism of plasma heating (see Section 4.2). Using smooth shock profile in the initial solution does not help much either.

In addition to the extremely fast motion relative to the grid, the FS5A shock is characterized by much stronger jump of the tangential component of the magnetic field across the shock than in the FS5 shock. If in the FS5 case, $\Delta B^y \approx 3$, in the FS5A it is $\Delta B^y \approx 2 \times 10^2$, leading to about 100 times stronger numerical magnetic dissipation.

Summarizing the results of our 1D shock wave tests, the splitting method captures strong shocks quite well, especially in the low-σ regime. However, in the high-σ regime, very fast shocks with large jumps of magnetic field are problematic.

5 2D TEST SIMULATIONS

We used some of the 1D tests problems described in Section 4 in setups aligned with the x- and y-directions to make sure that the results of 1D tests are reproduced with the 2D code. These tests do not reveal anything new and their results are not described in this section, where only the results of inherently 2D problems are presented. All the 2D simulations are carried out in Cartesian coordinates.

5.1 Magnetic rope

Lundquist's magnetic rope is a steady-state axisymmetric force-free magnetic configuration, where the magnetic pressure and tension perfectly balance each other (Lundquist 1950). In our simulations of a stationary rope, the force-free equilibrium is preserved, subject to slow numerical diffusion and magnetic dissipation. Here, we present the results of a more challenging problem, where the rope moves along the x- direction with a relativistic speed.

In the rest frame of the rope, its magnetic field is given by

$$\begin{cases} \tilde{B}^x = -B_0 \dfrac{y}{r} J_1\left(\alpha \dfrac{r}{r_0}\right), \\ \tilde{B}^y = B_0 \dfrac{x}{r} J_1\left(\alpha \dfrac{r}{r_0}\right), \\ \tilde{B}^z = B_0 J_0\left(\alpha \dfrac{r}{r_0}\right), \end{cases} \tag{95}$$

where r_0 is the rope radius. In these equations, J_n are Bessel's functions, α is the first root of J_1, and $r = \sqrt{\tilde{x}^2 + \tilde{y}^2}$ is the radial distance from the rope axis (Lundquist 1950). Outside of the rope, for $r > r_0$, $\boldsymbol{B} = (0, 0, B_0 J_0(\alpha))$. The gas pressure and density are uniform.

The initial solution for the rope moving with the speed v in the x-direction, is obtained using the Lorentz transformation for the electromagnetic field $\{\boldsymbol{E}, \boldsymbol{B}\}$ and the Lorentz length contraction $x = \tilde{x}/\gamma$. The model parameters of the test simulations are $B_0 = 100$, $r_0 = 1$, $p = 1$, $\rho = 1$, and $v = 0.8$. The corresponding magnetization reaches $\sigma \approx 2000$ in the centre of the rope. The domain is $(-2, 2) \times (-2, 2)$ with 200 uniformly spaced gridpoints in each direction. The periodic boundary conditions are used at both the x and y boundaries.

Fig. 12 compares the numerical solution with the exact solution at $t = 5$, by which time the rope has crossed the domain twice and returned to its initial position. In the left panel, the colour map shows the distribution of σ at $t = 5$. The plot also includes two sets of contour lines of the magnetic flux function, one set for $t = 0$ and another for $t = 5$. These are indistinguishable in the plot. The middle panel shows the pressure distribution at $t = 5$. Here, one can clearly see the numerical errors, which in places reach eight per cent. In the

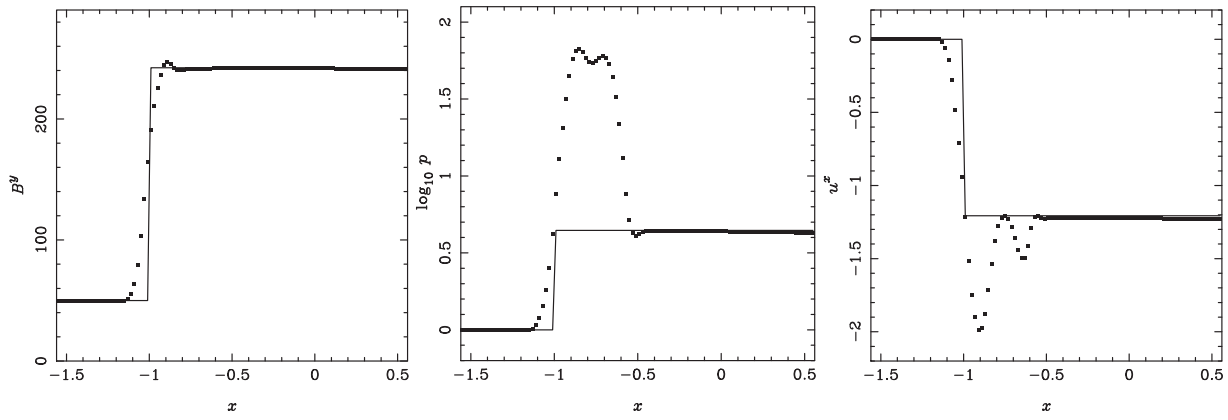

Figure 11. Fast shock FS5A of strong magnetization at $t = 1$. The plots the solutions for B^y (left panel), gas pressure p (middle panel), and u^x (right panel). The solid lines show the exact solutions and the marker show the numerical solution.

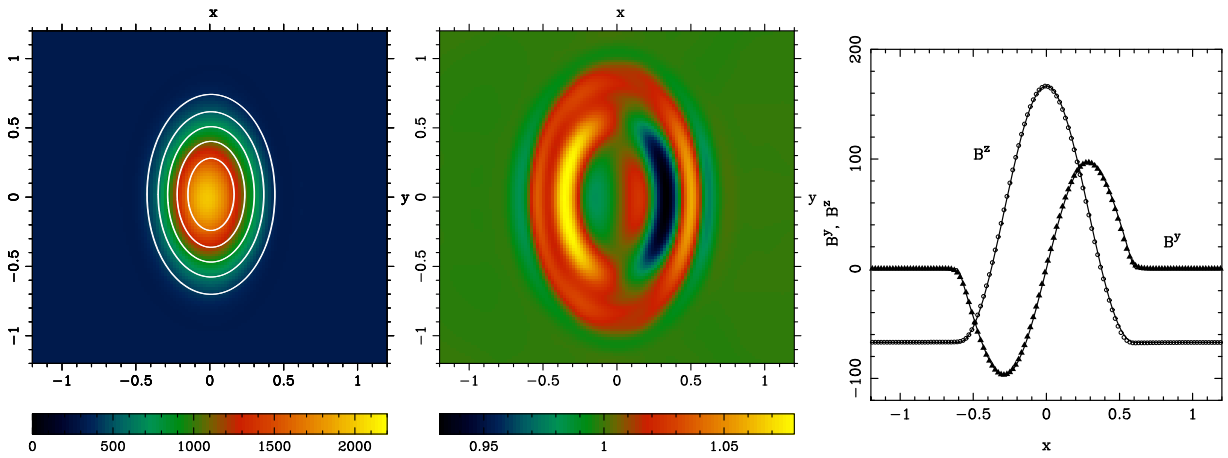

Figure 12. Magnetic rope. Left panel: magnetization parameter σ and magnetic field lines. The image shows σ at $t = 5$. Superimposed are two sets of five magnetic field lines, one for $t = 0$ and another for $t = 5$. They are indistinguishable. Middle panel: gas pressure p at $t = 5$. Right panel: magnetic field along the line $y = 0$. The markers show the numerical solution, and the solid lines show the exact solution at $t = 5$.

right panel, the magnetic field in the numerical solution along the line $y = 0$ (markers) is compared to the magnetic field in the exact solution. Here, the errors are hardly visible.

5.2 Oblique degenerate Alfvén wave. Anisotropy of numerical resistivity

Here, we return to the problem of Section 4.3 and consider the case where the wave vector points at 45° to the x-axis. The aim is to evaluate the anisotropy of the numerical resistivity relative to the computational grid. For such an obliqueness, the solution (92) reads

$$\boldsymbol{B}(t) = B_0 \left(-\frac{1}{\sqrt{2}} \cos\phi(x, y, k), \frac{1}{\sqrt{2}} \cos\phi(x, y, k), \sin\phi(x, y, k) \right) \times \exp(-\omega t)\,, \tag{96}$$

where $\phi = (k/\sqrt{2})(x + y)$ and $\omega = \eta k^2$.

In the test simulations, the domain is $(0, 1) \times (0, 1)$, with equal resolutions in the x- and y-directions, and the periodic boundary conditions. These boundary conditions are satisfied only for the wavenumbers $k_n = 2\sqrt{2}\pi n$, $n \in Z$. The model parameters are the same as in the 1D simulations, $B_0 = 50$, $\boldsymbol{v} = \boldsymbol{0}$, $p = 1$, and $\rho = 1$. Table 5 shows the results obtained for the wave with $k = 2\sqrt{2}\pi$ and the same resolution as in the 1D test. Comparing these results with the 1D results for the wave with $k = 2\pi$, given in Table 3, one can see that the resistivities are exactly the same. Since $\eta \propto k^2$, this means that for the same wavenumber the resistivity in the oblique case is smaller by the factor of 2.

Table 5. Oblique degenerate Alfvén wave simulations. $n_x = n_y$ is the numerical resolution, η is the numerical resistivity, and A_η is the normalization factor in equation (97).

$n_x = n_y$	10	20	40	80
$2\eta k^2$	0.39	0.026	0.0030	0.00038
ηnum	0.50×10^{-2}	0.33×10^{-3}	0.38×10^{-4}	0.48×10^{-5}
A_η	0.064	0.034	0.031	0.031

Clearly, the resistivity must be a smooth periodic function $f(\theta)$ of the angle θ between the wave vector $\boldsymbol{k}$ and the unit vector $\boldsymbol{e}_x$ of the x-direction, with the period of $\pi/2$. Moreover, it must be symmetric with respect to the angles $\theta_s = n\pi/4$, $n \in Z$, so that $f(\theta_s + a) = f(\theta_s - a)$. The simplest function satisfying these conditions is

$$\eta\text{num} = \frac{\eta_0}{4}(3 + \cos 4\theta)\,. \tag{97}$$

where η_0 is given by equation (90).

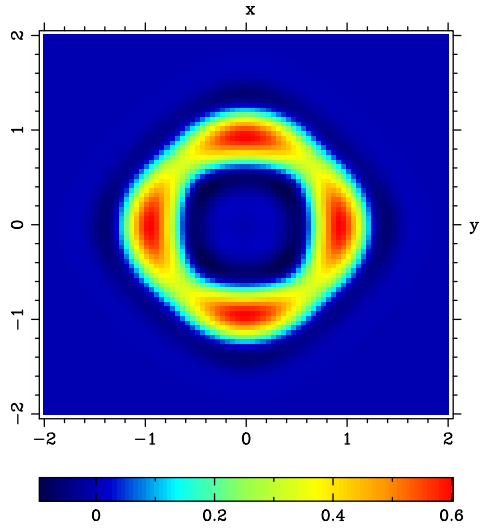

Figure 13. Anisotropy of numerical resistivity. Entropy distribution in the simulations of stationary magnetic rope at $t = 10$.

To explore this issue a little bit further, we inspected the results of the stationary magnetic rope simulations (see Section 5.1) for the signs of anisotropic resistivity. The entropy $s = \ln p/\rho^{\Gamma}$ of the exact solution is uniform. However, the plasma heating associated with the numerical resistivity is expected to yield a non-uniform distribution $s(r, \theta)$, which is periodic in θ and peaks along the x- and y-axes. This is exactly what is observed in these simulations (see Fig. 13.)

5.3 Cylindrical explosion in uniform magnetic field

This is now a standard test problem for RMHD codes (e.g. Komissarov 1999; Leismann et al. 2005; Mignone & Bodo 2006; Del Zanna et al. 2007). In the initial solution of this problem, a cylindrical volume filled with plasma of very high pressure and temperature (the result of an explosion) is surrounded by plasma of low pressure and density. To make the problem more interesting, the whole space is threaded with a uniform magnetic field directed perpendicular to the cylinder, which breaks the axial symmetry of the problem. Although there is no exact analytic solution to this problem, one can compare the results of simulations to the solutions obtained with other numerical methods.

Following Komissarov (1999), the density and pressure of the surrounding plasma are set to $\rho_{\rm e} = 10^{-4}$ and $p_{\rm e} = 3 \times 10^{-5}$. The hot cylinder is centred on the z-axis and has the radius $r_0 = 0.9$. Its density and pressure are set to $\rho_0 = 10^{-2}$ and $p_0 = 1$, respectively. The initial jumps of both the gas pressure and its density are soften with the same tanh-profile

$$f(r) = \frac{1}{2}[(f_0 - f_{\rm e})\tanh((r - r_0)/\Delta r) + (f_0 + f_{\rm e})]\,, \qquad (98)$$

where $\Delta r = 0.03$. The simulation domain is $(-6, 6) \times (-6, 6)$, with 400 uniformly spaced gridpoints in each direction. We explored four models with $B_0 = 0.01$, 0.1, 1.0, and 10^3.

The top row of Fig. 14 illustrates the solution for the model with the magnetic field strength $B_0 = 0.01$ at $t = 4$. The corresponding magnetization is $\sigma_0 = 2.5 \times 10^{-5}$ inside the cylinder and $\sigma_{\rm e} = 0.45$ in its surroundings. The magnetic pressure is very low compared to the gas pressure in the cylinder, with $\beta_0 = 2 \times 10^4$, and for some time the magnetic field has little influence on the solution. This is manifested in the central symmetry of the images in this figure. One can spot the slightly lower flow Lorentz factor and the slightly lower density of the shocked shell along the y-axis, indicating that the magnetic field is beginning to have a noticeable effect on the solution at $t = 4$. The second row of Fig. 14 illustrates the solution for the model with $B_0 = 0.1$. The corresponding magnetization is $\sigma_0 = 2.5 \times 10^{-3}$ ($\beta_0 = 2 \times 10^2$) inside the cylinder, and $\sigma_{\rm e} = 45.0$ in its surrounding. In this model, the magnetic field is sufficiently strong to have a pronounced effect on the solution, slowing down the flow expansion in the y-direction. This leads to the spectacular morphology reminiscent of an eye, which was seen in the test simulations by many other research groups. The third row illustrates the solution for the model with $B_0 = 1$. The corresponding magnetization is $\sigma_0 = 2.5 \times 10^{-1}$ ($\beta_0 = 2$) inside the cylinder and $\sigma_{\rm e} = 4.5 \times 10^3$ in its surroundings. Now the magnetic is so strong that it prevents the hot plasma from expanding in the y-direction and the explosion proceeds almost entirely along the magnetic field lines. The weak fast shock, however, still has a cylindrical shape, thanks to the fast speed being very close to the speed of light in all directions. One can also see that the magnetic are still a bit distorted by the explosion. The bottom row shows the solution for $B_0 = 10^3$. The corresponding magnetization is $\sigma_0 = 2.5 \times 10^5$ ($\beta_0 = 2 \times 10^{-6}$) inside the cylinder and $\sigma_{\rm e} = 4.5 \times 10^9$ in its surroundings. In this case, the distortion of magnetic field lines is so weak that it cannot be seen with a naked eye, and to visualize the fast shock we had to plot not the magnetic pressure $p_{\rm m}$, but $p_{\rm m} - p_{\rm m,0}$, where $p_{\rm m,0} = 5 \times 10^5$ is the initial magnetic pressure. For this model, a couple of first time-step had to be done with a smaller Courant number, $C = 0.1$. This was needed for the shock identification subroutine to capture the forward shock before the errors associated with the DER step became too high. We also run a model with $B_0 = 10^4$. There we had to use even smaller C and for a larger number of time-steps before switching back to the standard $C = 0.5$. The results for this model were almost indistinguishable from the results for $B_0 = 10^3$.

In the models with $B_0 = 0.01$ and 0.1, the magnetization is sufficiently low to be handled with the standard RMHD codes. The case with $B_0 = 0.1$ is a particularly popular test. On visual inspection, the results obtained for this test with the splitting scheme look indistinguishable from those obtained with standard conservative schemes previously (e.g. Komissarov 1999; Leismann et al. 2005; Mignone & Bodo 2006; Del Zanna et al. 2007). For a more detailed comparison, and to compare like with like, we run this model in the standard RMHD mode of our code (see Section 2.3). The results are illustrated in the middle panel of Fig. 15 which shows the distributions of B^x along the line $x = 0$, with the line corresponding to the solution obtained in the standard mode and markers to the solution obtained in the splitting mode. They are so close that one may think that both the line and the markers show the same solution. The same applies to other parameters. We did the same comparison for the model with $B_0 = 0.01$. This case is interesting, because the magnetic field is very weak and far from being in a force-free configuration. Given the fact that the splitting approach involves advancing the electromagnetic component using the FFDE approximation, one could anticipate large errors in $\boldsymbol{B}$. However, this is not the case, as illustrated in the left panel of Fig. 15. The solution obtained using the splitting approach is still almost indistinguishable from solution obtained with the standard approach.

The model with $B_0 = 1$ seems to be at the border line or already beyond the capabilities of the standard approach. Although one of us presented results for this model in the past (Komissarov 1999), which actually look quite similar to what is shown in Fig. 14, they were unable to reproduce this result later on request, indicating some unusual undocumented tweaking of the code. The simulations in the standard mode of the current code also crashed.

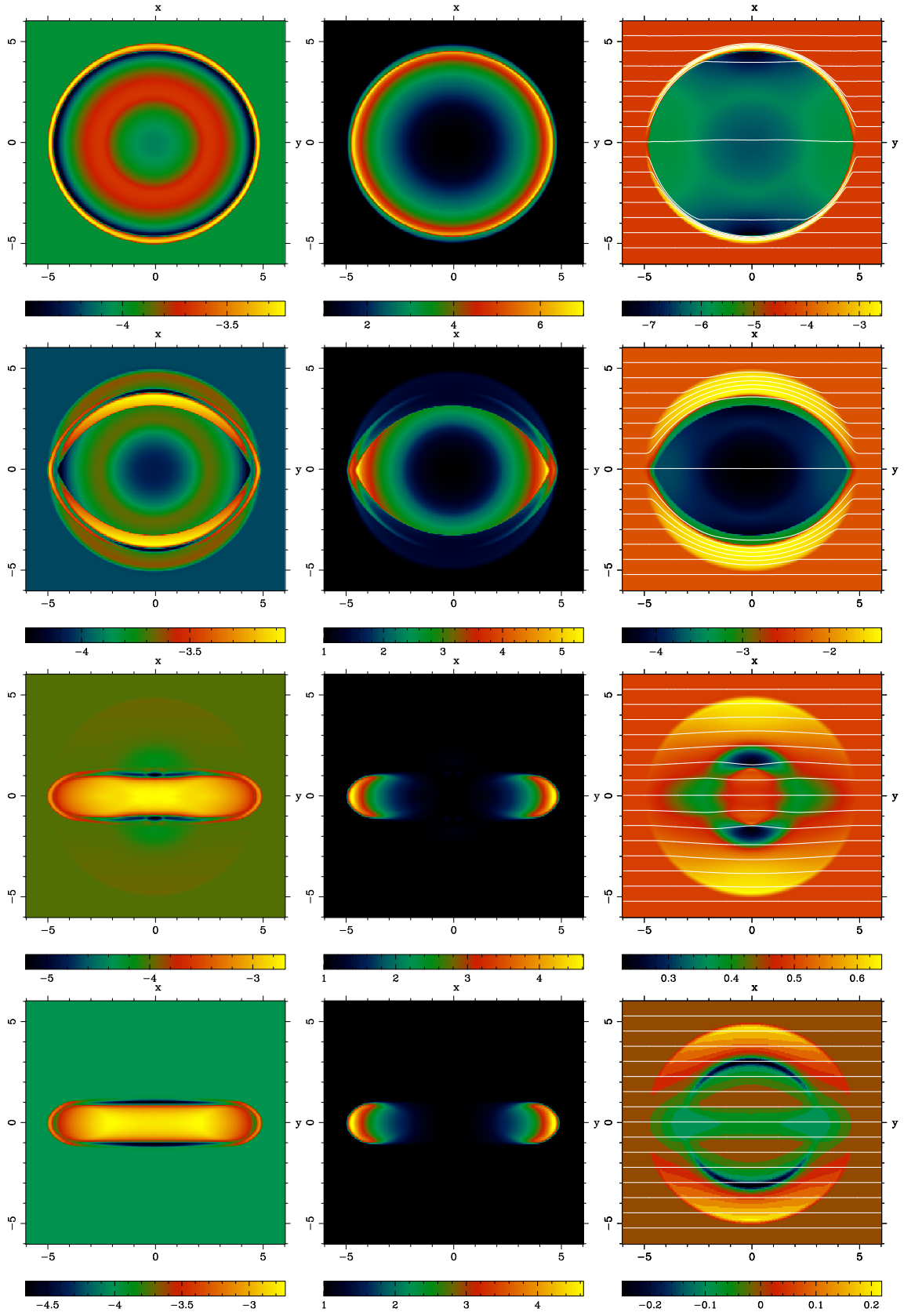

Figure 14. Cylindrical explosion. From top to bottom, solutions for the models with $B_0 = 0.01, 0.1, 1.0$, and 1000 at $t = 4$. Left panels: $\log_{10}\rho$; middle panels: Lorentz factor γ; and right panels: the magnetic field lines and $\log_{10} p_{\rm m}$ for $B_0 = 0.01$ and 0.1, $p_{\rm m}$ for $B_0 = 1$ and $\delta p_{\rm m} = p_{\rm m} - 5 \times 10^5$ for $B_0 = 1000$.

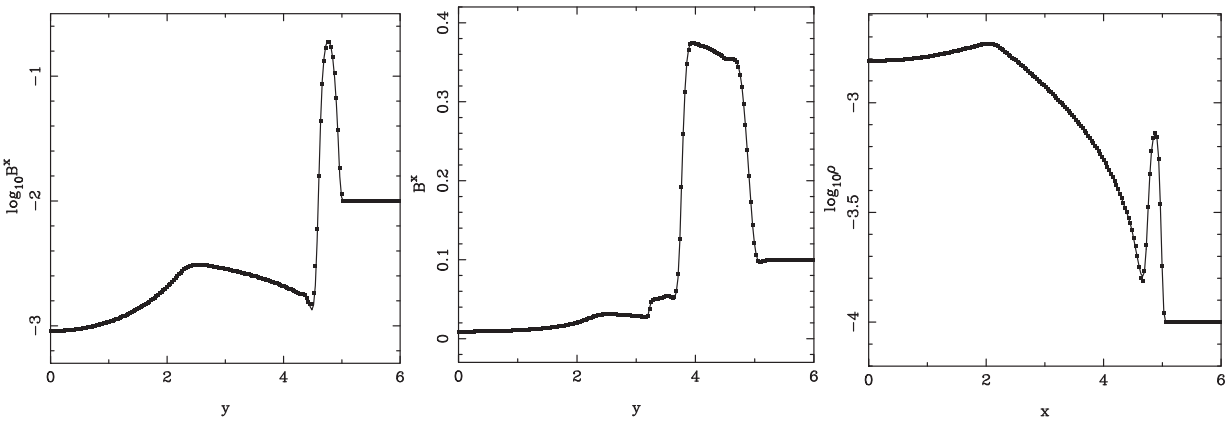

Figure 15. Cylindrical explosion. Splitting approach versus standard RMHD scheme. Left panel: B^x along the line $x = 0$ at $t = 4$ solutions for model with $B_0 = 0.01$. The solid line shows the solution obtained with the standard approach and the markers show the solution obtained with the splitting approach. Middle panel: B^x along the line $x = 0$ at $t = 4$ for the model with $B_0 = 0.1$. The solid line shows the solution obtained with the standard approach and the markers show the solution obtained with the splitting approach. Right panel: $\log_{10}\rho$ along the line $y = 0$ at $t = 4$ for the model with $B_0 = 1000$. Markers show the 2D solution obtained with the splitting approach and the solid line shows the solution for unmagnetized 1D flow in the problem with the same initial distribution of flow parameters along the x-axis.

The model with $B_0 = 1000$ is much more extreme than the one with $B_0 = 1$, and the simulations in the standard mode expectedly failed. However, because the magnetic field of this model remains highly uniform, a comparison with the solution of a different kind suggests itself. Since the flow is basically 1D, one may check it against the Cartesian 1D HD ($B = 0$) solution with the same initial distribution of pressure and density. This 1D HD solution is particularly close to the 2D solution along the $y = 0$. The symmetry of the 2D problem implies that $y = 0$ is a magnetic field line, and hence both the magnetic and electric forces along it vanish. Thus, the flow along this line is driven solely by the gas pressure force. The two solutions are compared in the right panel of Fig. 15, showing the distribution of ρ along the line $y = 0$. As expected, they look almost indistinguishable from each other.

Following Del Zanna et al. (2007), we used the $B_0 = 0.1$ model on the 200×200 grid to benchmark the performance of our code. It was compiled with *gfortran* using the O optimization option, which does not allow automatic parallelization, and was run on a single core of the Apple M2 3.49GHz processor. It took 24 cpu seconds (134 time-steps) to reach $t = 4$. In the standard RMHD mode, the code was only about 20 per cent faster. At $t = 4$, the variable conversion takes about 36 per cent of the computational time.

5.4 Tearing instability of Harris current sheet

In this test, the initial solution describes a Harris current sheet, with the $\boldsymbol{B} = (B^x, 0, 0)$, where

$$B^x = B_0 \tanh \frac{y}{a}\,, \tag{99}$$

and the gas pressure

$$p = p_0 + \frac{B_0^2}{2}\left(1 - \tanh^2 \frac{y}{a}\right)\,, \tag{100}$$

where a is the half-thickness of the current sheet, and p_0 and B_0 are the asymptotic values (as $y \to \pm\infty$) of the B^x and p, respectively. In addition, $\rho = \rho_0$ and $\boldsymbol{v} = \boldsymbol{0}$. The computational domain is $(-1, 1) \times (-1, 1)$ with 400 uniformly spaced gridpoints in the both directions, periodic boundary conditions in the x-direction and zero-gradient boundary conditions in the y-directions. The zero-gradient boundary conditions result in artefacts near the y boundaries, which become noticeable in log-scale plots towards the end of the simulations. However they remain at sufficiently low amplitude and do not influence the sheet dynamics.

The parameters used in the simulations are $p_0 = \rho_0 = 1$, $B_0 = 500$, and $a = 0.01$. The corresponding asymptotic value of plasma magnetization $\sigma_0 = 5 \times 10^4$. The selection of the very small value for a is determined by the intention of setting as thin current sheet as allowed by the numerical resistivity. The value of numerical resistivity in the current sheet can be estimated using equation (90). The corresponding length-scale, as determined by equation (94),

$$\mathcal{L} = \frac{a}{\sqrt{2}} \cosh \frac{x}{a}\,,$$

now depends on the location. At $x = a$, $\mathcal{L} \approx 0.009$, and with $A_\eta = 0.034$, equation (90) yields $\eta_{\rm num} \approx 10^{-4}$. The corresponding resistive time-scale $\tau_\eta = a^2/\eta \approx 1$, whereas the Alfvén time-scale based on the half-length $L = 1$ of the current sheet, $\tau_{\rm A} = L/c = 1$. Given that $\tau_\eta \propto a^4$, even a moderately smaller value of a would result in rapid thickening of the sheet.

5.4.1 Linear phase

The equilibrium is perturbed by introducing the vertical component of magnetic field

$$B^y = \sum_{j=1}^{20} A_j \sin\left(\frac{\pi j}{L}x + 2\pi r_j\right)\,, \tag{101}$$

where $A_j = 10^{-5} B_0$, and $0 < r_j < 1$ is a random number.

The right panel of Fig. 16 shows the function $B^y_{max}(t)$ obtained in the simulations. Using the expected exponential growth of a single eigenmode $B^y_{max}(t) \propto e^{\omega t}$, we find $\omega \approx 2.7$ for $0 < t < 1$, $\omega \approx 2.0$ for $1 < t < 2$, and $\omega \approx 1.7$ for $2 < t < 3$. The variation could be related to the thickening of the current sheet from $a = 0.01$ at $t = 0$ to $a \approx 0.013$ at $t = 0.5$, $a \approx 0.015$ at $t = 1.5$, and $a \approx 0.016$ at $t = 2.5$ (see the middle panel of Fig. 16). According to the theory of tearing instability, the maximum growth rate occurs for the mode with the wavenumber $k_{\rm m}$, given by the equation

$$k_{\rm m} a \approx 1.4\, S^{*-1/4}\,, \tag{102}$$

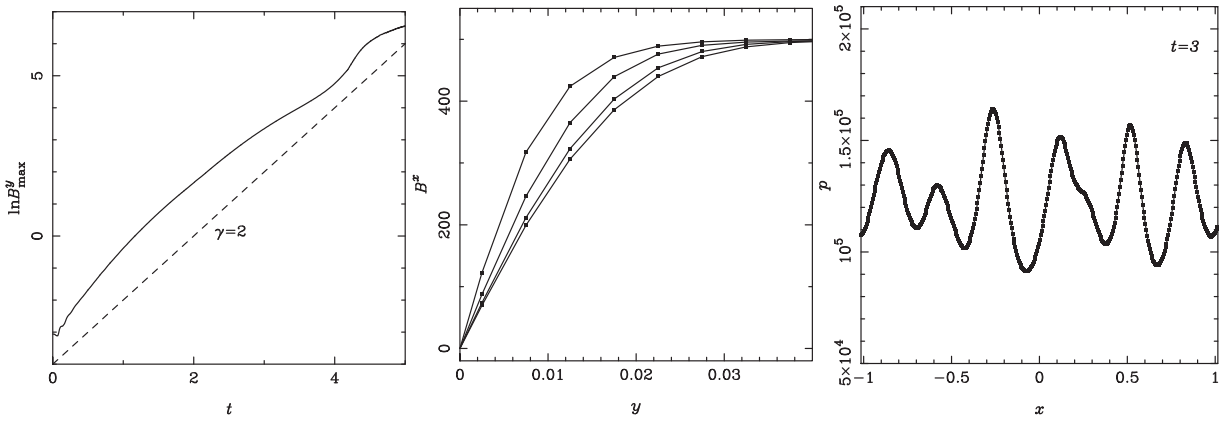

Figure 16. Tearing instability of Harris current sheet. Left panel: maximal value of B^y over the whole domain as a function of time during the linear phase. The dashed line shows the exponential function $\propto e^{2t}$ for comparison. Middle panel: diffusive spreading of the sheet during the linear phase. The lines show B^x along the line $x = 0$ at $t = 0$, 0.5, 1.5 and 2.5 (from the narrowest to the widest of the profiles, respectively). Right panel: gas pressure in the middle of the current sheet ($y = 0$) near the end of the linear phase, at $t = 3$.

and it has the value

$$\omega_{\rm m}\tau_{\rm A}^{*} \approx 0.63\, S^{*-1/2}\,, \tag{103}$$

where

$$S^{*} = \frac{a c_{\rm A}}{\eta}\,, \tag{104}$$

is the Lundquist number, and

$$\tau_{\rm A}^{*} = a/c_{\rm A}\,, \tag{105}$$

is the Alfvén time-scale of the current sheet based on the sheet thickness (Furth, Killeen & Rosenbluth 1963). Since the number of plasmoids emerging in the simulations (see the right panel of Fig. 16) is $n_p = 6$ the fastest growing mode in the simulations has $\lambda = 0.33$ and $k_{\rm m} = 6\pi$, which is inside the range set by the perturbation (see equation 101). Hence, one may use the above equations to estimate S^* due to the numerical resistivity, assuming domination of the fastest mode. Substituting the measured values of $\omega_{\rm m}$ and a into equation (103) yields $320 < S^* < 480$, where the lower limit corresponds to the data for $0 < t < 1$ and the upper limit for $2 < t < 3$. For $0 < t < 1$, the corresponding resistivity is $\eta \approx 4 \times 10^{-5}$, which is only 2.5 times lower than the initial numerical resistivity estimated via equation (90). The corresponding Lundquist number based on the half-length of the current sheet

$$S = \frac{L c_{\rm A}}{\eta} \approx 3 \times 10^{4}\,.$$

Next, one can use equation (102) to check if the value of S^* based on the growth rate is consistent with the number of emerged plasmoids. Substituting the values of S^* and a into equation (102) yields $0.25 < \lambda_{\rm m} < 0.36$, where again where the lower limit corresponds to the data for $0 < t < 1$ and the upper limit for $< 2t < 3$. Somewhat surprisingly, the observed value $\lambda = 0.33$ fits perfectly this theoretical prediction.

For further comparison with the results of analytical and numerical studies of the tearing instability in the framework of resistive MHD, we also run a model with a single sinusoidal perturbation $B^y = 10^{-4} \sin 6\pi x$. Fig. 17 illustrates the profiles of the key flow parameters across the current sheet along the line $x = 1/12$, where B^y is maximum. These vary very little during the linear phase and have almost the same shape along all other lines $x =$ const. So, one may call them numerical 'eigenmodes'. Qualitatively, they are similar to the eigenmodes found in the resistive RMHD simulations by Del Zanna et al. (2016), though there are some differences too. For example, the central dip in the profile of B^y in not as deep, the increase of $|v^y|$ prior to vanishing at $x = 0$ is not as strong, and the central peak of v_x is surrounded by a broad depression not seen in the resistive data.

Overall, given the fact that the numerical resistivity is more complex than the uniform scalar resistivity used in the theory of tearing instability, the agreement between this theory and the results of our simulations is quite remarkable.

5.4.2 *Non'-linear phase*

Once the multiple plasmoids developed in the current sheet, its subsequent evolution proceeds in the plasmoid-dominated regime. Smaller plasmoids merge to form larger ones, the sections of the current sheet between them lengthen and suffer secondary tearing instability. Secondary plasmoids emerge and merge with the larger plasmoids or other secondary plasmoids (see Fig. 18), trying to establish a hierarchy of scales (Uzdensky, Loureiro & Schekochihin 2010). The plasma of the current sheet gets heated up to very high temperature, typically $\zeta = kT/mc^2 = 10^5$. This is consistent with the magnetic energy per particle $\zeta_B = B^2/8\pi nmc^2 = 1.25 \times 10^5$ in the external plasma. In places, the Lorentz factor of the flow in the current sheet reaches $\gamma = 3$, and the collisions of the fast moving plasma with plasmoids drive shock waves.

Given the efficient heating of plasma in the current sheet, the global reconnection rate can be derived from the rate of increase of the total plasma energy in the computational domain. This energy is dominated by the thermal energy of plasma in the current sheet. The left panel of Fig. 19 shows the total plasma energy $\mathcal{E}_{\rm pl}(t)$ computed via equation

$$\mathcal{E}_{\rm pl} = \sum_{i=1}^{n_x}\sum_{j=1}^{n_y} \mathcal{E}_{\rm pl}^{i,j}\,, \tag{106}$$

where the cell volume factor is ignored. Up to $t = 4$ its increase is associated with the resistive spreading of the current sheet, and thereafter with the magnetic reconnection. The total increase of the plasma energy for $4 \le t \le 10$ is $\Delta\mathcal{E}_{\rm pl} = 0.475 \times 10^{10}$. The total initial electromagnetic energy in the domain $\mathcal{E}_{\rm em} = 0.197 \times 10^{11}$.

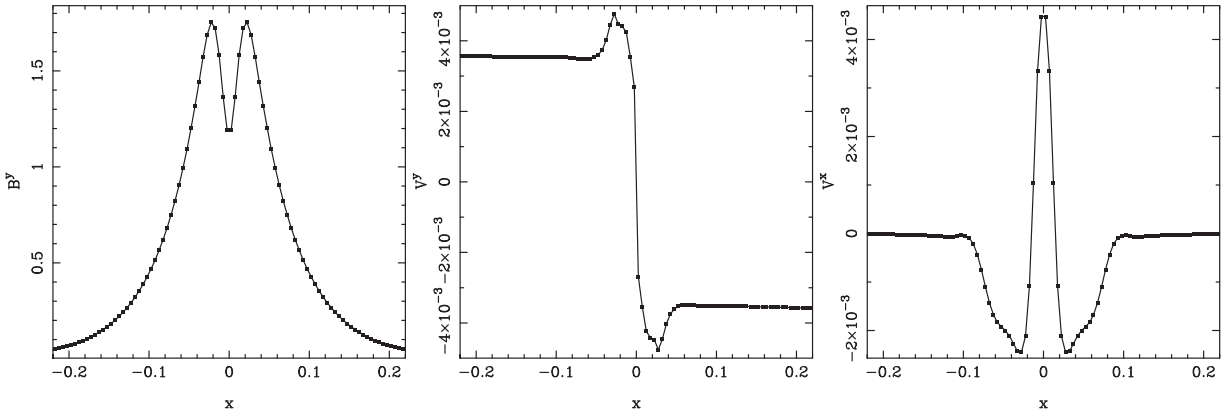

Figure 17. Tearing instability of Harris current sheet. Numerical 'eigenmodes' in the case of single perturbation with $k = 6\pi$.

Ignoring the residual magnetic energy of plasmoids,

$$\Delta\mathcal{E}_{\rm pl} = \frac{\mathcal{E}_{\rm em}}{L}\langle v_r\rangle\Delta t\,, \tag{107}$$

where $\langle v_r\rangle$ is the average speed of the electromagnetic energy inflow. For the above measurements, this equation yields $\langle v_r\rangle = 0.04$.

The middle panel of Fig. 19 shows the solution at $t = 9$ around the x-point near the largest plasmoid of the current sheet at this stage. Based on the velocity field, the x-point is located at $(x, y) \approx (-0.56, 0)$. The right panel of this figure shows $v^y(y)$ along the line $x = -0.56$. One can see that the plasma (and the magnetic field) flows towards the x-point with the speed ≈ 0.05, in agreement with the above estimate of the global reconnection rate. This reconnection rate is only slightly below the 'universal' maximal reconnection rate $R \approx 0.1$ found in resistive MHD, Hall-MHD, and particle-in-cell (PIC) simulations, and in the observations of Earth and Solar magnetospheres (see the references in Liu et al. 2017).

This is another test problem where the DER step had to be switched off in order to avoid conversion failures at shocks. The same applies to the remaining tests described further down.

5.5 ABC grid of magnetic ropes

The double-periodic 2D ABC configuration of magnetic ropes is interesting because it is unstable and involves developing of current sheets at the non-linear phase of the instability via collapse of x-points (e.g. Parker 1983; East et al. 2015; Lyutikov et al. 2017). Its magnetic field is force-free with

$$\begin{cases} B^x = -B_0\sin(ky)\,, \\ B^y = B_0\sin(kx)\,, \\ B^z = B_0(\cos(kx) + \cos(ky))\,. \end{cases} \tag{108}$$

The ropes with $B^z > 0$ are located at $(x_i, y_j) = (2\pi/k)(i, j)$, the ropes with $B^z < 0$ at $(x_i, y_j) = (\pi/k)(1 + 2i, 1 + 2j)$, and the x-points (out-of-plane x-lines) at $(x_i, y_j) = (\pi/k)(2i + 1, 2j)$ and $(x_i, y_j) = (\pi/k)(2i, 2j + 1)$, where $i, j \in Z$.

In the test simulations, $B_0 = 100$, $k = 2/\pi$, and $p = \rho = 1$. The magnetization varies from $\sigma = 0$ at the x-points to $\sigma = 2 \times 10^3$ in the centre of the magnetic ropes (islands). The domain is $(-1, 1) \times (-1, 1)$ with 400 uniformly spaced gridpoints in each direction, and periodic boundary conditions. The initial equilibrium is perturbed by imposing the velocity field

$$\boldsymbol{v}(x, y) = \frac{v_0}{\sqrt{2}}\left(-\cos\frac{k}{2}(x + y), \cos\frac{k}{2}(x + y), 0\right)\,, \tag{109}$$

with $v_0 = 0.01$. Such a perturbation is expected to trigger the shear-type mode of the instability (Lyutikov et al. 2017).

The global dynamics of the ABC grid is illustrated in Fig. 20. Initially, the speed of global motion set by the perturbation (109) increases, reaching the maximum value of $v \approx 0.35$ at about $t = 2.5$. At this point, the ropes of the same polarity (the same sign of B_z) form a linear chain running at the angle of 45° to the x-axis, for the first time. The high value of the speed shows that the initial perturbation may be considered as small. At around $t = 3.5$, there is a turning point, when the ropes start moving in the opposite direction. The subsequent global motion is a decaying oscillation about the state with the 45°-alignment. In the ideal model, this state is a stable equilibrium (Lyutikov et al. 2017).

On approach to the oblique alignment, the x-points collapse into current sheets separating ropes of the same polarity (see the top-middle panel of Fig. 20). These current sheets appear to suffer the tearing instability, and very soon a single plasmoid emerges in the middle of each sheet (the top-right panel of Fig. 20). Fig. 21 zooms into the current sheet located around the point $(x, y) = (-0.5, 0)$. As one can see, the current sheet is not yet developed at $t = 1.0$. At $t = 1.5$, it appears as a vertical linear structure, whose length is approximately 3.5 times shorter than its ultimate length. At $t = 2.0$, its length increases approximately by a factor of 2 and its orientation in space changes, reflecting the relative motion of the flux ropes. At $t = 2.5$, the current sheet is inclined at about 45° to the y-axis, and in the middle of it there is a bulge visible with a naked eye. Thus, the plasmoid had only time $\Delta t \approx 1$ to grow from perturbation.

This current sheet is as thin as the initial current sheet in the tearing instability simulations described in Section 5.4, both in terms of the number of cells, approximately four, and in terms of the linear size, $a \approx 0.013$. Hence, based on the numerical resistivity Lundquist number is also approximately the same, $S^* \approx 300$. The total length of the current sheet is $2L \approx 0.45$, leading to the aspect ratio $a/L \approx 0.045$. The aspect ratio of Sweet–Parker's equilibrium current sheet, $(a/L)_{\rm SP} \simeq S^{-1/2} = 1/S^*$ (Parker 1957; Sweet 1958), corresponding to the same value of S^* is much smaller, $(a/L)_{\rm SP} \approx 0.003$. Taking into account the reduction of the numerical resistivity for current sheets inclined at 45° by the factor of 2 would make this estimate even lower. Therefore one may ignore the flow inside the current sheet and apply the results of Furth et al. (1963) on the growth of the tearing instability (cf. Del Zanna et al. 2016). Equation (102) then gives the wavelength of the fastest growing mode $\lambda_{\rm m} \approx 0.25$, which is consistent with the fact that only one plasmoid emerges in this current sheet.

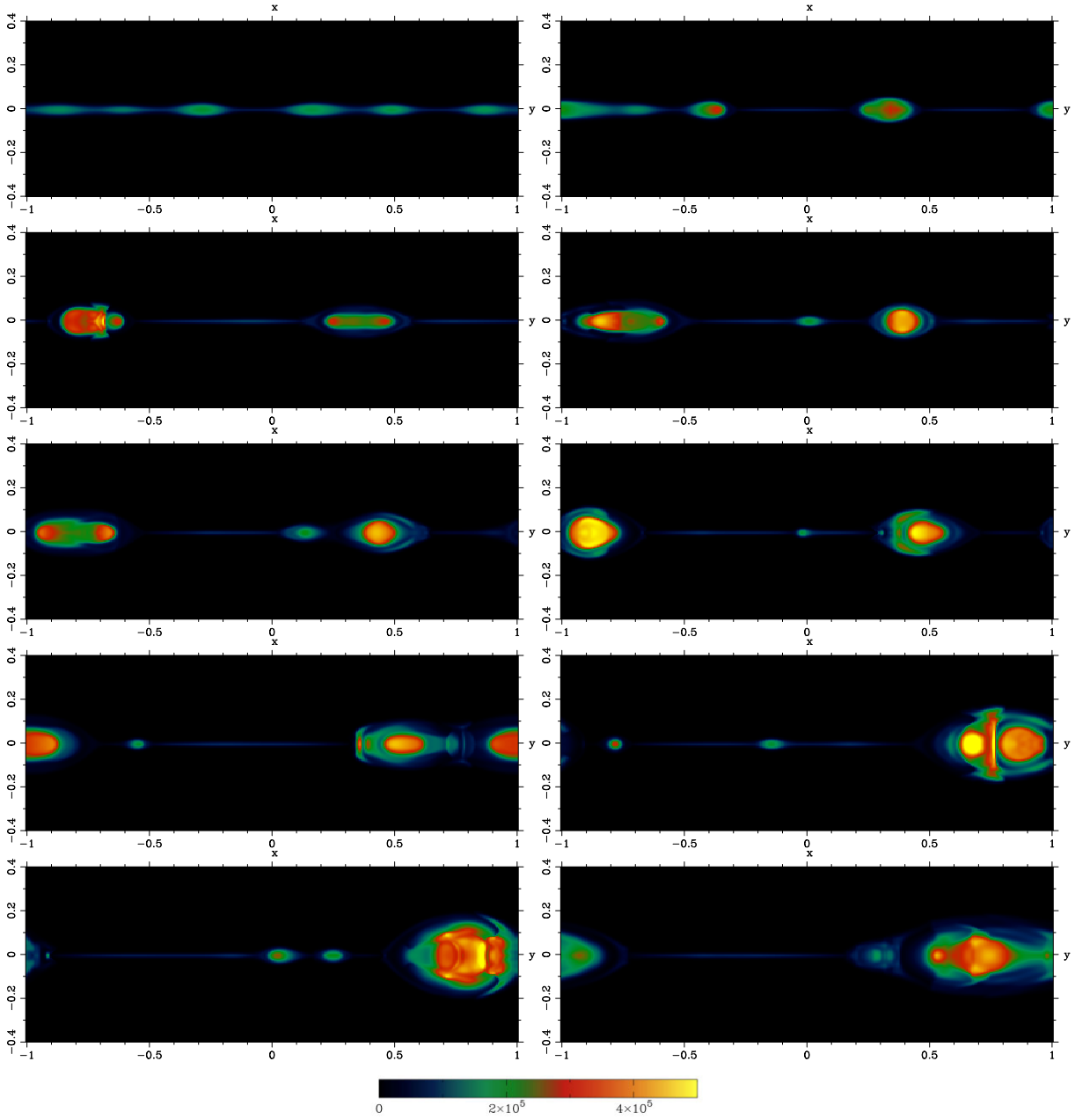

Figure 18. Non-linear phase of the tearing instability. Gas pressure at $t = 4, 4.5, \ldots, 8.5$ (from left to right and from top to bottom).

Pucci & Velli (2014) argued that current sheets are unable to reach the Sweet–Parker equilibrium because they get fragmented by the tearing instability before reaching $(a/L)_{\rm SP}$. They also proposed the current sheets scaling $(a/L)_{\rm PV} = S^{-1/3} = S^{*-1/2}$, where $(a/L)_{\rm PV}$ can be interpreted as the lower limit on the aspect ratio of non-fragmented current sheets. For $S^* = 300$, this yields $(a/L)_{\rm PV} \approx 0.057$, which is similar to the ultimate aspect ratio of the current sheets in our ABC simulations. The Pucci–Velli scaling can be supported with a simple causality argument. The minimum time required to form a current of the half-length L is its Alfvén time $\tau_{\rm A} \simeq L/c_{\rm A}$. The e-folding time $\tau_{\rm m} = 1/\omega_{\rm m}$ of the fastest growing unstable mode cannot be much shorter than $\tau_{\rm A}$, as otherwise the current sheet fragments already during its formation. Hence, for the longest non-fragmented current sheet, $\omega_{\rm m}\tau_{\rm A} \sim 1$. Equation (103) for the growth rate of the fastest mode can be conveniently written as

$$\frac{a}{L} \approx \left(\frac{0.63}{\omega_{\rm m}\tau_{\rm A}}\right)^{2/3} S^{-1/3}, \tag{110}$$

which yields the Pucci–Velli scaling when $\omega_{\rm m}\tau_{\rm A} \sim 1$.

For $S^* = 300$ and $a/L = 0.045$, equation (110) yields $\omega_{\rm m}\tau_{\rm A} \approx 0.81$, consistent with the current sheets just braking the fragmentation threshold. Given the observed $\tau_{\rm A} \approx 0.22$, the estimated value of $\omega_{\rm m}$ yields $\tau_{\rm m} \approx 0.27$. Because the plasmoids emerge on the time-scale $\Delta t \approx 1$, this implies that their amplitude could grow only by the factor $\approx \exp(1/0.27) \approx 40$. This is a small growth compared to what is normally achieved in the numerical studies of instabilities, which start with very small perturbations. However, the current sheets in the ABC simulations are highly dynamic from the start and hence

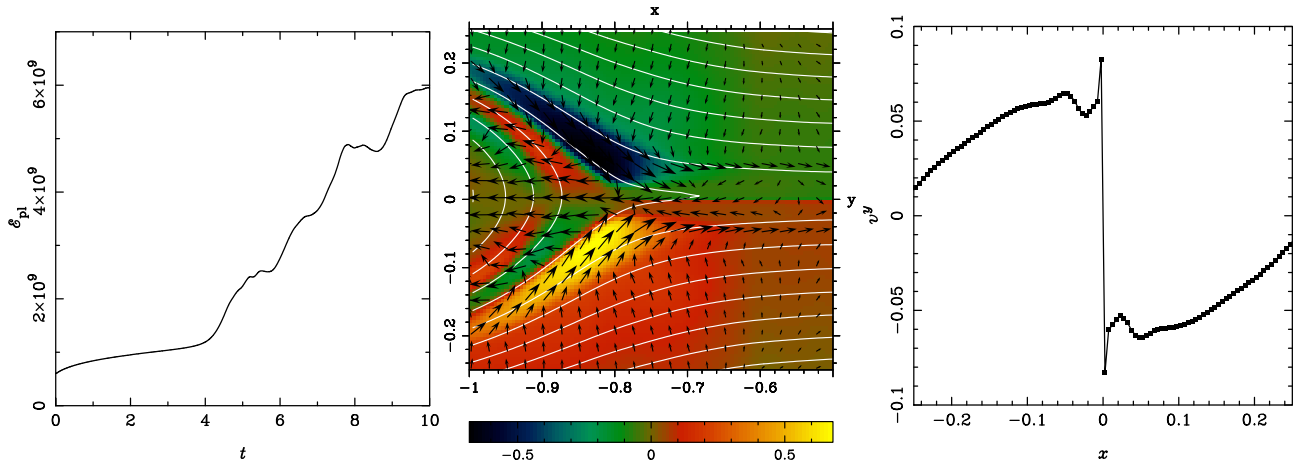

Figure 19. Non-linear phase of the tearing instability. Left panel: total plasma energy in the domain as function of time. Middle panel: the image shows the v^y component of velocity near the large plasmoid at $t = 9$. The contours show the magnetic field lines and the arrows are the velocity vectors. Right panel: the inflow velocity of magnetic field along the line $x = -0.56$, where the velocity field shown in the middle panel indicates an x-point in the current sheet.

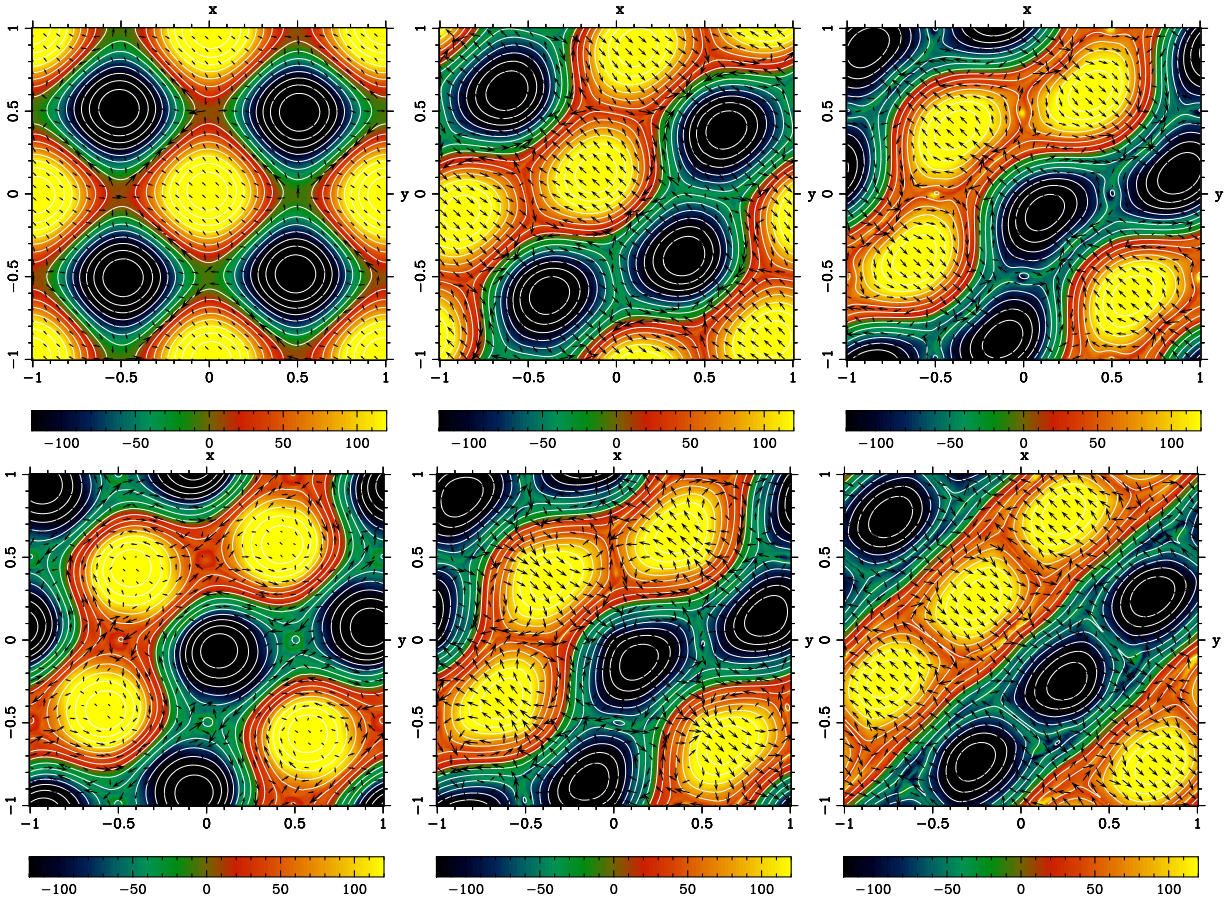

Figure 20. ABC grid. The image shows B^z, the contours show the magnetic field lines, and the arrows show the velocity field $\boldsymbol{v}$. From left to right, t =1.0, 2.0, and 3.0 in the top row, and t =3.5, 4.0, and 4.5 in the bottom row.

not expected to be near to such an almost perfect balance at any point in their evolution.

We also run this problem at the doubled resolution, and found a very similar evolution, especially at the early phase. In particular, the plasmoids emerge on the same time-scale (see the bottom row of Fig. 21). There is still only one plasmoid per current sheet, but the secondary current sheets have approximately the same aspect ratio as the primary current sheet at the lower resolution, suggesting that secondary plasmoids may emerge when the resolution is increased furthermore.

The PIC simulations of this problem (Lyutikov et al. 2017) show a similar dynamics, but with some quantitative differences. In these

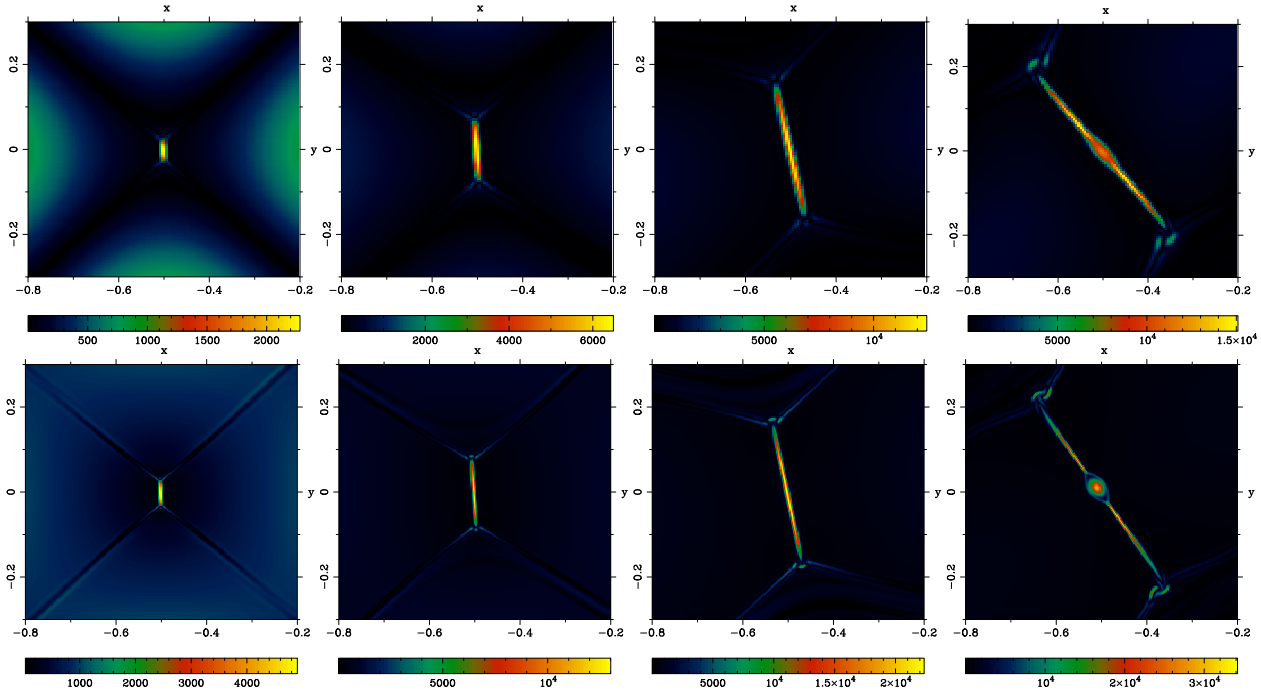

Figure 21. ABC grid. From left to right, the total electric current density for the current sheet emerging near the point $(x, y) = (-0.5, 0)$ at $t = 1.0$, 1.5, 2.0, and 2.5 respectively. The bottom row shows the solution obtained with the doubled resolution.

simulations, the ABC grid has the same linear scales, and the Alvfén speed is also very close to the speed of light. Hence, no time rescaling is required. The initial plateau phase in the PIC simulations continues up to $t = 4$, not $t = 1.5$ like in our simulations. However, this difference is attributable to the amplitude and nature of the initial perturbation of the ABC grid and simply requires us to shift the timing of the PIC simulations back by about $\Delta t = 2.5$ for comparison with our results. With this shift applied, by $t = 10$ the total electromagnetic energy in the PIC simulations is reduced by about 40 per cent, compared to the 18 per cent found here. This implies an approximately twice as fast reconnection rate in the PIC simulations compared to ours. Moreover, by this time the initial periodic structure of the ABC grid is erased, with the ropes of single polarity merged into larger structures (see fig. 8 in Lyutikov et al. 2017), whereas in our simulations the individual ropes are still identifiable. This is also consistent with the higher reconnection rate of the PIC simulations. According to fig. 8 in Lyutikov et al. (2017), the plasmoids are not seen at $t = 1.5$ and 2.5, but fully formed at $t = 3.5$. Thus, they emerge on approximately the same time-scale as in our simulations. This suggests that the timing is dictated by the macroscopic dynamics of the system rather than by the details of the microphysics. The number of plasmoids is also about one per current sheet. (However in other PIC runs, which yields thicker current sheets, the plasmoids do not emerge at all. See the discussion around equation 112.)

5.6 Magnetic field errors in the 2D simulations

In our implementation of the splitting approach we used the GLM method to keep the magnetic field near, but not exactly in, the divergence-free state. The deviation from the divergence-free state originates due to the truncation errors in the numerical integration of the Faraday equation and this allows us to estimate the errors in the magnetic field. This can be used to assess the potential impact of such errors on the conversion failures when the same problems are attempted in the standard mode of our code.

According to the analysis of Section 2.1 (see equations 17 and 20), in order not to cause the conversion failures, the relative error in magnetic field must satisfy the condition

$$\left|\frac{\delta B}{B}\right| \lesssim \frac{\gamma^2}{\sigma}\,.$$

To apply this result, we first estimate the relative error in the magnetic field as

$$\left(\frac{\delta B}{B}\right)_{ij} \simeq \left((B^i_{i+1,j} - B^i_{i-1,j}) + (B^j_{i,j+1} - B^j_{i,j-1})\right)/||\boldsymbol{B}_{i,j}||\,,$$

and then compute the error parameter

$$\mathrm{Er} = \left|\frac{\delta B}{B}\right| \frac{\sigma}{\gamma^2}\,.$$

When $\mathrm{Er} \gtrsim 1$, the error is sufficiently large to result in an unphysical state and hence cause a failure of the variable conversion. When $\mathrm{Er} < 1$, the error is below the safety limit. Since the analysis leading to these expectations is not comprehensive but confined to simple special cases, some caution needs to be exercised here.

Fig. 22 shows the error parameter for the magnetic rope, cylindrical explosion, and tearing instability tests. At the start of the magnetic rope test, Er reaches the values significantly exceeding unity near the rope surface (see the top-left panel of Fig. 22). Based on these values, we anticipated the simulations run in the standard mode of the code to crash at the very start, and they did even for the Courant number as small as $\mathrm{C} = 0.01$. By $t = 5$, the maximum value of Er reduces to ≈ 0.36, suggesting that it may be possible to continue the simulations from this point in the standard mode. This was indeed the case, but only with the Courant number reduced down to $C = 0.4$.

The bottom-left panel of Fig. 22 shows Er for the explosion test with $B_0 = 1$ at $t = 4$. Even at this time it remains about unity at the

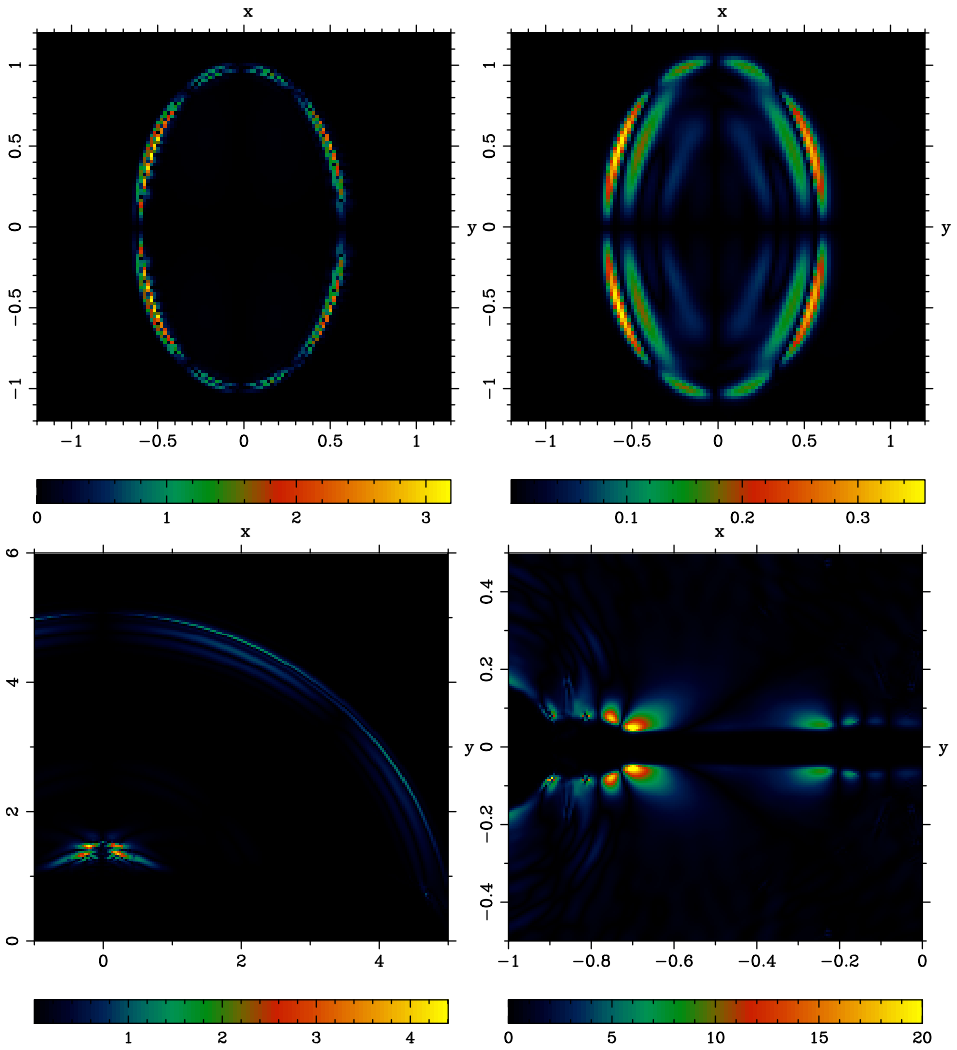

Figure 22. The error parameter Er. Top-left panel: the magnetic rope test with $B_0 = 100$ at $t = 0.02$. Top-right panel: the magnetic rope test with $B_0 = 100$ at $t = 5$. Bottom-left panel: the cylindrical explosion test with $B_0 = 1$ at $t = 4$. The high residuals colocate with the transient shock waves associated with the oscillations in the direction normal to the magnetic field. Bottom-right panel: the tearing instability test with $B_0 = 500$ at $t = 7.5$.

external fast shock, and reaches Er ≈ 4 in the vicinity of the point $(x, y) = (0, 1.3)$, where reverberation of the magnetic field appears to have triggered a secondary shock wave. As already stated in Section 5.3, our attempt to run this test in the standard mode of the code has failed. For the test with $B_0 = 0.1$, the error parameter is much lower, Er $\lesssim 0.3$, reaching the maximum at the external shock. These low values are consistent with the fact that for this value of B_0 the test can be run with the standard code from the start to the finish.

In the tearing instability test, Er is small at the linear phase, but then strongly increases in the non-linear phase. As one can see in the bottom-right panel of Fig. 22, the error parameter can reach the values Er ≈ 20 in the vicinity of the current sheet. Although $\delta B/B$ itself is higher inside the current sheet, where the magnetic field is highly distorted, leading to a stronger departure from the divergence-free state, the magnetization σ is significantly lower there, due to the presence of very hot plasma. In the outskirts of the current sheet, σ is very high and the magnetic field is still strongly distorted by the plasmoids. Our attempts to continue the simulations from this point in the standard mode have failed.

Overall, the data support the conclusion that the errors in magnetic field are responsible for failures of standard schemes in the high-σ regime. In principle, an increase of the accuracy in the numerical integration of the Faraday equation may help to extend the applicability of standard schemes. In this regard, schemes utilizing the CT approach may be more robust as they eliminate the errors associated with the $\nabla \cdot B = 0$ constraint. Other errors, however, will remain and may still be too high. Increasing the order of scheme's accuracy could help too. This is expected to be very effective in regions with smooth magnetic field, but not at discontinuities.

6 SUMMARY AND DISCUSSION

The main goal of this study was to find a new approach to numerical RMHD in the high-magnetization regime, where the standard conservative schemes turned out to be highly unreliable. Its direction was motivated by the understanding that the most attractive feature of such schemes, the conservation of total energy-momentum, is also the main reason for their failures in the high-σ regime. For such a high magnetization, the energy-momentum tensor is dominated by the electromagnetic field, and even relatively small errors emerging in the numerical integration of the Faraday equation can render the set of conserved variables unphysical. This understanding invited us

to search for a way of breaking the strict link between the energy-momentums of plasma and electromagnetic field imposed by the total energy-momentum conservation and enforced in the standard conservative schemes. Moreover, in this regime the electromagnetic field is largely force-free, and its evolution is well approximated by the equations of FFDE, which can be considered as a singular limit of RMHD when $\sigma \to \infty$. This invited us to study the potential of the perturbation approach, where the electromagnetic field is evolved mostly as force-free, and the plasma introduces only a small perturbation to the FFDE solution, with σ^{-1} playing the role of a small parameter. However, the standard asymptotic expansion approach is complicated, with higher order terms needed for accuracy in the case of moderate σ. Moreover, it is not suitable for $\sigma \leq 1$, significantly limiting the area of application.

Instead, we opted for a generalization of the approach proposed by Tanaka (1994), where the perturbation is governed the RMHD equations with the energy-momentum tensor modified via explicit subtraction of the energy-momentum tensor of the force-free field. In contrast to Tanaka (1994), where the strong force-free background field is stationary, in our approach it is dynamic. So, we enlarge the system of differential equations, which is now composed of two linked subsystems: the FFDE system for the electromagnetic field, and the perturbation system for the plasma. The latter has the same number of equations as the original RMHD. These subsystems are linked via the interaction terms in the perturbation system and the perfect conductivity condition. This approach delivers a numerical scheme which can be applied in both the high- and low-σ regimes.

The equations of the enlarged system are integrated simultaneously, and at the end of each time-step the electromagnetic field of the FFDE system and its perturbation are recombined. Thus, the final result is a splitting scheme, which is similar in spirit to operator-splitting schemes, but different in form. Like in the operator-splitting method, we separate processes of different nature and do this to bypass the stiffness of differential equations. However, if the operator-splitting method is focused on the stiffness arising due to the very different time-scales associated with the involved differential operators (processes), our splitting scheme deals with the stiffness arising due to the significant difference in the magnitude of contributions to the conserved quantities from components of different nature. If the operator-splitting method involves successive integration of simplified versions of differential equations, where some of the operators are dropped, we solve the whole system of equations simultaneously. This simplifies development of higher order schemes.

Both the subsystems of split RMHD can be written as conservation laws, and hence can be numerically integrated using the standard methods developed for such laws. We adopted the third-order WENO approach similar to that of Del Zanna et al. (2007), with some modifications. In particular, (1) we developed a new third-order WENO interpolation, which allows rapid transition to the third-order scaling of computational errors at low resolution and does not result in a loss of accuracy at turning points; (2) the code required a new variable conversion algorithm; (3) we used the GLM method (Dedner et al. 2002) to keep the magnetic field nearly divergence free; and (4) we developed a simple algorithm to locate strong shocks in order to switch off the DER step of Del Zanna et al. (2007) at their locations. The latter is needed to suppress the spurious oscillations capable of causing conversion failures at high-σ shocks.

Only the momentum density is used for the variable conversion of the FFDE subsystem. As a result, the energy of the FFDE subsystem and hence the total energy are not conserved. This break of conservation is at the centre of our splitting method. One can compute the difference between the energy density of the FFDE subsystem based on the energy conservation law and the one based on the updated $\boldsymbol{E}_{(0)}$ and $\boldsymbol{B}_{(0)}$, and transfer it to the perturbation subsystem, thus enforcing the total energy conservation. Such energy exchange between plasma and electromagnetic field implicitly occurs in standard conservative schemes, where it facilitates plasma heating in current sheets. However, it is also responsible for their failures in the high-σ regime. Hence in the splitting approach, the energy transfer must be conditional, filtering out the cases where this may lead to a crash. A simple analysis shows that the energy transfer is safe when the transferred energy is positive. In this case, the energy transfer amounts to plasma heating via the numerical dissipation of the electromagnetic energy. When the positivity is the only condition, plasma is also heated by weak waves generated in active regions. By setting positive lower limits on the transferred energy, this low-level heating can be suppressed. In the splitting approach, there is another, now uncontrollable mechanism of plasma heating, which involves the interaction terms of the perturbation equations. This mechanism accounts for about 50 per cent of heating in current sheets.

The 1D and 2D test simulations of continuous hyperbolic and associated shock waves have shown that the splitting method remains robust and accurate when applied to problems with very high σ. This is particularly true for continuous waves. Shock waves are more problematic, and in some cases the code can fail to deliver accurate values for the plasma parameters. Our test results suggest that this occurs when the tangential component of magnetic field experiences large jumps across the shock, leading to excessive plasma heating via the uncontrollable numerical dissipation of electromagnetic energy. As a result, the shock fails to develop monotonic structure. Although such shocks do exist, they are unlikely to be common. For example, in the 2D simulations of explosions in strong uniform magnetic field, the variation of the tangential magnetic field is much smaller.

The splitting approach delivers accurate solutions not only for high-σ problems, but also for problems with low magnetization, as illustrated by the shock tests FS7 and FS9, where the magnetization of the upstream state is only $\sigma = 10^{-3}$, and by the blast wave simulations with $\sigma_0 \sim 10^{-5}$. Moreover, as the magnetization decreases, the shock solutions become progressively more accurate. In fact, for unmagnetized plasma, the splitting scheme reduces to the standard conservative scheme for relativistic HD. For subrelativistic problems, the splitting approach also performs very well, as demonstrated by the FS9 test where the sound speed $c_s \approx 0.01$ and the Alfvén speed $c_{\rm A} \approx 0.007$. Thus, the splitting approach can be applied to many complex astrophysical problem involving states with vastly different parameters, like active galactic nuclei, where the low-σ accretion disc coexists with the high-σ magnetosphere of the central black hole.

Our test simulations of problems involving current sheets have demonstrated that the splitting approach can capture the active phenomena of plasma astrophysics involving fast magnetic reconnection. The fast reconnection plays an important part in many astrophysical phenomena, resulting in explosive dynamics, plasma heating, and acceleration of non-thermal particles responsible for high-energy emission. The latter is particularly important for high-σ relativistic plasmas, where PIC simulations of collisionless shocks revealed their low efficiency in particle acceleration (Sironi & Spitkovsky 2009, 2011). The reconnection events are preceded by the formation of current sheets, which can emerge spontaneously in quasi-static configurations, or forced by plasma motion in highly dynamic conditions (e.g. Pontin & Priest 2022).

The detailed structure and evolution of current sheets depends on the microphysics responsible for the deviation from the magnetic flux

freezing approximation of ideal MHD. Interestingly, most numerical methods for ideal MHD also break the flux freezing because of the truncation errors of numerical algorithms. This phenomena is called the numerical resistivity. Although magnetic reconnection has been seen in ideal MHD simulations (see e.g. Laitinen et al. 2005; Ripperda et al. 2022; Fryer et al. 2023; Berta et al. 2024, for more recent examples), this has been treated with a great deal of scepticism. However, in the plasmoid-dominated regime the overall dynamics of current sheets and the reconnection rate do not seem to be that sensitive to the incorporated microphysics (e.g. Liu et al. 2017; Pontin & Priest 2022). This is even more so in the theory of turbulent reconnection, where the reconnection rate does not depend on the microphysics altogether (Lazarian & Vishniac 1999; Lazarian et al. 2020). This motivated us to include problems involving current sheets in the suite of test simulations.

We started by studying the properties of numerical resistivity in our scheme, using as a guide the ansatz of Rembiasz et al. (2017). The 1D simulations of degenerate Alfvén waves (Section 4.3) are in agreement with the simple prescription for the numerical resistivity (90) based on the value of the rounding error. They confirm the dependence of numerical resistivity on the scheme's order of accuracy, numerical resolution, and the characteristic length-scale of the magnetic field variation $\mathcal{L}$. Since equation (90) states $\eta_{\rm num} \propto \mathcal{L}^{-2}$, the numerical resistivity is similar to the so-called anomalous resistivity, with $\eta \propto j^2$, used in resistive MHD simulations to achieve fast magnetic reconnection (e.g. Yokoyama & Shibata 1994; Syntelis, Priest & Chitta 2019; Færder, Nóbrega-Siverio & Carlsson 2023). In our 2D simulations, the corresponding magnetic Reynolds number varies from $Re_{\rm m} \sim 10^2$ for current sheets which are only few cells wide, to $Re_{\rm m} \sim 10^8$ on the domain scale. Thus, the numerical resistivity has little effect on the large-scale dynamics but very important in 'paper-thin' current sheets. As expected, the numerical resistivity is anisotropic. Our initial investigation of this issue suggests that it is highest when magnetic field is aligned with the gridlines and reduces by the factor of 2 when the magnetic field is at the angle of 45° to the gridlines.

In Section 5.4, we described the simulations of the tearing instability for the case of a very long and thin, only few grid cells across, Harris current sheet aligned with the computational grid. Quite remarkably, the results of these simulations are in good agreement with the key conclusions of the basic theory of this instability developed within the framework of Newtonian resistive MHD with constant scalar resistivity (Furth et al. 1963) [Although the theory of the tearing instability was developed in the Newtonian framework, the relativistic results are basically identical (Komissarov, Barkov & Lyutikov 2007a; Del Zanna et al. 2016).]. In particular, the wavelength of the fastest growing mode and its growth rate agree with the theoretical values obtained with the numerical resistivity (in place of the actual η) assuming $\mathcal{L} \approx a$, where a is its half-width of the current sheet. This result is somewhat surprising, as the theory predicts the existence of a narrow resistive (tearing) sublayer (boundary layer) in the middle of the current sheet. The thickness of this sublayer is

$$a_{\rm sub} \approx 1.5\, S^{*-1/4} \tag{111}$$

(Furth et al. 1963). For the consistent with the simulations value $S^* \approx 400$, the corresponding $a_{\rm sub} \approx 0.3a = 3 \times 10^{-3}$, whereas the cell size $\Delta y = 5 \times 10^{-3}$, and hence the sublayer is not resolved. In fact, it is collapsed into a discontinuity (see the right panel of Fig. 19). On the other hand, it has been claimed that many properties of reconnection are largely determined by the ideal MHD dynamics outside of the sublayer and only weakly depend on its microphysics (Liu et al. 2017; Pontin & Priest 2022). This is especially clear in the case of forced reconnection, where the reconnection rate is set by the externally determined rate of plasma inflow into the current sheet. At the non-linear phase of our ideal MHD simulations, the dynamics of the current sheet is also very similar to what in seen in resistive MHD and PIC simulations, including the development of primary plasmoids, their merger, the emergence of secondary plasmoids in secondary current sheets etc. (e.g. Bhattacharjee et al. 2009; Del Zanna et al. 2016; Petropoulou & Sironi 2018). The estimated global reconnection rate is about 0.04.

The simulations of the unstable ABC grid of magnetic ropes (Section 5.5) allowed us to study the case where the current sheets are not present in the initial solution, but develop as a result of the x-point collapse. These current sheets produced solitary plasmoids on the time-scale which is only few times longer than their ultimate Alfvén time-scale. These results are in agreement with the conclusion reached by Pucci & Velli (2014) that current sheets become fragmented by the tearing instability well before they reach the Sweet–Parker equilibrium, thus making studies of Sweet–Parker current sheets a matter of purely academic interest.

It is quite interesting that the PIC simulations of the ABC problem for electron–positron plasma (Lyutikov et al. 2017) yield very similar results in terms of the time-scale of the current sheet fragmentation, the number of emerging plasmoids, and the reconnection rate. As noted in Lyutikov et al. (2017), the half-thickness of the collisional current sheets emerging in the PIC simulations is set by the Larmor radius of the plasma particles heated in the sheet, $a \sim r_{\rm L,h}$. For relativistic plasma, this is approximately

$$r_{\rm L,h} = \sigma_0 \gamma_{\rm t,0} r_{\rm L,0}\,, \tag{112}$$

where $\sigma_0 = B_0^2/4\pi w_0$ is the magnetization of the inflowing plasma, $\gamma_{\rm t,0}$ is the thermal Lorentz factor of its particles, and $r_{\rm L,0} = m_{\rm e}c^2/eB_0$. They have also found that the emergence of plasmoids depends on the parameter $r_{\rm L,h}/D$, where D is the wavelength of the ABC grid. Namely, they begin to emerge when $D/r_{\rm L,h} > 126$. Since the half-length of the current sheets $L \approx D/3$, this can be written as

$$\frac{r_{\rm L,h}}{L} < 0.02\,.$$

Thus, even the fragmentation threshold is similar to what is found in our ideal RMHD simulations.

The results of our study of current sheets suggest that in principle the fast reconnection events can be captured in simulations even with ideal RMHD and MHD codes. Although the development of plasmoids and explosive reconnection has already been reported in the ideal RMHD simulations of neutron-star magnetospheres (Bucciantini et al. 2006) and black hole accretion (Ripperda et al. 2022), our study seems to be the first one where the plasmoid-dominated regime of magnetic reconnection is studied more or less systematically (a more advanced study is under way), and an agreement with the resistive MHD theory is found. This warrants a closer look at the numerical resistivity and its properties in different numerical schemes. It is quite possible that its properties are close to those of the proper resistivity only in some schemes and drastically different in others. For example, Rembiasz et al. (2017) found negative resistivity for their scheme. It is possible that the peculiarities of the splitting approach play a role too. Especially the fact that in the ideal FFDE approximation current sheets collapse into discontinuities, with the corresponding reconnection rate approaching the speed of light.

Our results show that for the thinnest current sheets allowed by the code, only few cells wide, the current sheets should be at least ∼100 cells long for the tearing instability to trigger fast reconnection on the Alfvén time-scale. Very long current sheet are know to exist in stellar magnetospheres, including the high-σ magnetospheres of black holes

and neutron stars. However in other astrophysical problems, current sheets may be much smaller compared to the dynamical scales of interest. For example, the size of reconnection sites responsible for the gamma-ray flares in the Crab nebula is only about one light day, whereas the size of the nebula is about 10 light years. For such problems, code's ability to efficiently resolve small thin structures becomes paramount.

Somewhat paradoxically, the ideal MHD codes might end up being more suitable than the resistive codes for large-scale problems of astrophysical interest (cf. Del Zanna et al. 2024, for the simulations of MHD turbulence). First, the actual resistivity of resistive codes has to be much higher than the numerical one to make its introduction meaningful. This would make current sheets significantly thicker and hence they would have to be much longer to allow fast reconnection. Second, uniform scalar resistivity will have strong effect on the magnetic field, and hence the plasma dynamics, outside current sheets, leading to much lower magnetic Reynolds numbers on the large scales compared to what it would be with an ideal code (Mattia et al. 2023, 2024). In principle, this can be mitigated with anomalous resistivity, which depends of the strength of the electric current. Finally, the resistive codes are great for verifying the analytical results of resistive MHD and exploring their non-linear regime, but since the astrophysical plasma is mostly collisionless, the actual benefits of the resistive model in astrophysics are not that obvious.

For RMHD, the fact that the numerical resistivity is not Lorentz-invariant is likely to be an issue for the simulations involving fast relativistic flows. As can be seen in equation (86), for such flows the resistivity reduces like γ^{-1}, whereas the numerical resistivity does not. One relevant example of such flows is the striped pulsar wind, where the time-dilation effect may prevent the reconnection of stripes till the wind passes through its termination shock (Lyubarsky & Kirk 2001). However, direct numerical simulations of such wind in the pulsar frame are extremely challenging and require significant simplification anyway.

Over the last decade, the kinetic approach based on the PIC method was successfully applied to numerical simulations of pulsar and black hole magnetospheres (e.g. Philippov & Spitkovsky 2014; Parfrey, Philippov & Cerutti 2019; Crinquand et al. 2020; Soudais, Cerutti & Contopoulos 2024). This approach has no difficulty in dealing with highly magnetized plasma but suffers from the scale-separation issue. PIC simulations must resolve the microphysics scales, which severely limits the accessible macroscopic scale and makes the method computationally expensive. Although the most recent studies show that the macroscopic size of some astrophysical problems can be scaled down towards the microscopic scales, without the large-scale dynamics being 'contaminated' by the microphysics, in general the issue is here to stay. One approach to mitigating this issue is the use of hybrid schemes, where PIC computations are limited in extent and carried out only where they are unavoidable, for example to compute the non-thermal radiation (e.g. Soudais et al. 2024). Another option is not to use PIC simulations directly altogether, but to incorporate the PIC predictions on particle acceleration and non-thermal emission at the subgrid level of fluid simulations. This requires accurate treatment of plasma in the high-σ regime, including the value of σ itself, and this is where the splitting approach to numerical RMHD promises to be most useful.

7 CONCLUSIONS

In this work, we developed a novel numerical method for integrating RMHD equations, which allows to extend the applicability domain into the regime of extremely high magnetization (high-σ) typical to the magnetospheres of neutron stars and black holes, and expected in the magnetized relativistic outflows from them as well. The method is based on splitting the RMHD equations into interacting (linked) subsystems, one governing the electromagnetic field, and another governing the motion of plasma. The splitting breaks the stiffness of RMHD equations in the high-σ regime, where the total energy-momentum tensor is largely dominated by the electromagnetic field. The method sacrifices the total energy-momentum conservation of standard conservative schemes for RMHD, and this does not allow the small numerical errors in magnetic field to result in catastrophic errors for the plasma parameters. Both the subsystems have the form of conservation laws, which allows to combine the splitting method with various numerical methods developed for such laws. In the current code, we applied the third-order accurate WENO approach.

The suitability of the splitting method to high-σ problems has been confirmed by a variety of 1D and 2D test simulations presented in this paper. Moreover, the code remains accurate for low-σ problems, including the unmagnetized regime ($\sigma = 0$), and the subrelativistic problems. Thus, the splitting method can be used for numerical simulations of complex astrophysical phenomena, which involve components with vastly different physical parameters, with no need for development of hybrid codes.

Given the importance of fast magnetic reconnection in high-energy astrophysics, particular attention has been paid to determining the numerical resistivity of the code and to test problems involving long and thin current sheets. Studying the numerical decay of periodic degenerate Alfvén waves, we verified and calibrated a simple model of numerical resistivity, and found it to be similar to the anomalous resistivity. In the 2D simulations of the tearing instability in a long Harris current sheet, we found the results to be in good agreement with the basic theory by Furth et al. (1963) when the resistivity proper is replaced with the numerical resistivity. At the non-linear phase, the simulations exhibited the typical properties of the fast magnetic reconnection in the plasmoid-dominated regime. The 2D simulations of the ABC grid of magnetic ropes allowed us to study the dynamics of current sheets emerging via x-point collapse. These current sheets became fragmented by tearing instability on Alfvénic time-scale before they could reach the aspect ratio of the Sweet–Parker sheets, in agreement with the analytical results by Pucci & Velli (2014). These results suggest that ideal RMHD codes, at least those based on the splitting method, may be applicable to problems involving fast magnetic reconnection.

ACKNOWLEDGEMENTS

We thanks the anonymous referee for their extensive and constructive report which led to noticeable improvements on the original manuscript. DP acknowledges support from Science and Technology Facilities Council (STFC) in the form of research studentship.

DATA AVAILABILITY

The data underlying this article will be shared on reasonable request to the corresponding author.

REFERENCES

Balsara D. S., Spicer D. S., 1999, J. Comput. Phys., 149, 270
Berta V., Mignone A., Bugli M., Mattia G., 2024, J. Comput. Phys., 499, 112701
Bhattacharjee A., Huang Y.-M., Yang H., Rogers B., 2009, Phys. Plasmas, 16, 112102

Blinn J., 2006, IEEE Comput. Grap. Appl., 26, 90
Brackbill J. U., Barnes D. C., 1980, J. Comput. Phys., 35, 426
Brent R., 1971, Comput. J., 14, 422
Bucciantini N., Thompson T. A., Arons J., Quataert E., Del Zanna L., 2006, MNRAS, 368, 1717
Crinquand B., Cerutti B., Philippov A., Parfrey K., Dubus G., 2020, Phys. Rev. Lett., 124, 145101
Dedner A., Kemm F., Kröner D., Munz C.-D., Schnitzer T., Wesenberg M., 2002, J. Chem. Phys., 175, 645
Dekker T., 1969, in Dejon B., Henrici P., eds, Constructive Aspects of the Fundamental Theorem of Algebra. Wiley-Interscience, New York, p. 37
Del Zanna L., Zanotti O., Bucciantini N., Londrillo P., 2007, A&A, 473, 11
Del Zanna L., Papini E., Landi S., Bugli M., Bucciantini N., 2016, MNRAS, 460, 3753
Del Zanna L., Landi S., Serafini L., Bugli M., Papini E., 2024, Fluids, 9, 16
De Hoffmann F., Teller E., 1950, Phys. Rev., 80, 692
East W. E., Zrake J., Yuan Y., Blandford R. D., 2015, Phys. Rev. Lett., 115, 095002
Eggington J. W. B.et al., 2020, J. Geophys. Res. (Space Phys.), 125, e27510
Evans C. R., Hawley J. F., 1988, ApJ, 332, 659
Event Horizon Telescope Collaboration, 2021, ApJ, 910, L13
Falle S. A. E. G., 1991, MNRAS, 250, 581
Fryer L. J., et al., 2023, J. Geophys. Res. (Space Physics), 128, e2023JA031317
Furth H. P., Killeen J., Rosenbluth M. N., 1963, Phys. Fluids, 6, 459
Færder Ø. H., Nóbrega-Siverio D., Carlsson M., 2023, A&A, 675, A97
Gammie C. F., McKinney J. C., Tóth G., 2003, ApJ, 589, 444
Gruzinov A., 1999, preprint (astro-ph/9902288)
Ha Y., Kim C.-H., Yang H., Yoon J., 2020, J. Sci. Comput., 82, 63
Harten A., Lax P., van Leer B., 1983, SIAM Rev., 25, 35
Henrick A. K., Aslam T. D., Powers J. M., 2005, J. Comput. Phys., 207, 542
Jiang G.-S., Shu C.-W., 1996, J. Comput. Phys., 126, 202
Komissarov S. S., 1997, Phys. Lett. A, 232, 435
Komissarov S. S., 1999, MNRAS, 303, 343
Komissarov S. S., 2001, MNRAS, 326, L41
Komissarov S. S., 2002, MNRAS, 336, 759
Komissarov S. S., 2004, MNRAS, 350, 427
Komissarov S. S., 2006a, in Hughes P. A., Bregman J. N., eds, AIP Conf. Ser., Vol. 856, Relativistic Jets: The Common Physics of AGN, Microquasars, and Gamma-Ray Bursts. American Institute of Physics, p. 129
Komissarov S. S., 2006b, MNRAS, 367, 19
Komissarov S. S., 2007, MNRAS, 382, 995
Komissarov S. S., Barkov M., Lyutikov M., 2007a, MNRAS, 374, 415
Komissarov S. S., Barkov M. V., Vlahakis N., Königl A., 2007b, MNRAS, 380, 51
Laitinen T. V., Pulkkinen T. I., Palmroth M., Janhunen P., Koskinen H. E. J., 2005, Ann. Geophys., 23, 3753
Lazarian A., Vishniac E. T., 1999, ApJ, 517, 700
Lazarian A., Eyink G. L., Jafari A., Kowal G., Li H., Xu S., Vishniac E., 2020, Phys. Plasmas, 27, 012305
Leismann T., Antón L., Aloy M. A., Müller E., Marti J. M., Miralles J. A., Ibáñez J. M., 2005, A&A, 436, 503
Liu X.-D., Osher S., Chan T., 1994, J. Chem. Phys., 115, 200
Liu Y.-H., Hesse M., Guo F., Daughton W., Li H., Cassak P. A., Shay M. A., 2017, Phys. Rev. Lett., 118, 085101
Lundquist S., 1950, Ark. Fys., 2, 361
Lyubarsky Y., Kirk J. G., 2001, ApJ, 547, 437
Lyutikov M., Sironi L., Komissarov S. S., Porth O., 2017, J. Plasma Phys., 83, 635830602
MacDonald D., Thorne K. S., 1982, MNRAS, 198, 345
Mahlmann J. F.et al., 2021, A&A, 647, A57
Majorana A., Anile A. M., 1987, Phys. Fluids, 30, 3045
Martí J.-M., 2015, Comput. Phys. Commun., 191, 100
Mattia G., Del Zanna L., Bugli M., Pavan A., Ciolfi R., Bodo G., Mignone A., 2023, A&A, 679, A49
Mattia G., Del Zanna L., Pavan A., Ciolfi R., 2024, A&A, 691, A105
McKinney J. C., 2006, MNRAS, 367, 1797
Mignone A., Bodo G., 2006, MNRAS, 368, 1040
Mignone A., Del Zanna L., 2021, J. Comput. Phys., 424, 109748
Mignone A., Tzeferacos P., Bodo G., 2010, J. Comput. Phys., 229, 5896
Munz C.-D., Omnes P., Schneider R., Sonnendrücker E., Voß U., 2000, J. Chem. Phys., 161, 484
Noble S. C., Krolik J. H., Hawley J. F., 2009, ApJ, 692, 411
Parfrey K., Philippov A., Cerutti B., 2019, Phys. Rev. Lett., 122, 035101
Parker E. N., 1957, J. Geophys. Res., 62, 509
Parker E. N., 1983, ApJ, 264, 635
Petropoulou M., Sironi L., 2018, MNRAS, 481, 5687
Philippov A. A., Spitkovsky A., 2014, ApJ, 785, L33
Pontin D. I., Priest E. R., 2022, Living Rev. Sol. Phys., 19, 1
Press H., Teukolsky S., Vetterling W., Flannery B., 1992, Numerical Recipies in C. The Art of Scientific Computing. Cambridge University Press, Cambridge
Pucci F., Velli M., 2014, ApJ, 780, L19
Rembiasz T., Obergaulinger M., Cerdá-Durán P., Aloy M.-Á., Müller E., 2017, ApJS, 230, 18
Ripperda B., Liska M., Chatterjee K., Musoke G., Philippov A. A., Markoff S. B., Tchekhovskoy A., Younsi A., 2022, ApJ, 924, L32
Shu C.-W., 2020, Acta Numer., 29, 701–762
Shu C.-W., Osher S., 1988, J. Chem. Phys., 77, 439
Sironi L., Spitkovsky A., 2009, ApJ, 698, 1523
Sironi L., Spitkovsky A., 2011, ApJ, 726, 75
Soudais A., Cerutti B., Contopoulos I., 2024, A&A, 690, A170
Sweet P. A., 1958, in Lehnert B., ed., IAU Symp. Vol. 6, Electromagnetic Phenomena in Cosmical Physics. Cambridge University Press, Cambridge, p. 123
Syntelis P., Priest E. R., Chitta L. P., 2019, ApJ, 872, 32
Tanaka T., 1994, J. Comput. Phys., 111, 381
Uchida T., 1997, Phys. Rev. E, 56, 2181
Uzdensky D. A., Loureiro N. F., Schekochihin A. A., 2010, Phys. Rev. Lett., 105, 235002
Yokoyama T., Shibata K., 1994, ApJ, 436, L197

APPENDIX A: THIRD-ORDER WENO INTERPOLATION

Below, only the interpolation in the x-direction is considered, and all other spatial indices are dropped for brevity. In the other directions, the procedure is the same.

A1 Modified second-order TVD weights

Consider a three-point stencil $S = \{x_{i-1}, x_i, x_{i+1}\}$ and its two substencils $S_- = \{x_{i-1}, x_i\}$ and $S_+ = \{x_i, x_{i+1}\}$. Each of the substencils yields a linear polynomial for interpolation to the ith cell interfaces $x_{i+1/2} = x_i + \Delta x/2$ and $x_{i-1/2} = x_i - \Delta x/2$ on a uniform grid,

$$P_-(x) = u_i + \frac{(u_i - u_{i-1})}{\Delta x}(x - x_i)\,, \tag{A1}$$

and

$$P_+(x) = u_i + \frac{(u_{i+1} - u_i)}{\Delta x}(x - x_i)\,. \tag{A2}$$

Any linear combination of these interpolants ensures second-order spatial accuracy in smooth regions of numerical solution. Falle (1991) used a TVD slope limiter which is equivalent[2] using following linear combination of the polynomials $P_\pm$

$$P(x) = w_- P_-(x) + w_+ P_+(x)\,, \tag{A3}$$

[2]Falle (1991) also use the polynomial $P_0(x) = u_i$, for the case where $\beta_+\beta_- \leq 0$.

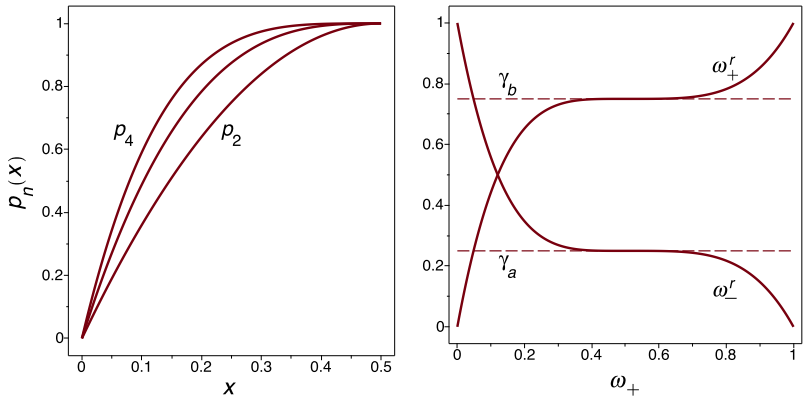

Figure A1. Left panel: mapping polynomials $p_n(x)$. Right panel: non-linear WENO weights for $P^r(x)$ obtained with $\alpha(x) = p_4(x)$.

where

$$w_- = \frac{\beta_+}{\beta_+ + \beta_-}\,, \quad w_+ = \frac{\beta_-}{\beta_+ + \beta_-}\,, \tag{A4}$$

are the weights and

$$\beta_- = (u_i - u_{i-1})^2\,, \quad \beta_+ = (u_{i+1} - u_i)^2 \tag{A5}$$

are the 'roughness' indicators. Incidentally, these indicators are the same as in Jiang & Shu (1996) for a third-oder WENO interpolation. The weights (A4) satisfy the constraint

$$w_- + w_+ = 1\,. \tag{A6}$$

It is clear that not the absolute values of β_+ and β_- but their ratio determines the weights:

(i) $w_-, w_+ \to 1/2$ as $\beta_-/\beta_+ \to 1$;
(ii) $w_- \to 1$ and $w_+ \to 0$ as $\beta_-/\beta_+ \to 0$;
(iii) $w_- \to 0$ and $w_+ \to 1$ as $\beta_+/\beta_- \to 0$.

This combination favours the interpolant with smaller gradient, thus reducing oscillations at regions with rapid variation of the numerical solution, such as shock waves. For example, suppose that $u_{i+1} = u_i$, like in the upstream state of a shock, whereas $u_{i-1} \neq u_i$ is a point of numerical shock structure. Then, $\beta_+ = w_- = 0$ and $P(x_i) = P_+(x) = u_i$.

Interestingly, these weights treat critical points of smooth solutions almost on the same footing as shocks. To illustrate this, suppose that a local maxima is located exactly between x_i and x_{i+1}, so that $u_{i+1} = u_i$. Then, like in the shock example, $\beta_+ = w_- = 0$ and $P(x) = P_+(x) = u_i$. Generalizing, any weights based on the ratios of the roughness indicators do not differentiate between shocks and critical points. This applies to the WENO weights proposed by Jiang & Shu (1996), which results in a loss of accuracy in the vicinity of critical points.

To remove this confusion, we propose the modified smoothness indicators

$$\beta_\pm = (u_i - u_{i\pm1})^2 + U^2\left(\frac{\Delta x}{L}\right)^2 + \epsilon\,, \tag{A7}$$

where

$$U = \max(|u_{i+1}|, |u_i|, |u_{i-1}|)\,, \tag{A8}$$

is the maximal magnitude of u on the stencil, $L \gg \Delta x$ is the minimal characteristic length-scale of what can be considered as a computationally smooth solution, and ϵ is a small number, introduced to avoid division by zero when $u_i = u_{i-1} = u_{i+1} = 0$. Hence,

(i) in smooth regions away from local extrema,

$$(u_{i\pm1} - u_i)^2 \approx \left(\frac{\partial u}{\partial x}\right)_i^2 \Delta x^2 \le U^2\left(\frac{\Delta x}{L}\right)^2\,.$$

Hence, $\beta_-/\beta_+ \approx 1$ and $w_\pm \approx 1/2$, like in the original TVD scheme.

(ii) At strong shocks, either

$$(u_{i+1} - u_i)^2 \approx U^2 \gg \frac{U^2}{L^2}\Delta x^2\,,$$

or

$$(u_{i-1} - u_i)^2 \approx U^2 \gg \frac{U^2}{L^2}\Delta x^2\,,$$

or the both of them. In any of the cases, the new terms introduced in equation (A7) have a little impact on $w_\pm$.

(iii) Near the critical of points of smooth solutions,

$$(u_{i\pm1} - u_i)^2 \approx \left(\frac{\partial^2 u}{\partial x^2}\right)_i^2 \Delta x^4 \approx U^2\left(\frac{\Delta x}{L}\right)^4 \ll U^2\left(\frac{\Delta x}{L}\right)^2\,.$$

Hence, $\beta_-/\beta_+ \approx 1$ and $w_\pm \approx 1/2$, like at any other point of smooth solutions.

As to the value of L, it is reasonable to use $L = n_{sm}\Delta x$, with $5 \lesssim n_{sm} \lesssim 10$, leading to the final expression for the modified weights

$$\beta_- = (u_i - u_{i-1})^2 + \frac{U^2}{n_{sm}^2} + \epsilon\,, \tag{A9}$$

$$\beta_+ = (u_{i+1} - u_i)^2 + \frac{U^2}{n_{sm}^2} + \epsilon\,. \tag{A10}$$

For the test simulations described in this paper, we set $n_s = 10$ and $\epsilon = 10^{-25}$.

A2 Third-order WENO weights

Third-order WENO interpolation utilizes the fact that the linear interpolation (A3) yields the same value at $x = x_{i+1/2}$ as the quadratic interpolation based on the all three points of the stencil S if $w_- = 1/4$ and $w_+ = 3/4$, and the same value at $x = x_{i-1/2}$ if $w_- = 3/4$ and $w_+ = 1/4$. Thus, two linear interpolants of the form (A3), one per each interface of the cell, can be used to achieve third-order accurate interpolation to the both interfaces. $\gamma_a = 1/4$ and $\gamma_b = 3/4$ are known as the ideal or linear weights. We denote the interpolant used for the interpolation to the $x_{i-1/2}$ interface of ith cell as

$$P^l(x) = w_-^l P_-(x) + w_+^l P_+(x)\,, \tag{A11}$$

and the interpolant used for the interpolation to the $x_{i+1/2}$ as

$$P^r(x) = w^r_- P_-(x) + w^r_+ P_+(x)\,. \tag{A12}$$

Their weights satisfy exactly the same constraint as before

$$w^l_- + w^l_+ = 1\,, \quad w^r_- + w^r_+ = 1\,. \tag{A13}$$

One may put $w^r_+ = w^l_- = \gamma_{\rm b}$ and $w^l_+ = w^r_- = \gamma_{\rm a}$, but this will lead to violent oscillations at shocks. Instead, WENO weights are non-linear, reducing to the ideal weights only on very smooth solutions. At shocks, the linear interpolant with lower gradient should dominate. Since the second-order TVD interpolation, described earlier, is also based on the three-point stencil S, has exactly the same form as the third-order WENO interpolants, and already has the required behaviour at shocks, a mapping of the TVD weights, which is closed to the identity mapping at shocks but yields ideal weights on smooth solutions, suggests itself.

So, we look for the mapping $w_+ \to \{w^l_+, w^r_+\}$ such that

$$w^l_+ \to \gamma_{\rm a}, \quad w^r_+ \to \gamma_{\rm b} \quad \text{as} \quad w_+ \to 0.5\,, \tag{A14}$$

$$w^r_+, w^l_+ \to w_+ \quad \text{as} \quad w_+ \to 0 \quad \text{or} \quad w_+ \to 1\,. \tag{A15}$$

It also makes sense to require the functions $w^l_+(w_+)$ and $w^r_+(w_+)$ to be monotonic. Hence, if

$$w^r_+ = \gamma_{\rm b}\alpha(w_+)\,, \tag{A16}$$

then $\alpha(x)$, $x \in [0, 1]$, must be a monotonic function of x satisfying the conditions

$$\alpha(0) = 0\,, \quad \alpha(0.5) = 1\,, \quad \alpha(1) = 1/\gamma_{\rm b}\,. \tag{A17}$$

In addition, it is desirable to have a reasonably wide region near $x = 0.5$ where $\alpha(x)$ remains close to 1. Hence, one may also require a number of its low-order derivatives to vanish at $x = 0.5$. For $x \in [0, 0.5]$, these conditions are satisfied by the polynomials

$$p_n(x) = 1 - (1 - 2x)^n\,, \tag{A18}$$

where $n \geq 2$. The first three examples of such polynomials are shown in the left panel of Fig. A1.

To determine $\alpha(x)$ for $x \in [0.5, 1]$, we require the function $w^r_-(w_-)$ to be the same as $w^r_+(w_+)$, apart from $\gamma_{\rm b}$ replaced by $\gamma_{\rm a}$, and write

$$w^r_- = \gamma_{\rm a}\alpha(w_-)\,. \tag{A19}$$

Given the constraints (A6) and (A13), one can write this equation as

$$w^r_+ = 1 - \gamma_{\rm a}\alpha(1 - w_+)\,.$$

This allows us to fully specify $w^r_+(w_+)$ and $w^r_-(w_+)$,

$$w^r_+(w_+) = \begin{cases} \gamma_{\rm b} p_n(w_+), & 0 \leq w_+ \leq 0.5\,, \\ 1 - \gamma_{\rm a} p_n(1 - w_+), & 0.5 < w_+ \leq 1\,, \end{cases} \tag{A20}$$

$$w^r_-(w_+) = 1 - w^r_+(w_+)\,. \tag{A21}$$

Similarly, one finds

$$w^l_+(w_+) = \begin{cases} \gamma_{\rm a} p_n(w_+), & 0 \leq w_+ \leq 0.5\,, \\ 1 - \gamma_{\rm b} p_n(1 - w_+), & 0.5 < w_+ \leq 1\,, \end{cases} \tag{A22}$$

$$w^l_-(w_+) = 1 - w^l_+(w_+)\,. \tag{A23}$$

Fig. A1 shows the non-linear weights based on $p_4(x)$.

A3 Downgrading to second-order TVD interpolation at strong shocks

Strong shocks in high-σ regime may still exhibit residual numerical oscillations of the flow parameters. To remove them completely, one can switch to the second-order TVD interpolation in the safety zone around such shocks (see Section 3.5).

APPENDIX B: VARIABLES CONVERSION

The conserved variables of the perturbation system are mass density

$$D = \rho\gamma\,, \tag{B1}$$

energy density

$$\mathcal{E}_{(1)} = \mathcal{E} - \mathcal{E}_{(0)} = \boldsymbol{E}_{(0)} \cdot \boldsymbol{E}_{(1)} + \boldsymbol{B}_{(0)} \cdot \boldsymbol{B}_{(1)} + \frac{E^2_{(1)} + B^2_{(1)}}{2} + w\gamma^2 - p\,, \tag{B2}$$

where

$$\mathcal{E} = \frac{E^2 + B^2}{2} + w\gamma^2 - p\,, \tag{B3}$$

$$\mathcal{E}_{(0)} = \frac{E^2_{(0)} + B^2_{(0)}}{2}\,, \tag{B4}$$

momentum density

$$\boldsymbol{S}_{(1)} = \boldsymbol{S} - \boldsymbol{S}_{(0)} = \boldsymbol{E}_{(0)} \times \boldsymbol{B}_{(1)} + \boldsymbol{E}_{(1)} \times \boldsymbol{B}_{(0)} + \boldsymbol{E}_{(1)} \times \boldsymbol{B}_{(1)} + w\gamma^2 \boldsymbol{v}\,, \tag{B5}$$

where

$$\boldsymbol{S} = \boldsymbol{E} \times \boldsymbol{B} + w\gamma^2 \boldsymbol{v}\,, \tag{B6}$$

$$\boldsymbol{S}_{(0)} = \boldsymbol{E}_{(0)} \times \boldsymbol{B}_{(0)}\,. \tag{B7}$$

In addition, we have the perfect conductivity condition is

$$\boldsymbol{E} = -\boldsymbol{v} \times \boldsymbol{B}\,, \tag{B8}$$

which can also be written as

$$\boldsymbol{E}_{(1)} = -\boldsymbol{E}_{(0)} - \boldsymbol{v} \times \boldsymbol{B}\,. \tag{B9}$$

and the polytropic equation of state

$$w = (\rho + \kappa p)\,, \tag{B10}$$

where $\kappa = \Gamma/(\Gamma - 1)$.

Equation (B8) leads to

$$\boldsymbol{E} \times \boldsymbol{B} = \boldsymbol{B} \times (\boldsymbol{v} \times \boldsymbol{B}) = B^2 \boldsymbol{v} - (\boldsymbol{v} \cdot \boldsymbol{B})\boldsymbol{B}$$

and hence

$$\boldsymbol{S} = (B^2 + W)\boldsymbol{v} - (\boldsymbol{B} \cdot \boldsymbol{v})\boldsymbol{B}\,, \tag{B11}$$

where $W = w\gamma^2$. From the last equation, it follows that

$$(\boldsymbol{B} \cdot \boldsymbol{v}) = \frac{(\boldsymbol{S} \cdot \boldsymbol{B})}{W}\,. \tag{B12}$$

Substituting this back in equation (B11), we obtain

$$\boldsymbol{v} = \frac{\boldsymbol{S} + ((\boldsymbol{S} \cdot \boldsymbol{B})/W)\boldsymbol{B}}{B^2 + W}\,. \tag{B13}$$

This equation shows that $\boldsymbol{v}$ depends solely on the unknown W. From this result, it follows that

$$S^2 = (B^2 + W)^2 v^2 - (2W + B^2)\frac{(\boldsymbol{S} \cdot \boldsymbol{B})^2}{W^2}\,. \tag{B14}$$

Thus, we have an equation for only two unknowns, W and v^2. However, this equation is not immediately suitable for the high magnetization case as it involves terms of the order B^4, that results in large computational errors for the hydrodynamic variables. As we show later, these terms cancel out.

Next, we use the perfect conductivity condition (B9) to eliminate $\boldsymbol{E}_{(1)}$ from the expression (B2) for $\mathcal{E}_{(1)}$. To this end, we first find that

$$\boldsymbol{E}_{(0)}\cdot\boldsymbol{E}_{(1)} = -E^2_{(0)} - \boldsymbol{E}_{(0)}\cdot(\boldsymbol{v}\times\boldsymbol{B})\,,$$

and

$$E^2_{(1)} = E^2_{(0)} + 2\boldsymbol{E}_{(0)}\cdot(\boldsymbol{v}\times\boldsymbol{B}) + ||\boldsymbol{v}\times\boldsymbol{B}||^2\,,$$

and hence

$$\boldsymbol{E}_{(0)}\cdot\boldsymbol{E}_{(1)} + \frac{E^2_{(1)}}{2} = -\frac{E^2_{(0)}}{2} + ||\boldsymbol{v}\times\boldsymbol{B}||^2\,.$$

This can be reduced further using

$$\begin{aligned}||\boldsymbol{v}\times\boldsymbol{B}||^2 &= (\boldsymbol{v}\times\boldsymbol{B})\cdot(\boldsymbol{v}\times\boldsymbol{B})\\ &= \boldsymbol{v}\cdot(\boldsymbol{B}\times(\boldsymbol{v}\times\boldsymbol{B}))\\ &= \boldsymbol{v}\cdot(\boldsymbol{v}B^2 - \boldsymbol{B}(\boldsymbol{v}\cdot\boldsymbol{B}))\\ &= v^2B^2 - (\boldsymbol{v}\cdot\boldsymbol{B})^2\,.\end{aligned}$$

Substituting the last two results into equation (B2), we obtain

$$\mathcal{E}_{(1)} = \frac{1}{2}(B^2v^2 - (\boldsymbol{v}\cdot\boldsymbol{B})^2) + W - p - \frac{E^2_{(0)}}{2} + \frac{B^2_{(1)}}{2} + \boldsymbol{B}_{(0)}\cdot\boldsymbol{B}_{(1)}\,. \tag{B15}$$

The last three terms of the right-hand side are already known. To reflect this, we introduce

$$\bar{\mathcal{E}}_1 = \mathcal{E}_{(1)} + \frac{E^2_{(0)}}{2} - \frac{B^2_{(1)}}{2} - \boldsymbol{B}_{(0)}\cdot\boldsymbol{B}_{(1)}\,, \tag{B16}$$

and write equation (B15) as

$$\bar{\mathcal{E}}_1 = \frac{1}{2}B^2v^2 + W - p - \frac{1}{2}\frac{(\boldsymbol{S}\cdot\boldsymbol{B})^2}{W^2}\,, \tag{B17}$$

where we have also applied equation (B12). This equation contains the unknowns v^2, W, and p. Using EOS (B10) and equation (B1), we find that

$$p = \frac{1}{\kappa}(W(1-v^2) - D(1-v^2)^{1/2})\,, \tag{B18}$$

which allows to eliminate p from equation (B17) and obtain the cubic equation

$$a_3(v^2)W^3 + a_2(v^2)W^2 + a_0 = 0\,, \tag{B19}$$

where

$$a_3 = 1 - \frac{1-v^2}{\kappa}\,, \tag{B20}$$

$$a_2 = \frac{1}{2}B^2v^2 - \bar{\mathcal{E}}_1 + D\frac{(1-v^2)^{1/2}}{\kappa}\,, \tag{B21}$$

$$a_0 = -\frac{1}{2}(\boldsymbol{S}\cdot\boldsymbol{B})^2\,. \tag{B22}$$

Thus, we have obtained two equations (B14) and (B19), for the unknowns W and v^2. This system is to be solved numerically.

Obviously, one can further reduce the system to just one equation, either for v^2 or W. Following the reasonable argument of Del Zanna et al. (2007), it is preferable to eliminate W by solving the cubic equation (12) analytically. This allows us to control the condition $0 \le v^2 < 1$ during the numerical iterations of the Newton method (or its secant version) for the resultant equation.

The fully expanded expression for the coefficient a_2 is

$$a_2 = \frac{1}{2}(B^2v^2 - E^2_{(0)}) - \mathcal{E}_{(1)} + \frac{B^2_{(1)}}{2} + \boldsymbol{B}_{(0)}\cdot\boldsymbol{B}_{(1)} + D\frac{(1-v^2)^{1/2}}{\kappa}\,.$$

The first two terms of this expression constitute the difference between $B^2v^2/2$ and $E^2_{(0)}$. These non-negative terms can be very large and their difference can be a source of large error in computations of a_2 in the case of high magnetization.

Introducing the drift velocity of force-free approximation

$$\boldsymbol{v}_{(0)} = \frac{\boldsymbol{E}_{(0)}\times\boldsymbol{B}_{(0)}}{B^2_{(0)}}\,.$$

One can write

$$B^2v^2 - E^2_{(0)} = B^2v^2 - B^2_{(0)}v^2_{(0)} = B^2_{(0)}(v^2 - v^2_{(0)}) + (B^2_{(1)} + \boldsymbol{B}_{(0)}\cdot\boldsymbol{B}_{(1)})v^2\,,$$

and hence

$$\begin{aligned}a_2 = {}& \tfrac{1}{2}(B^2_{(0)}(v^2 - v^2_{(0)}) + (B^2_{(1)} + \boldsymbol{B}_{(0)}\cdot\boldsymbol{B}_{(1)})v^2) -\\ & -\mathcal{E}_{(1)} + \tfrac{B^2_{(1)}}{2} + \boldsymbol{B}_{(0)}\cdot\boldsymbol{B}_{(1)} + D\tfrac{(1-v^2)^{1/2}}{\kappa}\,.\end{aligned}$$

Computations of the term $\boldsymbol{S}\cdot\boldsymbol{B}$ may also involve subtraction of large numbers and hence results in large errors. This can be avoided if we note that $\boldsymbol{S}_{(0)}\cdot\boldsymbol{B}_{(0)} = 0$ and write

$$\boldsymbol{S}\cdot\boldsymbol{B} = \boldsymbol{S}_{(0)}\cdot\boldsymbol{B}_{(1)} + \boldsymbol{S}_{(1)}\cdot\boldsymbol{B}\,.$$

Substituting $(\boldsymbol{S}\cdot\boldsymbol{B})^2/W^2$ from equation (B17) into equation (B14) and cancelling out terms of the order B^4 results in

$$\begin{aligned}W^2v^2 + 4\bar{\mathcal{E}}_1W + 4(p-W)\left(W + \tfrac{B^2}{2}\right) = {}& S^2_{(1)} + 2\boldsymbol{S}_{(1)}\cdot\boldsymbol{S}_{(0)} -\\ & -2\bar{\mathcal{E}}_1B^2 - B^2_{(0)}v^2_{(0)}(B^2_{(1)} + 2\boldsymbol{B}_{(0)}\cdot\boldsymbol{B}_{(1)})\,,\end{aligned} \tag{B23}$$

where

$$\bar{\mathcal{E}}_1 = \mathcal{E}_{(1)} - \frac{B^2_{(1)}}{2} - \boldsymbol{B}_{(0)}\cdot\boldsymbol{B}_{(1)}\,.$$

This paper has been typeset from a TEX/LATEX file prepared by the author.